Karlsruhe Institute of Technology

Determination of SKS/ SKKS-splitting parameters in the lowermost mantle beneath Siberia

Master's thesis of

Fiona Dorn

at the Geophysical Institute (GPI)
KIT-Department of Physics
Karlsruhe Institute of Technology (KIT)

Date of submission:
21.03.2025

Supervisor:	Prof. Dr. Joachim Ritter
Co-supervisor:	Prof. Dr. Thomas Bohlen
Advisor:	Yvonne Fröhlich

Erklärung / Statutory declaration

Ich versichere wahrheitsgemäß, die Arbeit selbstständig verfasst, alle benutzten Hilfsmittel vollständig und genau angegeben und alles kenntlich gemacht zu haben, was aus Arbeiten anderer unverändert oder mit Abänderungen entnommen wurde sowie die Satzung des KIT zur Sicherung guter wissenschaftlicher Praxis in der momentan gültigen Fassung beachtet zu haben.

I declare truthfully that I have written this thesis all by myself, that I have fully and accurately specified all auxiliary means used, that I have correctly cited (marked) everything that was taken, either unchanged or with modification, from the work of others, and that I have complied with the current version of the KIT statutes for safeguarding good scientific practice.

Karlsruhe, 21.03.2025

Signature: Fiona Dorn

Acknowledgments

I would like to thank all those who have contributed to the success of this thesis in various ways, but also those who have supported me during the course of my studies, even if I do not mention them by name.

First and foremost, I would like to thank Professor Dr. Joachim Ritter for his comprehensive supervision of my master's thesis and the opportunity to work on this interesting topic. I was able to learn a lot from you and I am very grateful for your mentorship!

A special thanks goes to Yvonne Fröhlich, who advised me during my master's thesis and was able to answer my numerous scientific and programming-related questions. Many thanks for passing on the scripts and for the many discussions we had over the entire duration of my master's thesis! I would also like to thank Muhammad Dillah for the exchange of ideas while working on the same topic. Dr. Sarah Mader, I am very grateful for the many valuable, not only scientific, conversations we have had in the office. Many thanks also to everybody in the seismology working group, who provided lots of useful input in the seminars and shared helpful tips.

I would like to thank Professor Dr. Thomas Bohlen for taking on the role of co-supervisor. My thanks also go to Dr. Thomas Hertweck for providing me with the LaTeX template of this work.

I appreciate the provision of the data by the GFZ Potsdam and IRIS Data Management Center.

I also wish to express my thanks to all those who contributed to proofreading this work, especially to Jakob Linder, Runa Ostermeier and Alexander Kreusel.

A special thanks goes to my parents Eva Dresler and Martin Dorn, as well as my boyfriend Jakob Linder for their loving support, encouragement and patience throughout my studies. Last but not least, I would like to thank my friends from EWB and from my shared flat for showing me time and time again that there also exists a Karlsruhe outside Campus West.

Abstract

The observation of shear wave splitting (SWS) is an unambiguous indication of seismic anisotropy in the Earth's interior and, thus, of deep geodynamic deformation processes. The latter is based on the premise that crystals exhibiting anisotropic elastic properties can be aligned or deformed by deformation processes or flows. This results in a directional dependency of seismic velocities and therefore SWS.

In the Earth's lowermost mantle (LMM), specifically in the D″ layer, there exist large-scale structures that drive global processes (mantle plumes) or result from them (remnants of subducted slabs). These structures potentially influence the heat flow from the core and the magnetic field lines through the mantle. In order to investigate the latter in particular, the SWS of SKS, SKKS, and PKS (jointly referred to as *X*KS) phases propagating through a high latitude flux lobe (HLFL), a region of higher magnetic flux, below Siberia is measured.

The splitting parameters, the fast polarisation direction ϕ and the delay time δt, are determined using both the energy-minimisation and the rotation-correlation method in the *MATLAB* program *SplitLab*. A special focus lies on phase pair SWS discrepancies, i.e., between SKS and SKKS phases, as they are a clear indication for a LMM contribution to the splitting signal.

Our study of the target region of Siberia has revealed anisotropy in this region and a comprehensive image of this anisotropy has been obtained by studying the region along different orientations of raypaths. A total of 49 pairs of core refracted phases have been measured. Out of these, 19 pairs are discrepant. For these pairs, the phases with piercing points in the region of the highest magnetic flux predominately show splitting, while we observe mostly no splitting for phases piercing through the D″ layer at larger offsets from the HLFL.

List of Figures

List of Tables

List of Abbreviations

2D	two-dimensional
3C	three-component
3D	three-dimensional
BAZ	backazimuth
CMB	core-mantle boundary
CMT	Centroid Moment Tensor
CPO	crystal preferred orientation
EQ	earthquake
FD	Fiona Dorn
FDSN	International Federation of Digital Seismograph Networks
HLFL	high latitude flux lobe
LLSVP	large low shear wave velocity province
LMM	lowermost mantle
LPO	lattice preferred orientation
MD	Muhammad Dillah
MG	Michael Grund
nCCC	normalised cross-correlation coefficient
pp	piercing point
qP	quasi P
qS	quasi S
RC	rotation-correlation
SC	Silver and Chan
S-N	south-north
SNR	signal-to-noise ratio
SPO	shape preferred orientation
SWS	shear wave splitting
SWSM	shear wave splitting measurement
ULVZ	ultra low velocity zone
W-E	west-east

Contents

Chapter 1

Introduction

This thesis is preceded by the motivation (Section 1.1) and the outline (Section 1.2).

1.1 Motivation

The main field of the Earth's magnetic field is generated by a geodynamo in the outer core, controlled by convection of a liquid, iron-rich, electrically conductive fluid in the outer core (Clauser, 2014). It varies over many different timescales, with short-term variations but also regions of stable magnetic flux over long periods. Regions with long-term, intense magnetic flux at stable geographic positions are called high latitude flux lobes (HLFLs) due to their occurrence at latitudes between 60° to 70° in the Northern Hemisphere and the corresponding reverse flux patches at similar latitudes in the Southern Hemisphere (Amit et al., 2011; Gubbins et al., 2007; Olson and Amit, 2006).

Within the Priority Program 2404 "Reconstructing the Deep Dynamics of Planet Earth over Geologic Time" (DeepDyn), we investigate possible seismic signatures at geomagnetic HLFLs. The focus is on four target regions in the Northern Hemisphere: Siberia, Canada, the North Atlantic and Indonesia. While Siberia and Canada show the HLFLs, the North Atlantic region should be the location of a third postulated HLFL, but this area does not show an intense magnetic flux signal in models of the magnetic field (Jackson et al., 2000). The region beneath Indonesia is characterised by an area of intense magnetic flux moving westwards over time. We aim to understand whether mineralogy or seismic structures (i.e., thermal constraints) could contribute to these different magnetic signatures at the core-mantle boundary (CMB). The aim of the project is to understand and study in detail the possible seismic signatures of regions with an increased magnetic flux in the lowermost mantle (LMM). In doing so, a combination of two approaches is used: seismic reflections (University of Münster) and seismic anisotropy (Karlsruhe Institute of Technology).

The target region of the work in this thesis is the HLFL beneath Siberia which is studied using seismic anisotropy investigations. We measure the shear wave splitting (SWS) of core refracted phases (SKS, SKKS and PKS, jointly referred to as XKS phases) at seven different seismic stations. SWS is generally a clear indicator of anisotropy. Accordingly, the SWS of linearly polarised shear waves is used in seismology to study elastic anisotropy in the Earth, particularly in the mantle. SWS can be seen as an elastic analogue to birefringence in optics. The fast polarisation direction ϕ and the accumulated delay time δt between the two quasi S (qS) waves serve to describe the SWS. These splitting parameters are determined in a *MATLAB* program using the *SplitLab* package (Wüstefeld et al., 2008) applying both the energy-minimisation and the rotation-correlation method. The usage of

*X*KS phases gives us the advantage of being able to constrain the origin of the anisotropy. In particular, we search for phase pair SWS discrepancies, i.e., between SKS and SKKS phases, as they are a clear indication for a LMM contribution to the splitting signal (Deng et al., 2017; Nowacki et al., 2011; Wookey and Kendall, 2007; Maupin and Park, 2007; Savage, 1999).

The selection of the seismic recording stations includes stations in Northern Scandinavia (KEF, HSPB, SA01, SA02 and SA05) and Central Asia (ULN, WMQ). This gives us the possibility to study the potential anisotropy in the LMM beneath Siberia in much more detail by using different orientations of the raypaths through the LMM.

The splitting observations in the proximity of the HLFL beneath Siberia are compared with models of the Earth's magnetic field at the CMB and previous studies of anisotropy in the region. Measurements at the KEF station are additionally compared between different analysts to ensure reproducibility and reliability of the results and define criteria to measure reliable shear wave splitting measurements (SWSMs).

1.2 Outline

In the following Chapter 2, the theoretical background of the work in this thesis is presented. This includes a section about the Earth's interior (Section 2.1) as well as a section about the fundamentals of elastic anisotropy (Section 2.2). Chapter 3 focuses on the methods used to measure SWS (Section 3.1) and the software, that is used to determine the splitting parameters (Section 3.2). Additionally, it presents an exemplary SWSM (Section 3.3). The SWSMs, that are performed at the KEF station, are discussed in Chapter 4 regarding the measurement procedure (Section 4.1), the results (Section 4.2) and a comparison between different analysts (Section 4.3). Chapter 5 presents the SWSMs at the HLFL beneath Siberia. Firstly, suitable earthquakes and stations are selected (Section 5.1) and then the updated measurement procedure is introduced (Section 5.2). The results are presented and discussed in Chapter 6. In Section 6.1, this is done for all stations individually and then combined for all stations (Section 6.2). In addition, the results are compared to other studies previously performed in the region (Section 6.3). An evaluation and a discussion on the method of SWS is shown in Section 6.4. Chapter 7 summarises the main results of this work and an outlook for future work is given.

Chapter 2

Theory

2.1 The Earth's interior

The Earth's structure is radially stratified in three concentric shells: the core, mantle and crust. A schematic cross-section of this stratification can be seen in Fig. 2.1. The core, composed of dense, iron-nickel-rich material, is further separated into the solid inner core and the liquid outer core, where the bulk of the geomagnetic field is generated. The outer core is limited by the CMB at a depth of 2891 km, which separates the liquid core from the significantly less dense mantle, primarily composed of magnesium-iron silicates. The mantle can be divided into upper and lower mantle. On top of the upper mantle lays the crust, a thin layer with low-density minerals (Moores and Twiss, 2014; Clauser, 2014).

The boundaries between these shells are given by seismic discontinuities, measurable as abrupt changes of the seismic velocity (Nowacki et al., 2011). These discontinuities result from variations in both the chemical and physical properties of the present materials, including density, elasticity constants and phase transitions of the dominant minerals (Clauser, 2014; Garnero et al., 2005). Despite the presence of these discontinuities, the shells are dynamically interconnected through complex mechanisms, including convection of material in the liquid core and the solid mantle. Large-scale convective motions driven by heat flux are depicted in Fig. 2.1, with arrows indicating the flow of material. Cold lithospheric material, shown in dark grey, subducts as slabs in subduction zones. On the contrary, in regions with an increase in temperature and a reduction in seismic velocity, labelled as large low shear wave velocity provinces (LLSVPs), mantle plumes might arise, going along with an upwelling of warmer mantle material (Moores and Twiss, 2014; Heron, 2019).

The convection within the outer core (see Fig. 2.1) is depicted by spiral arrows. Temperature differences within the iron-rich liquid fluid lead to the formation of convection cells. Due to the Earth's rotation and thus the resulting Coriolis force, spiral movements in Taylor columns are produced. This generates a stable magnetic field, referred to as the main field (Clauser, 2014).

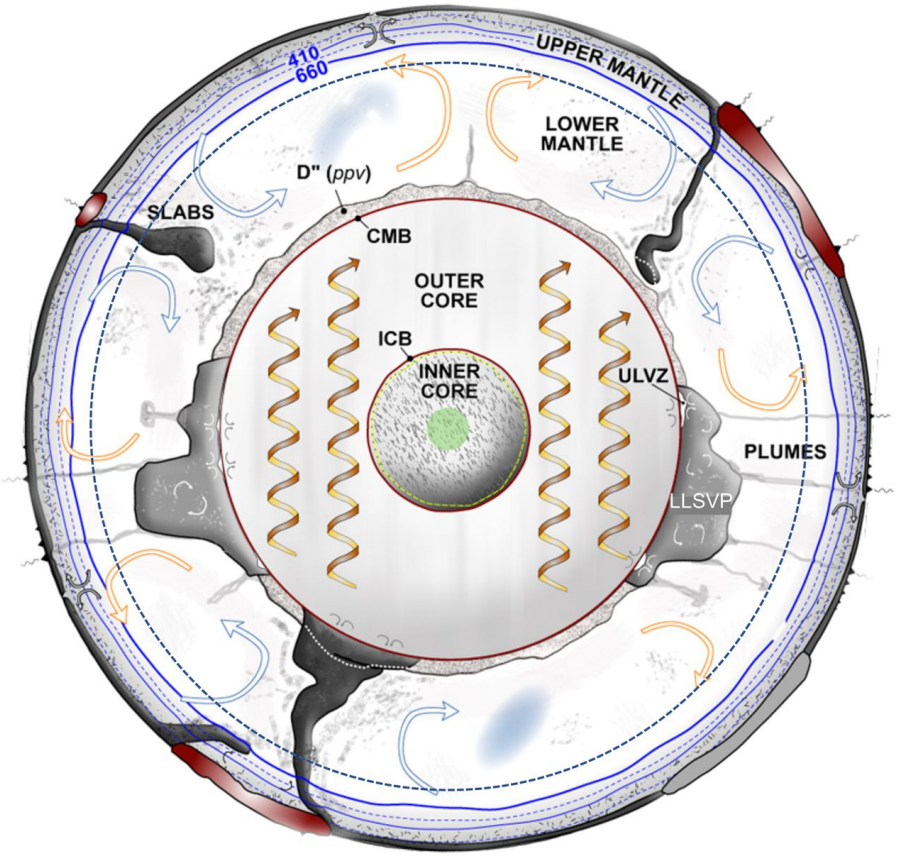

Figure 2.1: *A schematic cross-section of the Earth's interior, displaying its radial stratification, consisting of inner and outer core, lower and upper mantle and crust, with discontinuities between these layers. Dynamic processes such as large-scale convection in both the lower mantle, driven by subduction of cold lithospheric slabs, and outer core, sustaining the geodynamo, are displayed. Figure is taken from Heron (2019).*

2.1.1 The Earth's geomagnetic field

The Earth's magnetic field consists of three components: the main field, generated by the geodynamo in the outer core, the crustal field, mainly controlled by the magnetisation of the rocks in the crust, and the extraterrestrial field caused by current systems of the ionosphere and interplanetary magnetic fields. 94 % of the magnetic field measured at the Earth's surface can be explained by the resulting dipole of the geodynamo, residual non-dipole contributions to the magnetic field and regional crustal anomalies (Clauser, 2014). The main field is generated by a geodynamo in the outer core, controlled by convection of an iron-rich, electrically conducting fluid (Nowacki et al., 2011; Amit et al., 2011; Olson and Amit, 2006). The state of convective overturn of the outer core, including heat loss to the solid mantle in combination with crystallisation and chemical differentiation at the boundary with the solid inner core, drives the geodynamo. As a result, it continuously converts the kinetic energy of the moving fluid into electromagnetic energy resulting in a magnetic dipole field at the Earth's surface with a dipole axis slightly inclined relative to the Earth's rotation axis (Olson and Amit, 2006; Busse, 2000).

At the CMB, the process of the geodynamo generates a more complex magnetic field, varying both in time and space and being largely controlled by Earth's rotation (Finlay and Jackson, 2003; Gubbins et al., 2007).

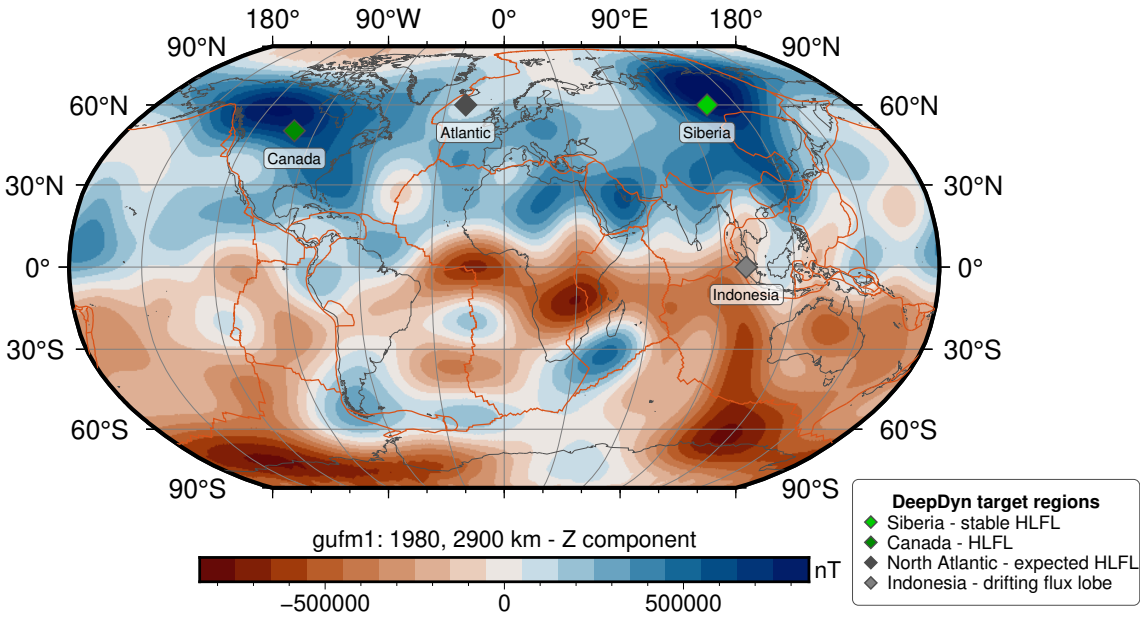

Figure 2.2: *Model of the radial component of the Earth's magnetic field (gufm1 1980) at* 2900 km *depth according to Jackson et al. (2000). The regions labelled with diamonds mark regions of (expected) intense magnetic flux. Data of the figure is taken from Jackson et al. (2000) and Amit et al. (2011).*

Figure 2.2 shows the *gufm1* model of Jackson et al. (2000). This model represents the radial component of the Earth's magnetic field at the CMB at a depth of 2900 km for the years between 1590 to 1990 (Jackson et al., 2000). The model of the Earth's magnetic field at the CMB deviates significantly from a simple axial dipole. It is characterised by a complex pattern with regions of high magnetic flux at latitudes between 60° and 70° in the Northern Hemisphere and regions with intense reverse magnetic flux at similar latitudes in the Southern Hemisphere and near the equator (Olson and Amit, 2006). The geodynamo exhibits a complex pattern of the magnetic field due to its three-dimensional (3D) processes involving the whole core and a potential strong influence by the heterogeneous LMM (Amit et al., 2010). According to Bloxham and Gubbins (1987), the lowermost 200 km to 300 km of the mantle (D″ layer) form a boundary layer for the generation of the Earth's magnetic field, as the highly electrically conductive core is electromagnetically coupled to the less conductive lower mantle. The fluid motion within the core induces an electromotive force in the lower mantle, causing the magnetic field lines in the mantle to move due to advection (Bloxham and Gubbins, 1987). The morphology of the geomagnetic field is thus influenced by the boundary conditions of both the geometry of the inner core but also the structure of the LMM (Gubbins et al., 2007).

Although the geodynamo generates a temporary changing field, some regions have experienced only slight changes over the past 400 years, consistent with paleomagnetic data from the last few million years (Jackson et al., 2000; Gubbins et al., 2007). Lower mantle thermal heterogeneity, along with thermal coupling between the core and mantle, lead to lateral variations in the heat flux at the CMB. This induces thermal winds at the CMB, concentrating the magnetic field at preferred locations and producing non-axisymmetric geomagnetic features, which can only exist due to lateral heat flux variations (Gubbins et al., 2007; Amit et al., 2010).

High latitude flux lobes

In the model of the Earth's magnetic field at the CMB (Fig. 2.2), four regions with high magnetic flux can be identified at latitudes between 60° and 70°, both on the Northern and Southern Hemispheres. These regions, referred to as HLFL, exhibit a distinct long-term temporal behaviour compared to the general characteristics of the Earth's magnetic field. Predominantly, these lobes show quasi-stationary periods with small oscillations around preferred longitudes. The statistical preference for high magnetic flux at high latitudes could be associated with the core-mantle thermal coupling (Amit et al., 2011, 2010). The heterogenous mantle might influence the preferred longitudes in the steady core field. Models of a numerical dynamo support this thesis by demonstrating that a heterogenous heat flux outer boundary condition affects the location of the intense magnetic flux patches (Amit et al., 2011). Between these quasi-stationary periods, varying degrees of drifts in the regions of high magnetic flux can be observed. Amit et al. (2010) associated the episodical drift events with an azimuthal motion of fluid downwelling structures, which concentrate a higher magnetic flux. These non-axisymmetric features arise due to flow convergence at these latitudes (Amit et al., 2010). In the Southern Hemisphere, drifts are more prominent due to higher north-south shear in the mantle driven zonal thermal wind. The predominant westward drifts indicate a time-averaged zonal core flow driven by thermal coupling between the core and mantle (Amit et al., 2011).

One of the regions with high magnetic flux is located beneath Siberia, marked with a bright green diamond in Fig. 2.2. The corresponding region of high reverse flux is situated in the southern Indian Ocean (Jackson et al., 2000). This HLFL pair, and particularly the HLFL beneath Siberia, is remarkably stable over long times. This is potentially associated with a seismic anomaly in the mantle in this region (Gubbins et al., 2007). The flux concentration in the region might be related to the downwelling fluid, which indicates a cold mantle (Bloxham and Gubbins, 1987).

A second HLFL pair is located beneath Canada, with its reverse counterpart situated southwest of South America in the Pacific Ocean. The HLFL beneath Canada exhibits greater mobility compared to the Siberian pair (Jackson et al., 2000; Gubbins et al., 2007). Gubbins et al. (2007) suggest that this increased mobility might be driven by thermal variations exerting a stronger influence on the magnetic field than compositional variations.

As the thermal conductivities of minerals at the CMB form a critical boundary condition for core dynamics, a deeper understanding of these properties is essential to be able to constrain the processes at the CMB. The observed differences in thermal variations, which are more pronounced beneath Siberia than Canada, may influence why the HLFL beneath Siberia is less mobile (Gubbins et al., 2007).

The possible position of an assumed third HLFL beneath the North Atlantic, expected due to symmetry reasons, is marked in dark grey in Fig. 2.2. However, no intense magnetic flux is observed at this location.

Additionally, Fig. 2.2 indicates in light grey the origin of an intense magnetic flux region beneath Indonesia. Unlike the other intense flux regions, this patch migrates westwards at a relatively rapid rate (Jackson et al., 2000). Consequently, this region is classified as a drifting flux lobe. Intense magnetic flux patches in the equatorial region remain less well understood, since numerical dynamo models frequently exhibit zonal equatorial upwelling, leading to a dispersion of the field at low latitudes (Aubert, 2005; Olson and Amit, 2006). However, if the toroidal field is sufficiently strong, these regions of upwelling material might concentrate intense magnetic fields beneath the CMB (Bloxham and Gubbins, 1987).

The LMM does not only play an important role in the control of the geodynamo and, thus, the Earth's magnetic field. It also features distinct seismic characteristics. The lowermost 200 km to 300 km of the mantle, referred to as D″ layer, represent a thermal boundary layer between the hot, vigorously convecting core and the colder and slower convecting mantle. It plays a fundamental role in both the dynamics of the mantle and the core. This layer is involved in the processes of mantle convection, as it presents the presumable origin of upwelling plumes and the terminus of downwelling mantle material, including subducted slabs (Nowacki et al., 2011; Peltier, 2007).

The D″ layer is bounded by a sharp, horizontal seismic discontinuity lying between 200 km to 300 km above the CMB, which could result from a phase transformation from bridgmanite to a post-perovskite polymorph of $MgSiO_3$. The large seismic variability of the D″ layer results from chemical heterogeneity of minerals, heterogeneity of the lateral seismic velocity, fine-scale structures and seismic anisotropy (Deng et al., 2017; Murakami et al., 2004; Nowacki et al., 2011).

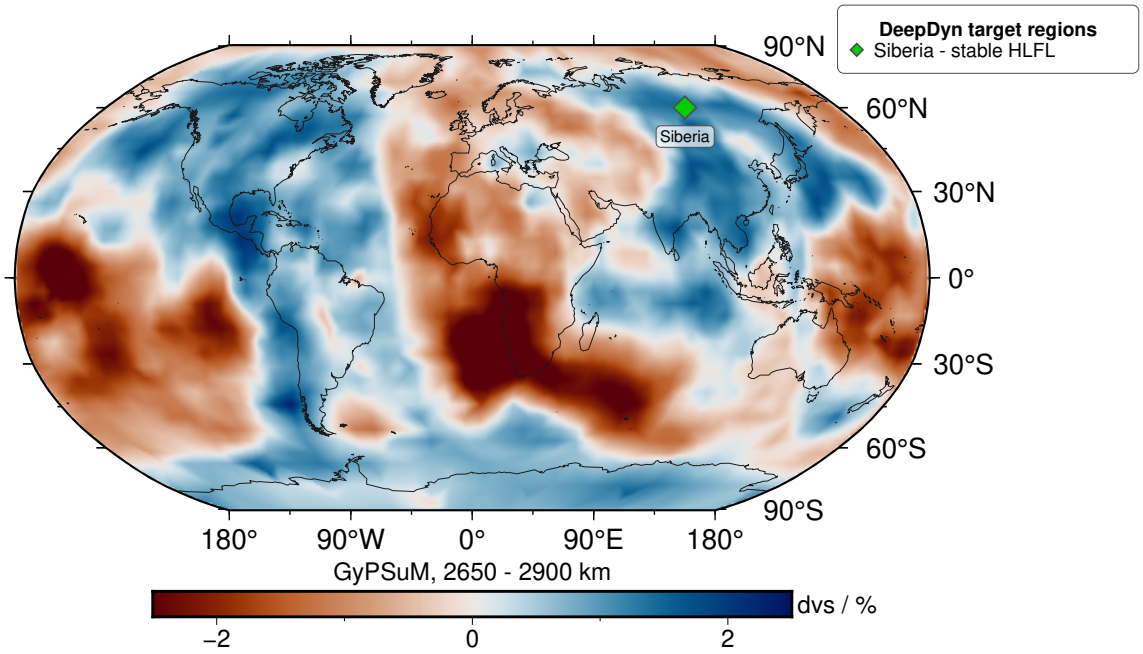

Figure 2.3: *Model of the lateral variations in shear wave velocity in* 2650 km *to* 2900 km *depth according to the GyPSuM model of Simmons et al. (2010). The colours show percental deviations from the global mean velocity in this depth range with higher velocities in blue and lower velocities in red. The center of the HLFL beneath Siberia is marked with a green diamond.*

Figure 2.3 displays a model of the shear wave velocity at depths ranging from 2650 km to 2900 km. The *GyPSuM* model of Simmons et al. (2010) is derived by combining information from geodynamics and mineral physics using both compressional and shear waves. The colours represent the percental deviations in shear wave velocity from the global mean velocity in this depth range, with red indicating lower shear wave velocities and blue denoting above-average shear wave velocities. These differences in seismic shear wave velocities are associated with temperature variations in the D″ layer. Regions with increased shear wave velocity go along with colder material, while a reduction in shear wave velocity is associated with a hotter material (Deng et al., 2017; Nowacki et al., 2011). Strong lateral variation can be seen worldwide, with two principal regions of lower shear wave velocity located beneath southern Africa and the South Atlantic, as well as the Pacific. These

regions are known as LLSVPs (McNamara, 2019). Shear wave velocity is reduced up to 30% near the edges and within these LLSVPs in so-called ultra low velocity zones (ULVZs) (cf. Fig. 2.1) (Deng et al., 2017; Nowacki et al., 2011). Another region of interest is the Perm anomaly beneath Eurasia, which shows reduced shear wave velocity as well and might feature similar thermochemical properties as the LLSVPs. Studies at the edges of the Perm anomaly and LLVSPs beneath the Pacific and Africa show particularly strong LMM anisotropy along the edges of regions with reduced shear wave velocity due to deformation along the margins. The concentration of deformation, and thus anisotropy, at the borders of the LLSVPs provides insights into the interaction between LLSVPs and ambient mantle flow. It may reflect processes such as focused upwelling flow at the bases of mantle plumes near the edges or flow of material deflected by the LLSVP itself (Deng et al., 2017; Long and Lynner, 2015).

In contrast to the LLSVPs beneath the Pacific and Africa, Fig. 2.3 indicates an increase in shear wave velocity at the target region of this thesis, Siberia. The colder material, associated with this velocity increase, is assumed to be a pile-up of remnant slab material from past subductions (Wookey and Kendall, 2008). The material may be associated with the remnant material of the Mongol-Kazakh slab which subducted around 240 Ma ago (van der Meer et al., 2018).

Variations in the temperature above the CMB go along with lateral differences in heat flux through the D″ layer since it serves as a thermal boundary layer above the isothermal CMB (Gubbins et al., 2007). Using the shear wave velocity at the CMB, obtained from tomographic studies, as a proxy for heat flux in simulations of the geodynamo, results in a first combination of geomagnetic and seismological studies (Gubbins et al., 2007). This combination of approaches from geomagnetic and seismological methods is further continued in this thesis by using anisotropy measurements with the aim to better constrain the seismic signatures at the HLFL beneath Siberia.

2.2 Anisotropy

In an anisotropic medium, physical properties depend on the direction. In general, these properties can include elastic, thermal or electromagnetic properties (Greulich et al., 1998). Seismic anisotropy refers to the seismic velocities of the elastic waves depending on the direction of wave propagation and polarisation. The mechanisms that lead to directional variations in seismic velocities can be classified into intrinsic mechanisms, independent of wavelength, and extrinsic mechanisms, which depend on the wavelength. An example is a periodic thin layering of material with contrasting elastic properties, which might appear anisotropic if studied with waves with larger wavelength (Maupin and Park, 2007; Wookey and Kendall, 2007). Anisotropy must be distinguished from heterogeneity, which describes the spatial dependency of a property. Despite their different physical meaning, for both anisotropy and heterogeneity it is a matter of the scale whether a medium appears anisotropic or heterogenous. Therefore, an at small scales heterogenous layered material can appear both homogenous or anisotropic if it is studied with waves with larger wavelength (Maupin and Park, 2007).

In the following sections, wave propagation in anisotropic media (2.2.1), its resulting observation of SWS (2.2.2) and causes of anisotropy in the Earth (2.2.3) are discussed. Additionally, *X*KS pairs and their advantages, including the constrain of the depth of the anisotropy, are presented in Section 2.2.3.

2.2.1 Wave propagation in anisotropic media

In case of a linear elastic medium, the stress σ_{ij} is linearly related to the resulting strain ϵ_{kl} by the elasticity tensor c_{ijkl} as given in Hooke's law (Nowacki et al., 2011),

$$\sigma_{ij} = c_{ijkl}\epsilon_{kl}, \tag{2.1}$$

with the infinitesimal strain given by

$$\epsilon_{kl} = \frac{1}{2}\left(\frac{\partial u_k}{\partial x_l} + \frac{\partial u_l}{\partial x_k}\right). \tag{2.2}$$

Here, u_n represents the displacement and x_n the Cartesian spatial coordinate. Using the symmetry of the stress and strain tensors, as well as the intrinsic symmetry of c_{ijkl}, the 81 components of the elasticity tensor can be reduced to 21 independent parameters for a general anisotropic medium (Wookey and Kendall, 2007). Introducing constraints on the anisotropy of the medium further reduces the number of independent parameters of the elastic tensor. In the isotropic case, the elastic tensor consists of only two independent elastic parameters, the Lamé parameters, λ and μ (Wookey and Kendall, 2007).

For a plane wave of the form $\boldsymbol{u}(\boldsymbol{x}, t) = \boldsymbol{a}\, f(\boldsymbol{n}\cdot\boldsymbol{x} - ct)$ propagating in the direction $\boldsymbol{n}$ with a phase velocity c in a homogeneous medium with density ρ, the equation of motion is given by

$$\frac{c_{ijkl}}{\rho} n_j n_k a_l = c^2 a_i\,. \tag{2.3}$$

The term $\frac{c_{ijkl}}{\rho} n_j n_k$ is known as the Christoffel matrix. To solve the equation of motion, the eigenvalues and eigenvectors of the Christoffel matrix need to be found. In general, this leads to three distinct eigenvalues, corresponding to three waves propagating in the direction $\boldsymbol{n}$ with different phase velocities. Their polarisation direction is given by the eigenvectors, which can be chosen perpendicular to each other. Unlike in isotropic media, where the wave polarisation is parallel or perpendicular to the propagation direction, in anisotropic media, the polarisation deviates from these orientations (Maupin and Park, 2007; Nowacki et al., 2011). In the upper part of Fig. 2.4, the orientation of the polarisation and propagation direction of both the P and the S wave can be seen for an isotropic medium. In the lower part of the figure, the situation for a weak anisotropy is depicted. For a weak anisotropy, the three waves separate into a quasi P (qP) wave, with the highest velocity and a polarisation nearly aligned with the propagation direction, and two qS waves with different velocities and a polarisation in the plane nearly perpendicular to the propagation direction (Maupin and Park, 2007; Savage, 1999; Wookey and Kendall, 2007).

2.2.2 Shear wave splitting

If a shear wave enters an anisotropic medium, its particle motion is projected onto the polarisation direction of the two qS waves. This can be seen in Fig. 2.5. The initial linearly polarised S wave enters an anisotropic region and "splits" into two perpendicularly polarised qS waves with different velocities. This effect is known as birefringence (analogue to the optical birefringence for light) or SWS. The fast qS wave propagates with the fastest seismic velocity and with a polarisation in the plane of the fastest seismic velocity, while the slow qS wave moves with the slowest seismic velocity with a polarisation in the plane of the slowest seismic velocity, which is perpendicular to the fastest one. After leaving the anisotropic region, the splitting effect is preserved, which allows to describe the anisotropy by two splitting parameters: β, the angle between the fast polarisation direction and initial polarisation of S wave in the isotropic medium, and δt, the delay time between the arrivals of the fast and the slow qS wave. Figure 2.5 shows the angle ϕ which is the azimuth between

north and the orientation of the fast polarisation axis. It can be calculated from β using the initial polarisation direction of the S wave in the isotropic medium and the inclination i (measured from the Z axis oriented downward in the vertical plane) (cf. Section 3.1.2). Since splitting delay times are typically between 0.5 s to 2.0 s, they are shorter than the dominant periods T of teleseismic shear waves (T$\in [5, 10]$ s). Therefore, it is not possible to visually observe two independent peaks. Instead, the qS waves display an elliptical particle motion (Vecsey et al., 2008; Wookey and Kendall, 2007; Maupin and Park, 2007).

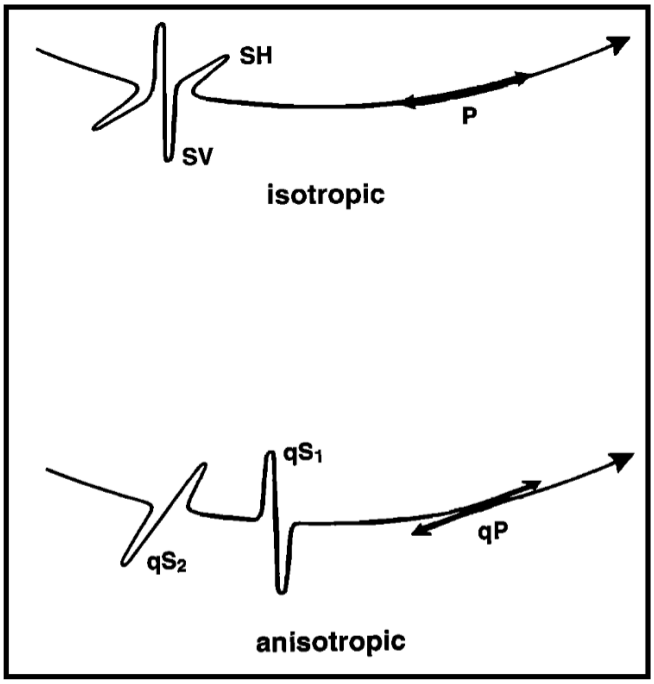

Figure 2.4: *Direction of the polarisation and propagation of SV, SH and P wave in the isotropic case (top) and qS_1, qS_2 and qP wave in the presence of a weak anisotropic medium (bottom). Figure is taken from Savage (1999).*

Split measurement and null measurement

When measuring SWS, two observational types are possible. One needs to differentiate between the possibility to perform SWSMs and get a useable result or not. The presence of an (apparent) null measurement when performing SWSMs needs to be classified as a result of a successful measurement. Therefore, SWS in general can lead to two observational types: an (apparent) null measurement and a split measurement. For isotropic media, only null measurements for SWS can be observed. In the case of an anisotropic medium, we can observe both a split measurement and an (apparent) null measurement, depending on the orientation of the ray passing through the medium and the type of anisotropy (Creasy et al., 2021). As an example, for simple anisotropy four backazimuth (BAZ) directions do not show SWS since the initial polarisation in the isotropic medium is parallel or orthogonal to the fast (or slow) polarisation direction of the anisotropic medium. Thus, no oscillation occurs perpendicular to the fast (or slow) polarisation direction in the anisotropic medium (Fröhlich, 2020; Creasy et al., 2021).

A combination of the different anisotropies results in the linear (but not commutative) combination of splitting since the observation of SWS is a path integrated property. Thus, depending on the type of anisotropy and the orientation of the fast polarisation axis, the delay time is the sum or difference between the different layers. Therefore, certain configurations of anisotropy cannot be resolved (Silver and Long, 2011; Fröhlich, 2020).

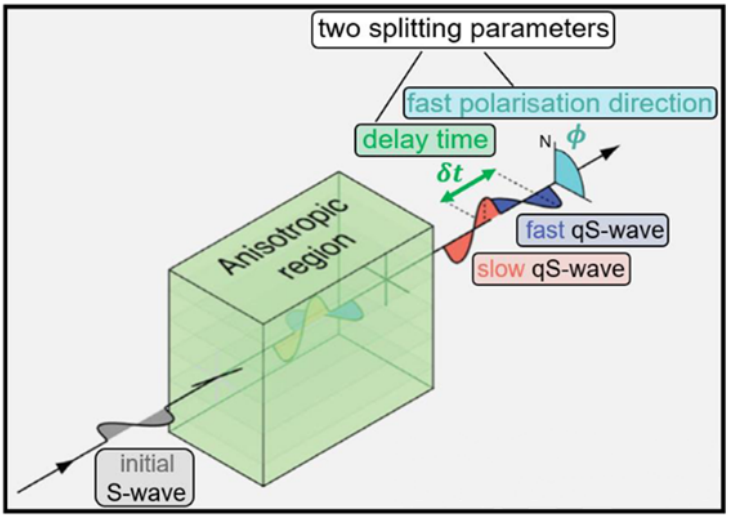

Figure 2.5: *Principle of SWS when a linearly polarised S wave enters an anisotropic region (green) and gets split up into two waves. The two perpendicular polarised qS waves propagate at different velocities. The two splitting parameters describing the anisotropy are the fast polarisation direction ϕ measured as the angle from north and the accumulated delay time δt between both waves. Figure is taken from Nowacki et al. (2011), modified by Fröhlich et al. (2021).*

2.2.3 Anisotropy studies in the Earth

Seismic anisotropy occurs on different scales and depths within the Earth. In addition to the crust and the upper mantle, which are widely anisotropic, the D″ layer and the inner core show anisotropy as well (Long and Becker, 2010; Nowacki et al., 2011; Creasy et al., 2021). Depending on the region of interest, the epicentral distance to the recording station and the distribution of suitable earthquakes, different phases are favourable to study anisotropy in the Earth. In this thesis, core refracted phases are used, since they, in comparison to S and ScS waves, offer a variety of advantages to study anisotropy particularly in the LMM.

*X*KS pairs

The splitting parameters ϕ and δt, measured at seismometers, are path-integrated parameters. Thus, they do not contain information about the position of the anisotropy along the raypath. Core refracted phases, referred to as *X*KS phases, allow to limit the possible source region of the anisotropy. As it can be seen in Fig. 2.6 for the SKS and SKKS phases, the S wave that emitted from the earthquake is converted to a P wave upon entering the liquid outer core. SKS and SKKS phases both travel through the outer core with SKKS being reflected once at the inside of the CMB. Leaving the outer core, both phases are converted back into S waves when a smooth CMB and laterally homogenous Earth is assumed (Nowacki et al., 2011). This conversion constrains the S wave to a purely SV polarised wave with a known initial polarisation equivalent to the BAZ in the isotropic case. Due to the propagation as a P wave inside the outer core, all the anisotropy information that is measured at the receiving station can only result from the station-side (upcoming) raypath between the CMB and the station. As previously discussed, the upper-mantle and crust are highly anisotropic. Therefore, the measured anisotropy at the station may be composed to a certain degree of an upper-mantle/crustal effect. Combining pairs of *X*KS phases, especially SKS and SKKS phases, from the same event uses the advantage of the waves to have nearly identical raypaths in the upper mantle and crust. Yet, the phases have a different raypath in the LMM. Therefore, if we observe a so-called discrepant pair,

where one of the two phases shows anisotropy and the other one does not show it, we can assume that a contribution to the measured SWS results from an anisotropy located in the region where the two *X*KS phases have different raypaths (Deng et al., 2017; Creasy et al., 2021). Since there is no evidence of a widespread significant anisotropy in the lower mantle, this most likely comes from the D″ layer (Meade et al., 1995; Deng et al., 2017; Nowacki et al., 2011).

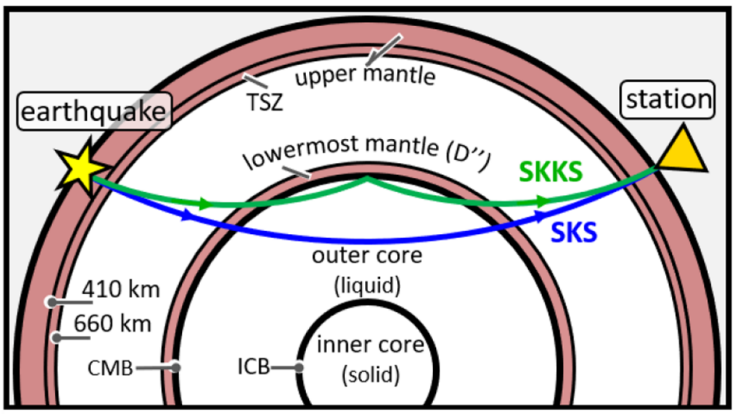

Figure 2.6: *Schematic drawing of the raypaths of the SKS (blue) and the SKKS phases (green) through the Earth's interior. The layers (inner core, outer core, LMM, lower and upper mantle and crust) as well as the discontinuities (TSZ = transition zone, CMB, and ICB = inner core boundary) are displayed. The waves propagate from the earthquake (yellow star) to the station (triangle). They are converted to a compressional wave upon entering the liquid outer core and converted back to a shear wave when leaving the outer core. The different raypaths for SKS and SKKS phases in the lower mantle and the different piercing points at the CMB are striking. Figure is taken from Fröhlich et al. (2021).*

Additionally, PKS phases, which propagate as P waves until leaving the outer core at the station side of the CMB at a piercing point close to the one of the SKS phase and being converted to a SV polarised wave, can be used to study anisotropy in the LMM (Kaviris et al., 2018). They are limited in their usage due to the limited epicentral range, $[130, 148]^\circ$, where they can be observed (Kennett, 2005; Maupin and Park, 2007).

Occurrence and causes of anisotropy in the Earth

Most of the minerals in the Earth are seismically anisotropic. Without external influences, these minerals are randomly orientated, resulting in an isotropic appearance of the material. However, external forces can lead to a preferred alignment of minerals, causing directional variations in seismic velocity. Such an anisotropy is classified as bulk-anisotropy, meaning that the wavelength of the seismic waves is much larger than the characteristic length of the structure. Causes for the anisotropy include lattice preferred orientation (LPO) of intrinsic anisotropic minerals or shape preferred orientation (SPO) of isotropic materials with contrasting elastic properties (Wookey and Kendall, 2007; Long and Becker, 2010; Nowacki et al., 2011).

LPO occurs when an external stress field leads to strain in an intrinsic anisotropic crystal. An increase in strain rate results in dislocations within the crystal lattice. Therefore, the term crystal preferred orientation (CPO) describes the same cause of anisotropy. Depending on the relative strengths of the active slip systems in the crystal, these dislocation migrate (e.g. a slip on a crystallographic plane) (Nowacki et al., 2011). The large-scale alignment of crystals leads to LPO. The degree of observed anisotropy depends on both the elastic

anisotropy of the individual crystals and the degree of alignment (Wookey and Kendall, 2007).

Another cause of macroscopic anisotropy arises from the SPO of minerals. This involves the alignments of features on length-scales that are larger than individual crystals, including sub-wavelength layering, preferred alignment of intrusions or (periodic) ordering of material with contrasting elastic properties (Nowacki et al., 2011; Wookey and Kendall, 2007).

The differentiation between LPO and SPO as the dominant effect in the LMM remains challenging with the currently available data. The observations are compatible with a complementary presence of both SPO and LPO (Nowacki et al., 2011). The measurement of anisotropy in the LMM can be due to the alignment of melt pockets, stratification of layers with different seismic velocities or the alignment of minerals through deformation. By observing SWS as an unambiguous indication of seismic anisotropy, we are able to investigate deep geodynamic deformation processes which control the alignment of minerals or structures (Kendall and Silver, 1998; Lay et al., 1998).

Simple and complex anisotropy

In this thesis, an anisotropic structure without lateral and vertical variation of the anisotropy, with a transversal isotropy and a horizontal axis of symmetry is referred to as simple anisotropy. Any anisotropy that deviates from this description is described as complex anisotropy, including layering of anisotropic layers or lateral varying anisotropy (Long and Silver, 2009; Plomerová et al., 1996). The general methods to measure SWS, including the methods used in this thesis and described in Chapter 3, generally assume a simple anisotropy. Only then the splitting parameters measured at the surface directly relate to the anisotropic properties present in depth. Otherwise, apparent splitting parameters are determined, which represent significant results only in the presence of a simple constellation of complex anisotropy. Systematic variations in (apparent) splitting parameters with the BAZ or differences in the resulting splitting parameters obtained using different analysis methods can indicate the presence of complex anisotropic structures (Long and Silver, 2009).

Chapter 3

Methods

3.1 Methods to determine the splitting parameters

In this thesis, SWSMs are performed by determining the splitting parameters for individual seismic events (single-event analysis) in the *MATLAB* program *SplitLab* from Wüstefeld et al. (2008). *X*KS phases of different permanent and temporary broadband seismometers are analysed. As discussed in Section 2.2.2, the expected delay time of the qS waves is shorter than the dominant period of the *X*KS phases. Therefore, no complete separation of the signal in the time domain is obtained. To address this, the methods of Bowman and Ando (1987) and Silver and Chan (1991) are implemented in *SplitLab*, allowing the determination of SWS by performing a grid-search to determine the optimal splitting parameters which best correct for the observed splitting and, thus, linearise the horizontal particle motion.

3.1.1 Bowman and Ando method

The method after Bowman and Ando (1987), also referred to as rotation-correlation (RC) method, relies on maximising the normalised cross-correlation coefficient (nCCC). The horizontal seismograms are rotated relative to each other in 5° steps between 0° to 90°. In doing so, the nCCC is calculated between the seismograms of the fast and the slow qS waves with a time shift of ±2 s. The orientation of the fast polarisation axis ϕ is determined by the rotation angle corresponding to the maximal nCCC. The delay time δt is given by the time shift between the minimum and maximum nCCC. The seismogram of the slower qS wave is shifted relative to the fast qS wave by the determined delay time. Finally, the seismograms are rotated back and the corrected particle motion can be seen in the south-north (S-N) vs. west-east (W-E) hodogram (Bowman and Ando, 1987; Long and van der Hilst, 2005).

3.1.2 Silver and Chan method

Silver and Chan (1991) introduced an eigenvalue (EV) method to determine the splitting parameters. A specialised case of this method, named Silver and Chan (SC) method, can be applied if the initial polarisation direction is known. Both methods (EV and SC) are implemented in *SplitLab* and therefore briefly outlined in this section.

Eigenvalue method (EV)

In a homogeneous isotropic medium, a shear wave $\boldsymbol{u}(\omega)$ with an amplitude $w(\omega)$, angular frequency ω and a polarisation direction given by the unit vector $\hat{\boldsymbol{p}}$ can be described with

$$\boldsymbol{u}(\omega) = w(\omega) \exp\left(-\mathrm{i}\omega T_0\right) \hat{\boldsymbol{p}}. \tag{3.1}$$

The wavelet-function $w(\omega)$ is the product of the Fourier-transformed source time function, the damping operator, the instrument response and the complex vector amplitude. If the wave enters an anisotropic medium, birefringence occurs, which is described by the splitting operator

$$\boldsymbol{\Gamma} = \exp(\mathrm{i}\omega\delta t/2)\hat{\boldsymbol{f}}\hat{\boldsymbol{f}} + \exp(-\mathrm{i}\omega\delta t/2)\hat{\boldsymbol{s}}\hat{\boldsymbol{s}}. \tag{3.2}$$

The splitting operator $\boldsymbol{\Gamma}$ consists of the two splitting parameters β and δt. Here, the angle β is given by the angle between the fast polarisation axis $\hat{\boldsymbol{f}}$ and the initial polarisation $\hat{\boldsymbol{p}}$. The slow direction $\hat{\boldsymbol{s}}$ is perpendicular to the fast one, as discussed in Section 2.2. The two waves experience a time shift of $\delta t/2$ and $-\delta t/2$, respectively. The dyadic products of the slow, $\hat{\boldsymbol{s}}\hat{\boldsymbol{s}}$, and fast, $\hat{\boldsymbol{f}}\hat{\boldsymbol{f}}$, polarisation directions with themselves present the projection operators. Consequently, a shear wave in an anisotropic medium $\boldsymbol{u}_\mathrm{s}(\omega)$ is expressed as

$$\boldsymbol{u}_\mathrm{s}(\omega) = \boldsymbol{\Gamma}\boldsymbol{u}(\omega) = w(\omega) \exp\left(-\mathrm{i}\omega T_0\right) \boldsymbol{\Gamma} \cdot \hat{\boldsymbol{p}}. \tag{3.3}$$

To obtain the splitting parameters, the parameters that best undo the splitting are to be determined. Therefore, the optimal transformation from Eq. 3.3 to Eq. 3.1 needs to be found:

$$\tilde{\boldsymbol{u}}_\mathrm{s}(\omega) = \boldsymbol{\Gamma}^{-1}\boldsymbol{u}_\mathrm{s}(\omega) = \boldsymbol{\Gamma}^{-1}\boldsymbol{\Gamma}\boldsymbol{u}(\omega) = \boldsymbol{u}(\omega). \tag{3.4}$$

This requires computing the inverse operator $\boldsymbol{\Gamma^{-1}}$, which is achieved by calculating the two-dimensional covariance matrix of the particle motion and determining the eigenvalues λ_1 and λ_2. For the isotropic case, the covariance matrix has only one eigenvalue differing from zero. Therefore, the optimal splitting parameters are those that minimise λ_2 and maximise the singularity of the covariance matrix. The quality of the outcome of this method depends strongly on the data quality. In data with lower noise level, more accurate splitting parameters can be determined in the grid search. These values then bring the covariance matrix closer to a singular matrix (Fröhlich, 2020; Silver and Chan, 1991; Sanz Alonso, 2017).

Energy minimisation method (SC)

If the initial isotropic polarisation vector $\hat{\boldsymbol{p}}$ is known, a special case of the EV method, the energy minimisation method, can be applied. Assuming a smooth CMB and a laterally homogeneous Earth, the initial polarisation of the XKS phases is constrained by the P-SV conversion at the CMB (cf. Section 2.2.3). Under these conditions, the energy on the corrected transverse component,

$$E_{\tilde{\mathrm{u}}_{\mathrm{s,T}}} = \int_{-\infty}^{+\infty} \tilde{u}^2_{\mathrm{s,\ T}}(t)\mathrm{d}t, \tag{3.5}$$

can be minimised. The signal on the transverse component $u_{\mathrm{s,T}}(t)$ (cf. Fig. 3.1) in the time-domain is given by

$$u_{\mathrm{s,T}}(t) = -\frac{1}{2}(w(t+\delta t/2) - w(t-\delta t/2))\sin(2\beta). \tag{3.6}$$

Similarly, the signal on the radial component in the time domain, $u_{\mathrm{s,R}}(t)$ (cf. Fig. 3.1), is given by

$$u_{\mathrm{s,R}}(t) = w(t+\delta t/2)(\cos(\beta))^2 - w(t-\delta t/2)(\sin(\beta))^2\,. \tag{3.7}$$

Comparing Eqs. 3.6 and 3.7, it follows that the signal on the transverse component becomes zero in the isotropic case, as expected (Fröhlich, 2020; Silver and Chan, 1991; Sanz Alonso, 2017).

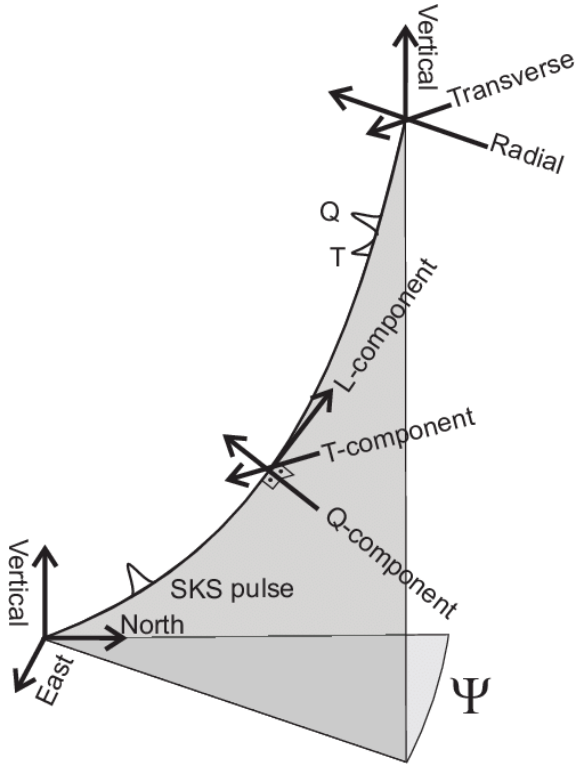

Figure 3.1: *Relation between the ZNE coordinate system and the LQT coordinate system. The measured signal in the ZNE coordinate system is transferred to the ray coordinate system (right-handed LQT system). The ray plane, coloured in grey, is given by the L-component, pointing along the ray from the earthquake to the station, and the Q-component, pointing towards the earthquake. The T-component is perpendicular to the ray plane.* Ψ *denotes the BAZ. Figure taken from Wüstefeld et al. (2008).*

3.1.3 Comparison of the methods

The two methods that are used in this thesis are the SC and RC method. They are influenced by a different amount by the presence of a complex anisotropy, the proximity to apparent null-measurements and noise. In *SplitLab* both methods are implemented and the reliability of the SWSMs is assessed by comparing the results of both methods. If the derived (apparent) splitting parameters are consistent across methods, then the results are considered fairly robust. In general, the SC method is considered to be more robust because it is less affected by noise. In contrast, the RC method is less influenced by complex anisotropy (Long and van der Hilst, 2005; Long and Becker, 2010). Both methods yield distinctly different results when apparent null measurements are observed. The fast polarisation direction ϕ shows a discrepancy of $|\Delta\phi| = |\phi_{SC} - \phi_{RC}| = 45°$ due to $\phi_{SC} = \phi \pm n \cdot 90°$ with $n = 0, 1$ and $\phi_{RC} = \phi \pm 45°$. For δt the SC method obtains large values up to the maximum of the grid search ($4\,s$), while the RC method strives towards very small values for the delay time (Wüstefeld and Bokelmann, 2007).

3.2 Software used for the measurements

To study the anisotropy of the LMM, SWSMs are performed in *MATLAB* R2024a using the *SplitLab* program developed by Wüstefeld et al. (2008). The version 1.2.1, maintained by Rob Porritt, is used for the measurements of SWS in this thesis. The process of requesting seismic traces, as well as further processing of the results obtained in *SplitLab*, including the visualisation of these results, is conducted in *Python* 3.12 using various libraries, including *Matplotlib, ObsPy* and *PyGMT* (Hunter, 2007; Beyreuther et al., 2010; Tian et al., 2025).

3.2.1 Configuration of projects in *SplitLab*

To analyse seismic traces in *SplitLab*, a project-file (.pjt) is created for each station individually. After a configuration of the recording station parameters in *SplitLab*, including the latitude, longitude, station and network codes, as well as a possible seismometer misorientation, a desired earthquake catalogue can be loaded into the project. Earthquakes in the Global Harvard Centroid Moment Tensor (CMT) catalogue (Dziewonski et al., 1981; Ekström et al., 2012) that meet specified constraints regarding time span, epicentral distance, hypocentral depth and moment magnitude are linked to the project. The selected limits and ranges for these parameters are described in Section 4.1 and Section 5.2.

The theoretical arrival times for the desired phases are calculated automatically using the *MATLAB* toolbox *tauP* (Crotwell et al., 1999) based on the Earth *iasp91* model (Kennett and Engdahl, 1991). Seismic traces of suitable earthquakes (cf. Section 5.1.1) are requested in *Python* via the International Federation of Digital Seismograph Networks (FDSN) web service and the *obspy.clients.fdsn* package (Beyreuther et al., 2010). The selected client depends on the requested station. Requested are all three components (vertical (Z), North (N), East (E)) of broadband stations with a duration of 3000 s. Additionally, the station metadata is requested using the FDSN web service to download the station XML-files.

The seismic traces are automatically linked to the corresponding earthquakes of the Global Harvard CMT catalogue (Dziewonski et al., 1981; Ekström et al., 2012) in *SplitLab* by comparing the time in the file header of the three-component (3C) seismograms (.sac-files). Once a project is set up, individual traces are analysed and the splitting parameters can be determined.

3.3 Measurement of shear wave splitting

Each earthquake is studied to potentially pick the onset of SKS, SKKS and PKS phases and measure SWS. In the *view seismogram* panel of *SplitLab*, all three components (vertical (Z), North (N), East (E)) of a given earthquake are displayed. A signal is identified as a relevant seismic phase by comparing the onset of the signal with the theoretical arrival time of the corresponding phase. To distinguish between P, SV and SH waves, the traces are rotated around the BAZ and tilted by the inclination angle, which transfers the measured signal from the ZNE coordinate system (measuring coordinates) to the LQT coordinate system (ray coordinates) (cf. Fig. 3.1). In this coordinate system, the L-component aligns with the direction of the ray towards the receiver (P wave), the Q-component (SV wave) is positive towards the source and the T-component is perpendicular to the LQ-plane (Wüstefeld et al., 2008).

To differentiate between the desired seismic signals and noise (every other signal on the seismogram), the data are filtered with a Butterworth bandpass filter of third order. Since *X*KS phases have typical frequencies of [0.03, 0.20] Hz with a dominant range between [0.1, 0.13] Hz the bounds for the frequency are varied between [0.020, 0.066] Hz for the lower

bound and [0.16, 0.20] Hz for the upper bound with a broader frequency range of [0.020, 0.20] Hz being preferred. If no clear signal of the phases is visible with these filter parameters, the bounds are adjusted, using the same frequency bounds for all measured phases of the same earthquake. The selection of the *X*KS phases is done on the Q-component. Due to the dominant frequencies of the *X*KS phases and the frequency bounds of the bandpass filter, a time window of approximately 15 s to 20 s is selected for the SWSMs. To minimise possible interferences with other phases, a time lag of at least 5 s is kept between the selected time window and other arriving phases, including S, Sdiff or depth phases (pSKS, sSKS) for most SWSMs.

The selected time window is expanded by ±20 s at both ends. SWSMs are performed using both the RC and SC methods as described in Section 3.1. The optimal pair of splitting parameters is identified through a grid search between $[-90, 90]^\circ$ in steps of 1° (RC) and 2° (SC) for the orientation of the fast polarisation axis ϕ. For the delay time values between $[0, 4]$ s are tested with steps of half the sampling frequency.

The SWSMs are classified by visual inspection in the *diagnostic* plots of *SplitLab* (cf. Fig. 3.2). The classification depends on the signal of the different components, the S-N vs. W-E hodogram of the particle motion before and after the correction for splitting, the 95 % confidence interval of the determined (apparent) splitting parameters and the extend to which both methods (RC and SC) agree. The results are classified based on their observational type, (apparent) null measurement or split measurement, and assigned to one of the three quality classes (Table 4.6) according to their signal-to-noise ratio (SNR) and the differences between both methods.

To improve the quality and to increase the number of SWSMs, different limiting frequencies and time windows (varying both in length and onset times) are analysed for each earthquake and phase. Verification of picking the arrival of the correct wave is performed by comparing the absolute value between the initial polarisation of the incoming phase and the theoretical azimuth of the corresponding earthquake, which should theoretically be 180°, since the initial S wave is a pure SV wave. Deviations from this might indicate the misidentification of another phase as *X*KS phase or a possible misorientation of the seismometer. Therefore, picks of phases with values outside the interval $[150, 210]^\circ$ are discarded as they do not correspond to the desired phases.

The SNR in *SplitLab* is calculated as the ratio of the R-component $\tilde{u}_{s,R}(t)$ to the 2σ-envelope of the T-component, $2\sigma_{s,T}$, of the corrected S-wave,

$$\mathrm{SNR}_i = \frac{\max(|\tilde{u}_{s,R_i}(t)|}{2\sigma_{s,T_i}} \quad \text{with} \quad i \in \{\mathrm{RC}, \mathrm{SC}\}, \tag{3.8}$$

(Restivo and Helffrich, 1999). A high SNR is essential to obtain stable and reliable results. Thus, Vecsey et al. (2008) suggest a $\mathrm{SNR}_{\mathrm{SC}} \geq 3$ as lower limit. In addition to the analytical value for the SNR, the visual impression is considered as well. A significant signal on the Q-component is crucial to identify the relevant *X*KS phases. Furthermore, due to noise in real data, it is not possible to achieve a zero signal amplitude on the *T*-component, as discussed in Section 3.1.2. An exemplary measurement for an observation of a null and a split measurement is displayed in Fig. 3.2. In both cases, some signal is visible on the T-component, even after correction. For low SNRs, a (small) signal might hide in the noise on the T-component. Extreme values of the delay time, both for short and long times, need to be studied in more detail. Very small delay times $\delta t < 0.3$ s are associated with large uncertainties and a small signal amplitude on the *T*-component, necessitating a high SNR. In contrast, long delay times $\delta t > 2$ s may be a splitting artefact if no strong signal amplitude is observed on the T-component (Vecsey et al., 2008).

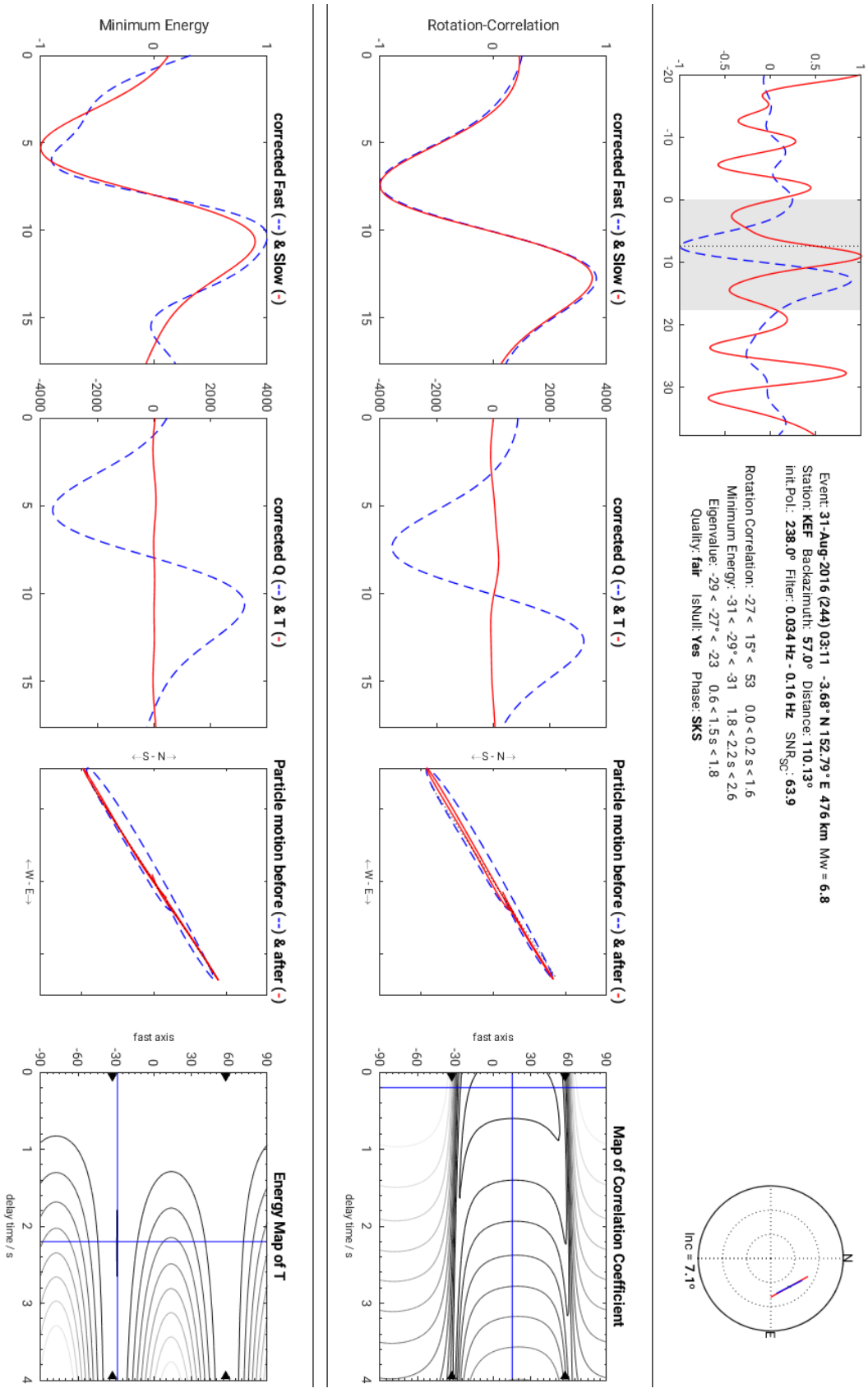

(a) 2016.244 SKS

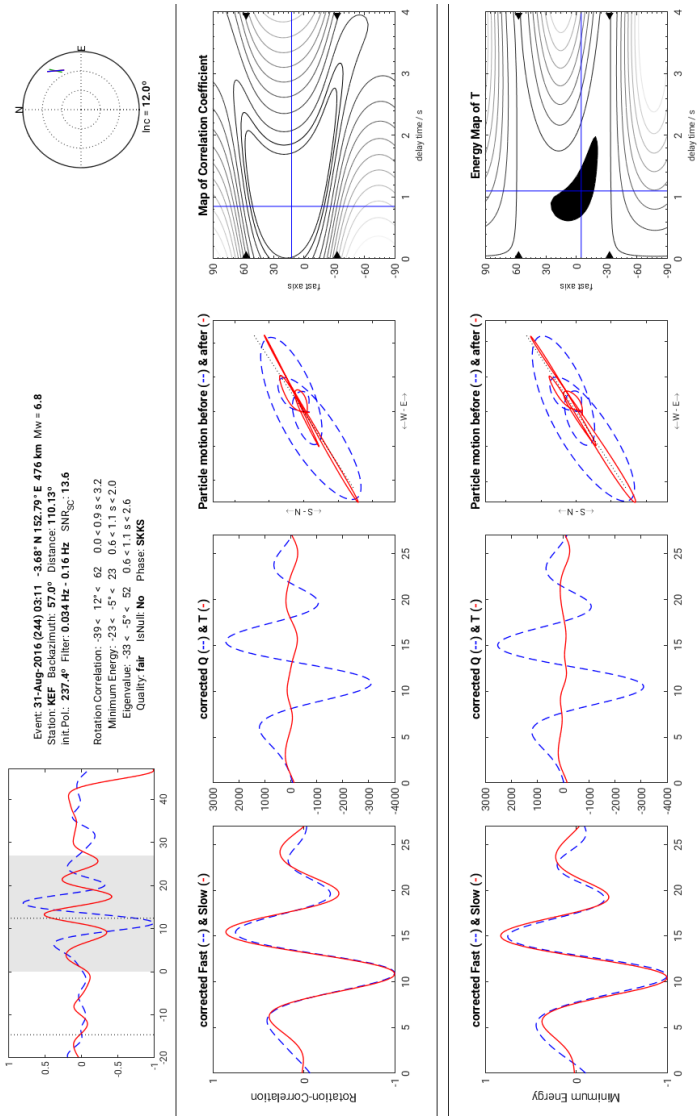

(b) 2016.244 SKKS

Figure 3.2: *Diagnostic plot from SplitLab for an earthquake on 2016/08/31 measured at the KEF station. In the top left of both figures the horizontal seismogram components can be seen, with the grey background marking the selected time window for which splitting is calculated.* ***(a)*** *The figure shows an (apparent) null measurement. The particle motion in the S-N vs. W-E hodogram (third figure from the left for both methods) is already linear before correction for the splitting. In the diagram of the determined splitting parameters a small delay time can be seen for the RC method, while the SC method strives for (in general unlimited) long delay times.* ***(b)*** *The lower figures shows a split measurement. The particle motion in the S-N vs. W-E hodogram (third figure for both methods) is elliptical before the correction for splitting and becomes linear afterwards. Shifting the waveforms by the (apparent) delay time results in the waveforms of the slow and fast polarisation direction to coincide in time (first figure form the left in both lines). After backrotation by the fast polarisation direction most of the signal on the T-component is removed (second figure form the left in both lines).*

Chapter 4

Shear wave splitting measurements at the KEF station (Finland)

4.1 Measurements at KEF station

SWSMs of XKS phases are analysed, which are recorded at the KEF station, network HE in Finland (cf. Table 4.1), and which sample the LMM beneath Siberia and the North Atlantic. The parameters of these earthquakes are listed in Table 4.2. The dataset consists of 903 earthquakes with magnitudes M_W ranging from 5.5 to 8.8, recorded between August 2006 and July 2017 (cf. Table 4.3). To increase the SNRs, only events with hypocentral depth greater than or equal to 20 km are used. The epicentral distances of these earthquakes lie between 80° and 140° as XKS phases occur in this range.

Table 4.1: *Parameters of the recording station KEF.*

station code	**network code**	**longitude ° N**	**latitude ° E**	**operation time**	**sensor type**
KEF	HE	24.8670	62.1667	2006/01/01-	STS-2

The general process of analysing the seismic traces at the KEF station to measure SWS follows the methodology described in Section 3.3. When rotating into the LQT-coordinate system and subsequently measuring SWS, striking deviations are visible for the period between 2012/09/30 and 2017/06/22. These traces show significantly larger amplitudes on the T-component than on the Q-component. An exemplary trace of an earthquake recording, along with the *diagnostic* plot, is provided in Fig. A.1 and Fig. A.2 in the appendix.

Table 4.2: *Parameters of selected earthquakes (EQs) at the station KEF.*

epicentral distance/ °	$80 \leq$ distance ≤ 140
magnitude M_W	≥ 5.5
depth/ km	≥ 20

Revision of the station information confirmed a misorientation of the seismometer by a rotation of 90° during this period. The North-component has been pointing west, while the East-component has been pointing north. To correct for this misorientation, data in

this time interval are rotated back to the correct orientation by swapping the North- and East-component and adjusting the polarity of the new East-component before performing SWSMs.

Table 4.3: *Parameters of the 3C seismograms at the station KEF.*

data-centre	**channel-code**	**sampling rate/ Hz**	**time span**	**total no. of EQ**
GFZ	BH?	20	2006/08/25 - 2017/07/15	903

4.2 Results and discussion

For the 903 earthquakes recorded at the KEF station, I was able to measure SWS in 215 cases for a *X*KS phase. An overview of the number of measurements for each phase and the corresponding splitting observation is presented in Table 4.4. It is noticeable that SKS phases are measured more frequently than SKKS and PKS phases. This discrepancy arises from the challenges associated with observing SKKS and PKS phases and the limited epicentral distance in which PKS phases can be observed.

Table 4.4: *Number of SWSMs for the station KEF. The first column represents the total amount of phases for which I was able to measure SWS, independent of the splitting observation. The individual results for the different phases are listed in the other columns.*

total no. of SWSM	**SKS**		**SKKS**		**PKS**	
	split	null	split	null	split	null
215	74	55	28	22	26	10

For the aim of this thesis, a special focus lies on earthquakes for which at least two *X*KS phases are successfully measured. Table 4.5 provides an overview of the number of such pairs at the KEF station and their respective splitting observations. Particular attention is drawn to discrepant pairs, as they have at least a contribution to the splitting signal from the LMM (Section 2.2.3). A total of 17 of such discrepant pairs have been measured at the KEF station.

Table 4.5: *Number of pairs for which at least two of the analysed XKS phases were observed for an earthquake. The second and third column present pairs for which both seismic phases show similar splitting observations, while for pairs in the fourth column, both phases show different splitting observations.*

total no. of pairs	no. of same pairs (nulls)	no. of same pairs (splits)	no. of discrepant pairs
36	8	11	17

The distribution of these measurements and the derived splitting parameters are displayed in Fig. 4.4a. The stereographic projection shows the results of the SWSMs projected onto the horizontal plane. Figure 4.1 provides a 3D representation of this projection. The positions of the measurements within the stereoplots are determined by the BAZ with respect to north (N), and their incident angle. SKKS phases have larger incident angles

(11° to 13°) and, therefore, plot further away from the centre of the stereoplots compared to SKS (5° to 9°) and PKS (4° to 8°) phases (Creasy et al., 2021).

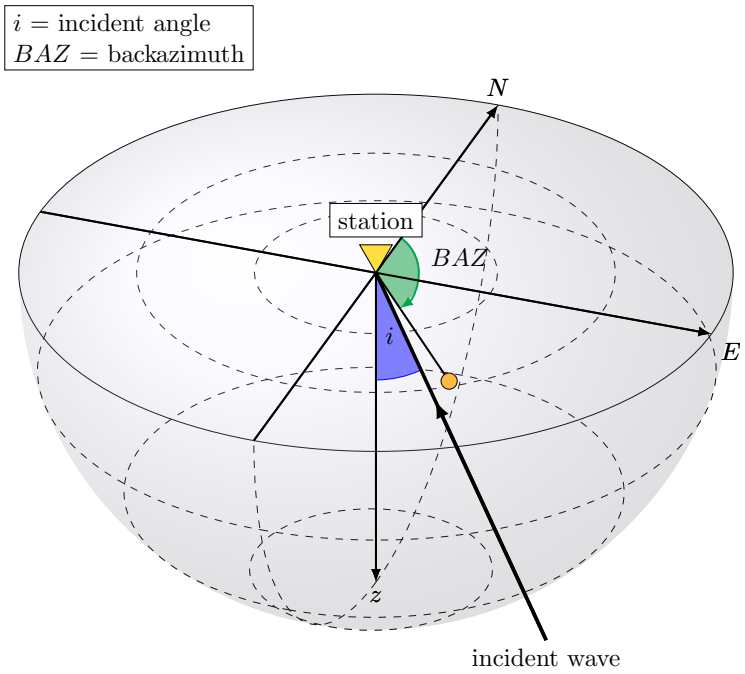

Figure 4.1: *Schematic drawing of the stereographic projection in 3D. The three axes represent north (N), east (E) and the vertical component (z) with the recording seismic station at the point of origin. If an incident wave arrives at the station it pierces through the lower spherical half shell at a certain incident angle i. This point is projected onto the horizontal plane, marked with orange in the plot. Thus, the larger the incident angle the further the point plots away from the centre of the coordinate system. The position of the orange point from north is given by the BAZ of the earthquake.*

In Fig. 4.4a only pairs are included for which at least one measurement is classified as good or fair quality according to the criteria defined in Table 4.6. In the two-dimensional (2D) representation, the data points are plotted according to their observational type. Null measurements are represented as circles, while split measurements are marked with lines. The length of these lines corresponds to the delay time δt between the arrivals of the fast and slow waves. The colour of the line indicates the orientation of the fast polarisation axis, using a cyclic colourbar. In general, a complex pattern can be observed. Towards the west, nulls are observed consistently for SKS phases while SKKS phases show mostly splits. Towards the northeast, the pattern becomes more complex with variations within both splitting type and values of the splitting parameters for both the delay time and the orientation of the fast polarisation direction. Consistent observations are made for the PKS phases with a BAZ of around 30° and an incident angle of around 5°. Those measurements show splitting with a fast polarisation axis of around 60°. But, especially from directions where few SWSMs are obtained (e.g. north, west-northwest or east-southeast), estimating the reproducibility and, thus, the uncertainty of the obtained results is not reliably possible. This is further discussed in Section 4.3.1.

Since the focus of the DeepDyn project lies on the understanding of the LMM, maps of receiver-side piercing points for the previously discussed pairs through the D″ layer are generated to obtain spatial information on the distribution of null and split measurements.

Raypaths are calculated using the *TauP* package (Crotwell et al., 1999) of *Python* and using the point of the raypath that is the closest to the desired depth as the location of the piercing point. The resulting map of the piercing points for a depth of 2900 km can be seen in Fig. 4.2.

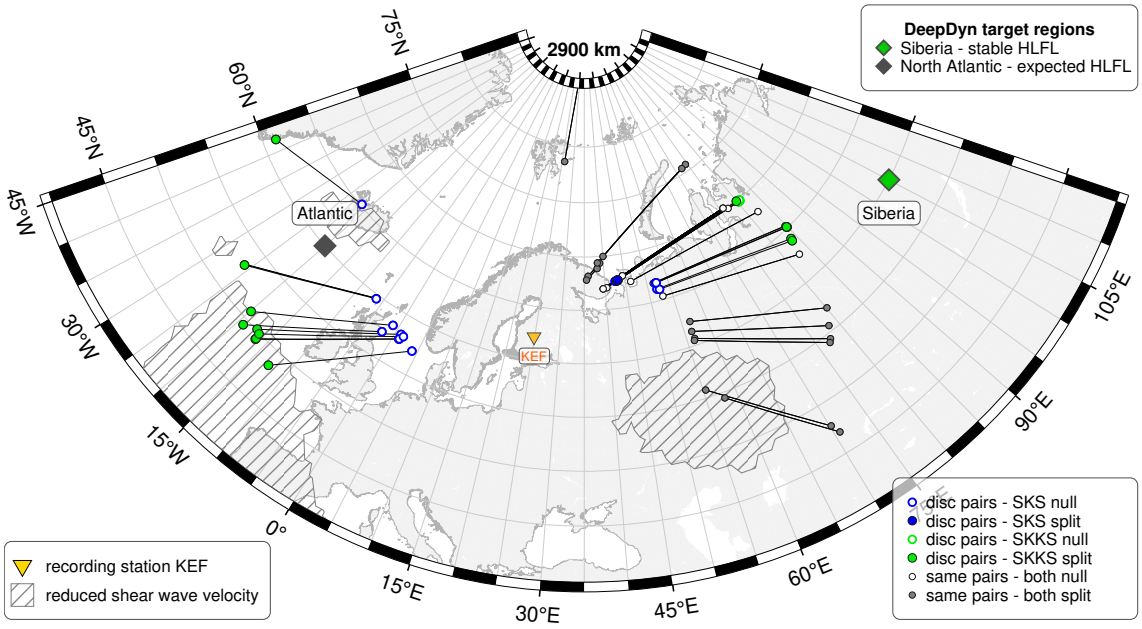

Figure 4.2: *Piercing points at the receiver side of the raypath at* 2900 km *depth. The yellow triangle marks the recording station KEF, the diamonds the two DeepDyn target regions in the LMM and the grey striped areas show regions with reduced shear wave velocity according to Wolf et al. (2023). The colour of the piercing point indicates the wave type and the type of splitting observation.*

The recording station KEF is located in the centre of the map, marked with a yellow triangle. The associated piercing points for the different phases of the same event are connected by a black line. The phases of discrepant pairs are colour-coded according to their phase, with filled dots representing splits and colour-framed circles indicating nulls. Pairs with the same observational type are also displayed with minor dots, here white dots indicate nulls and grey split measurements. In accordance to the stereographic projection in Fig. 4.4a, the piercing points of the SKS phases (blue) plot closer to the recording station while the SKKS phases (green) pierce through the CMB at larger distances to the station. For the piercing points plotting west for the KEF station these might be associated with the HLFL in the North Atlantic (grey diamond). The border of the LLSVP, according to Wolf et al. (2023), plotted beneath the North Atlantic and Spain aligns nicely with the observed splitting in SKKS phases. Previous studies have shown that mantle flow processes take place at the borders of LLVPs and go along with a preferred orientation of minerals (Wang and Wen, 2007; Long and Lynner, 2015; Wolf et al., 2023). This alignment adds up to the observation of anisotropy in this region. The piercings points towards the east of the KEF station can be associated with the target region of Siberia and the reduced shear wave velocity at the Perm anomaly, as indicated in Fig. 4.2 (Long and Lynner, 2015). In general, the observed behaviour of these measurements exhibits strong variations between the observational type and spatial positions. While most pairs with more southern piercing points exhibit splitting of both phases, variations arise in the north. There, all possible combinations of nulls and splits are observed.

Table 4.6: *Quality criteria for the different SWSMs. Criteria are based on the SNR, the variations between the two methods for the splitting parameters ϕ and δt, the confidence interval and the particle motion. Three different quality classes are defined: good, fair and poor. The upper three rows present a null measurement, the lower three rows a split measurement. These criteria follow the criteria defined by Fröhlich (2020).*

observation quality	SNR (SNR_{SC})	$\lvert\Delta\phi\rvert/^\circ$ $\lvert\phi_{SC} - \phi_{RC}\rvert$	$\lvert\Delta\delta t\rvert/$ s $\lvert\delta t_{SC} - \delta t_{RC}\rvert$	confidence interval (95%)	particle motion (SN-WE /Q-T)
null, good	> 10	$[37, 53]$	maximum	no overlap	unchanged
null, fair	> 7	$[32, 58]$	large		linear
null, poor	≥ 3	as soon as one criterium is not fulfilled, and no SWS recognisable			
split, good	> 10	≤ 5	≤ 0.2	small	from elliptical
split, fair	> 7	≤ 20	≤ 1.0		to linear
split, poor	≥ 3	as soon as one criterium is not fulfilled, but SWS recognisable			

4.3 Comparison

Analysing the events discussed in Section 4.1 allows a comparison of phase pairs and splitting parameters obtained by different analysts since Muhammad Dillah (MD) and I, Fiona Dorn (FD), have been studying the dataset of the ScanArray (Thybo et al., 2021) previously studied by Grund and Ritter (2018). By comparing Muhammad Dillah's results and my own, reproducibility of the results can be assessed and uncertainties of the obtained splitting parameters can be estimated. In addition, we evaluate to which degree the results depend on the analyst.

According to Fröhlich et al. (2023), the *SplitLab* software used by Michael Grund (MG) in his data analysis still contained an error related to the temporal alignment of the traces of the components relative to each other. Since the start and end times of the single traces differ due to data storage details, wrongly aligned recording components can lead to wrong particle motions in both the ZNE and the LQT coordinate systems. This misalignment can distort splitting signals and generate artificial ones (Fröhlich et al., 2023). Therefore, by comparing the results of Muhammad Dillah and myself with those of Grund and Ritter (2018) the extent of this error and the impact on previous obtained results can be examined.

4.3.1 Results and discussion

Figure 4.3 presents the colour-coded distribution of epicentres for which at least two phases were measured by one analyst. Even though certain individual events differ between analysts, the general pattern and the backazimuthal distribution agree within all three analysts. Each analyst performed SWSMs on earthquakes with epicentres in South America and Southeast Asia extending up to the Tonga region. The backazimuthal distribution reflects the natural unequal distribution of strong and deep earthquakes across the Earth.

The number of pairs found for each analyst is listed in Table 4.7. Pairs refer to measurements for which an analyst has been measuring at least two XKS phases for the same earthquake. If all three phases are measured for one event, all combinations are listed as separate pairs. Differences in the number of identified pairs may arise from different criteria for classifying measurements as null and split. The table with the criteria used by Muhammad Dillah and myself are listed in Table 4.6. These criteria follow the criteria defined by Fröhlich (2020).

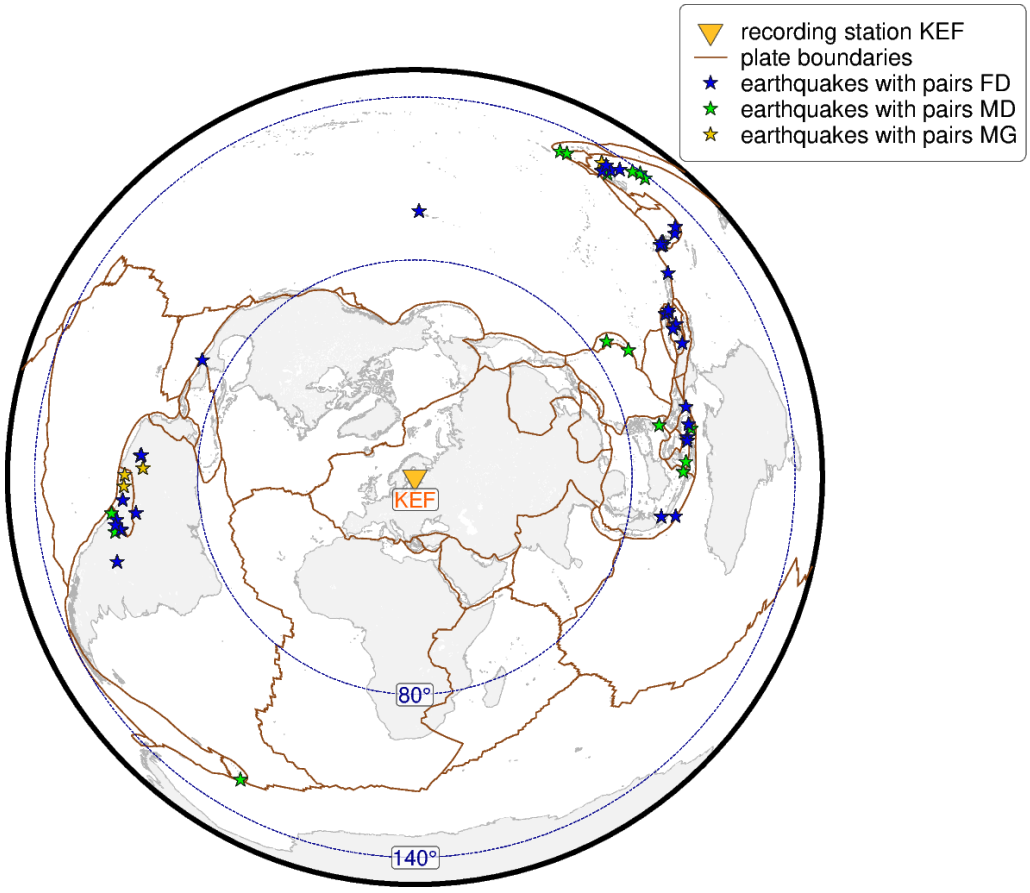

Figure 4.3: *Map of the epicentres of the earthquakes for which at least two XKS phases were measured. The yellow triangle shows the recording station KEF in Finland. The blue circles represent epicentral distances of* 80° *and* 140°*. The different colours of the epicentres corresponds to the different analysts.*

The generally lower number of pairs which have been identified by Grund and Ritter (2018) may result from stricter classification criteria for split or null measurements, including only measurements agreeing for the RC and SC methods within their error bounds (95 % confidence region) and having a SNR of at least five (Grund and Ritter, 2018). In addition, the error in *SplitLab* in the time alignment of the recorded components influences the number of pairs (Fröhlich et al., 2023).

Table 4.7: *Number of pairs for which the different analysts (first column) observed at least two of the analysed XKS phases for the same earthquake. The third and fourth column present pairs for which both seismic phases show similar splitting observations, while for pairs in the fifth column, both phases have different splitting observations.*

analyst	total no. of pairs	no. of same pairs (nulls)	no. of same pairs (splits)	no. of discrepant pairs
FD	36	8	11	17
MD	32	10	10	12
MG	27	4	14	9

Differences in the number of measurements between Muhammad Dillah's and myself primarily result from the classification of near-null measurements (Wüstefeld and Bokelmann, 2007). These measurements show a striking signal for the expected phase with matching values for the absolute values between initial polarisation of the incoming wave and the theoretical BAZ of the corresponding earthquake. However, for the particle motion only a slight elliptical movement is visible. While each analyst classified these cases consistently as null or split measurement within their dataset, differences arise between the analysts. An example for this is displayed in Fig. A.3 in the appendix. Here, the SKKS phase is classified as null by Muhammad Dillah and as split by me, resulting in a discrepant pair in my statistics and in a same pair (both null) in Muhammad Dillah's results.

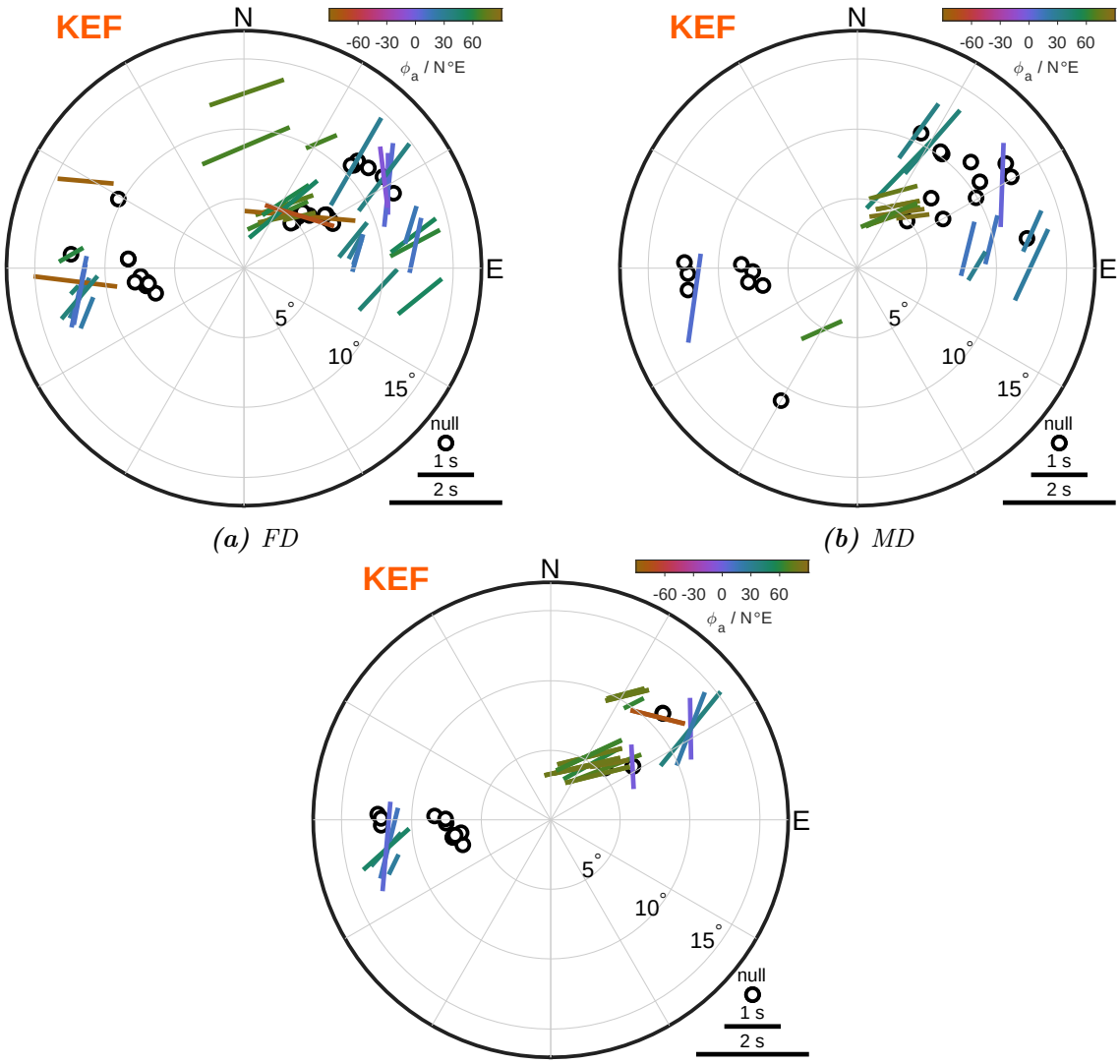

(a) FD *(b) MD*

(c) MG

Figure 4.4: *Stereoplots of pairs of XKS measurements from the three analysts for the KEF station with at least one of the measurements being of good or fair quality. The degrees from the centre point show the incident angle, with SKKS phases showing larger incident angles.*

The results of SWSMs for pairs, in which at least one measurement is classified as good or fair quality (cf. Table 4.6), are displayed in the stereoplots in Fig. 4.4 for all three analysts. The general pattern agrees strongly among the three analysts. The observed splitting

measurements with a BAZ of around 30° to 45° for PKS and SKS phases are consistent across the three analysts. Moreover, the orientation of the fast polarisation axis ϕ and the values for the delay time δt have comparable values for the analyses. A similar level of agreement of the observation can be made for the null measurements of SKS or PKS phases with a BAZ of 240° to 280°. Still, discrepancies occur for the corresponding SKKS phases, for which Michael Grund and I measure mostly splits with a consistent orientation of the fast axis, and Muhammad Dillah measures primarily nulls. The strong variation of splitting parameters with the BAZ has been associated with the presence of a complex seismic anisotropy beneath the station, e.g., multiple layers of seismic anisotropy (Silver and Savage, 1994; Grund and Ritter, 2018). Apart from this in general complex splitting pattern, MD and I observe additional pairs with differing values for the BAZ, resulting in a more scattered distribution.

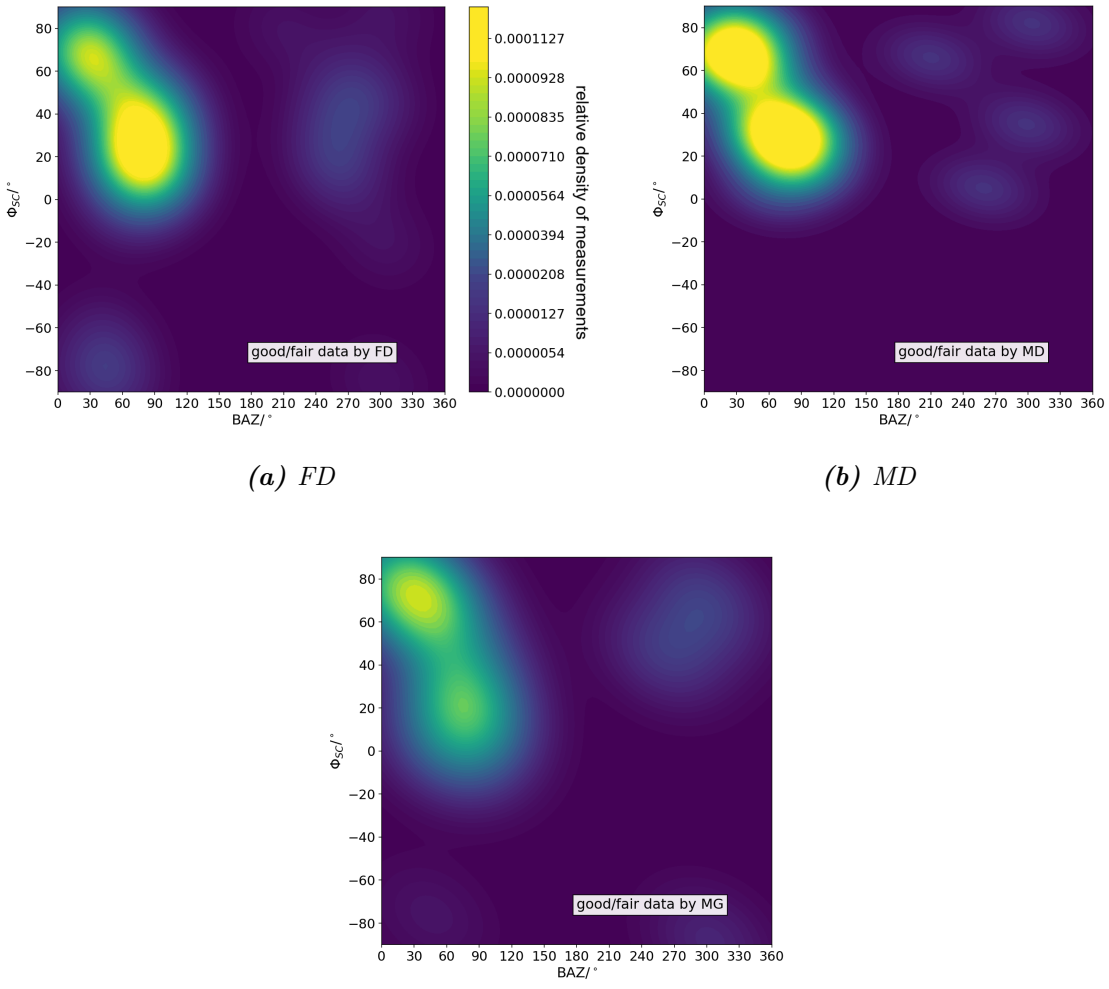

(a) FD *(b) MD*

(c) MG

Figure 4.5: *Heatmaps showing kernel density estimations of the fast polarisation axis for FD, MD and MG. The brighter the colour, the higher is the relative density of measurements. The relative density of measurements are normalised in such way that the integral overall possible values equals 1. The colours in the colourbar of the three figures are the same to make comparison between the figures easier.*

To further estimate the distribution and comparability of the splitting parameters, density function distributions are generated for the fast polarisation axis. These heatmaps can be seen in Fig. 4.5 for the three analysts FD, MD and MG. By comparing the values of the fast polarisation axis across the analysts, it is desired to estimate not only the reliability of the observational type but to further assess the reproducibility of the values of the splitting data. The aim is to study, whether interfering further information regarding parameters of the anisotropy is reliably possible. The value for the fast polarisation axis is plotted on the y-axis, while the x-axis gives the BAZ. The colour of each plot shows the density of measurements at a certain position with brighter colours corresponding to higher densities. The colours in the colourbar of the three figures are consistent to facilitate comparison between the figures. The *seaborn.kdeplot* function of *Python* visualises the distribution of observations in a dataset, similar to a histogram. But instead of using discrete bins a kernel density estimation plot smooths the observations with a Gaussian kernel, producing a continuous density estimate. The curve is normalised so that the integral over all possible values equals 1, which explains the small values in the colourbar. The integration of the density over a given range gives the probability of the value being in that range (Waskom, 2021). In the case of the heatmaps in Fig. 4.5 this gives the proportion of measurements out of all measurements that lie in a certain range. The general patterns in the three figures agree nicely, with a high density represented at angles up to 100° for the BAZ and for values of the fast axis between 15° to 45°. A second maximum can be seen for smaller BAZs and higher values for the fast axis around 60° to 70°. The density at this maximum is lower for Muhammad Dillah and myself but higher for Michael Grund. In general, scattering for different measurements appears to be more pronounced for this maximum than in the maximum at larger BAZs. Another accumulation of measurements with lower density can be observed for BAZs above 210° and similar values for the fast axis as the higher maxima. Due to less measurements in this BAZ range, scattering of values between the analysts becomes more pronounced. This gets particularly striking for small accumulations of values for the fast axis of around $-80°$ to $-70°$ which are only visible in the density function distribution of Michael Grund and myself.

Analogue to Fig. 4.2, a map of the piercing points through the CMB on the receiver side is generated including the results obtained from all three analysts (Fig. 4.6). The addition of pairs from Muhammad Dillah and Michael Grund increases the number of observations for both discrepant and same pairs. Especially towards the west, the observation of splits for the SKKS phase and nulls for the SKS phase agrees strongly among the analysts. The predominantly split observations for the SKKS phases align nicely with the boundary of the LLSVP according to Wolf et al. (2023).

Towards the east, the observation of mostly same pairs with both phases being splits remains consistent, with only one discrepant pair for the region of the reduced shear wave velocity at the Perm anomaly. The intricate pattern observed towards the northeast of the KEF station becomes even more complex with additional pairs measured by Michael Grund and Muhammad Dillah, including the observation of split PKS phases.

4.3.2 Influencing factors

By comparing phase pairs and splitting parameters obtained by different analysts, we study both objective and subjective aspects that are crucial to consider when performing SWSMs. A major factor influencing the quality of the SWSMs are the selected filter parameters. Since observations of SWSMs are inherently challenging, different filter parameters (bandwidth and corner frequencies) are selected for the different earthquakes in the dataset. The lower frequency bound ranks between $[0.02, 0.066]$ Hz, the upper between $[0.16, 0.20]$ Hz. During the analysis of the earthquakes, it is observed that varying the corner frequencies and the

bandwidth cannot only impact the quality of the observation but can also change the type of observation. By narrowing down the bandwidth of the filter excessively, only a limited range of frequencies passes the filter, naturally creating a time and phase offset to each other. This can cause an elliptical particle motion and therefore splitting observations might be influenced artificially.

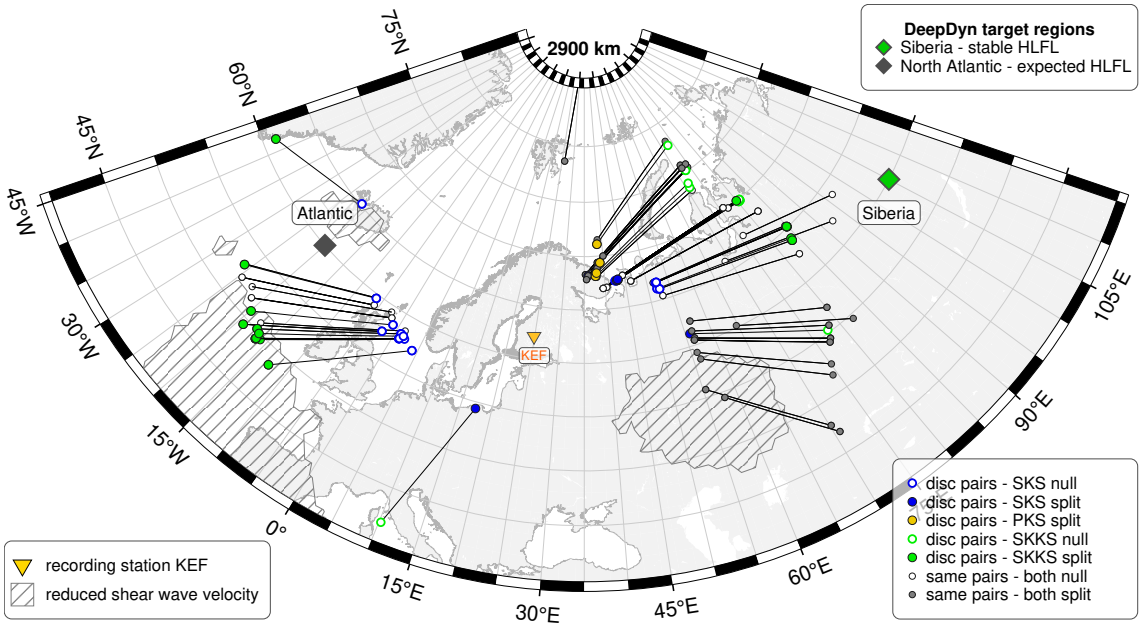

Figure 4.6: *Piercing points at the receiver side of the raypath at* 2900 km *depth. The yellow triangle marks the recording station KEF, the diamonds the two DeepDyn target regions in the LMM and the grey striped areas show regions with reduced shear wave velocity according to Wolf et al. (2023). The colour of the piercing point indicates the wave type and the type of splitting observation.*

Another relevant factor is the length of the time window, compared to the dominant period of the seismic phase, in which SWS is measured. This window is manually selected for each phase. It depends in first order on the observable signal on the Q-component after the rotation. Typically, a window length of 15 s to 20 s is selected, while considering the arrival of other phases during the same time and trying to keep a time gap of at least 5 s to these phases.

While Michael Grund observed phases at an epicentral distance of $[80, 140]^\circ$ with magnitudes $M_W > 5.8$, we increased the number of available earthquakes for the analysis by using all events with $M_W \geq 5.5$ in the same observation range. However, especially in the interval $[80, 90]^\circ$, we encounter difficulties to reliably identify the desired phase, as SKS and S phases arrive almost at an identical time in this epicentral distance. This can also be seen in Fig. 4.7c. The violet and cyan dots mark the arrival time of the S and ScS phases which arrive almost at the same time as the dark blue SKS phase and the green SKKS phase. The corresponding raypaths for an epicentral distance of 87° are shown in Fig. 4.7a. Other phases that particularly interfere with the desired phases are depth phases propagating from the hypocentre upwards and being reflected at the free surface (see Fig. 4.8).

As mentioned in Section 3.3, systematic deviations from the initial polarisation (theoretical BAZ) and a particle motion not parallel to the BAZ might indicate a possible misidentification of a seismic phase, interference with noise or a misorientation of the seismic sensor.

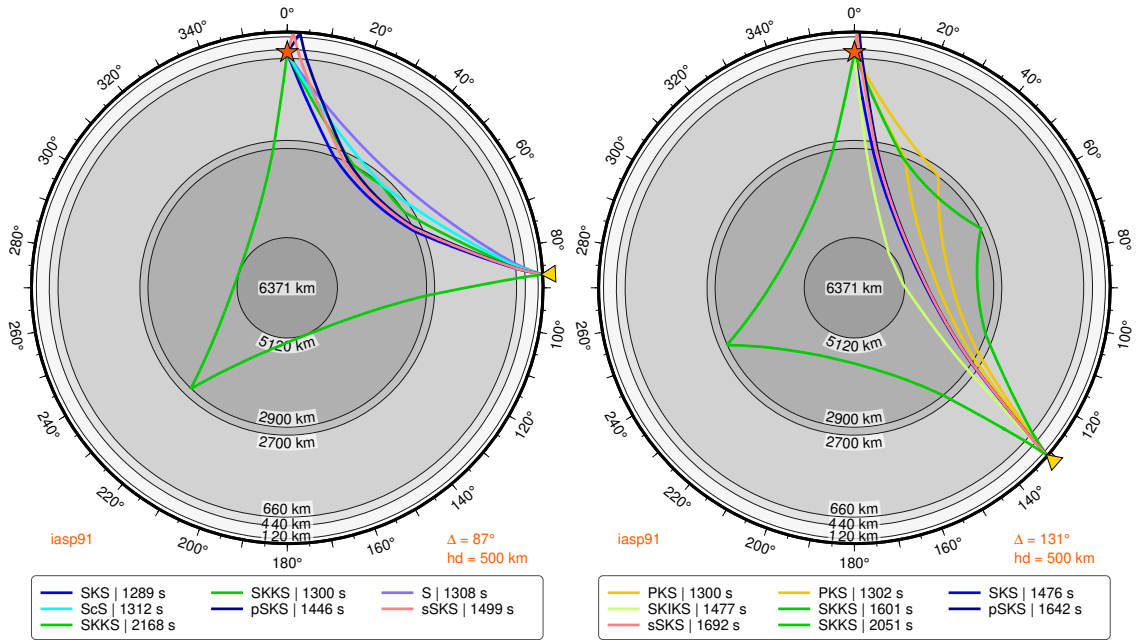

(a) *Raypaths of the occurring phases for an epicentral distance of* 87°.

(b) *Raypaths of the occurring phases for an epicentral distance of* 131°.

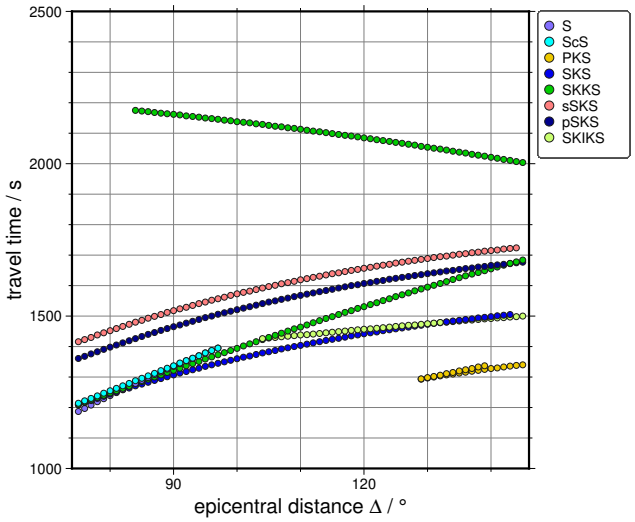

(c) *Traveltimes of the occurring phases as function of the epicentral distance.*

Figure 4.7: *Raypaths and traveltimes for varying epicentral distances for the desired XKS and interfering phases for an earthquake with a hypocentral depth of* 500 *km. In the parts (a) and (b) the red star represents the hypocentre and the yellow triangle the recording station.*

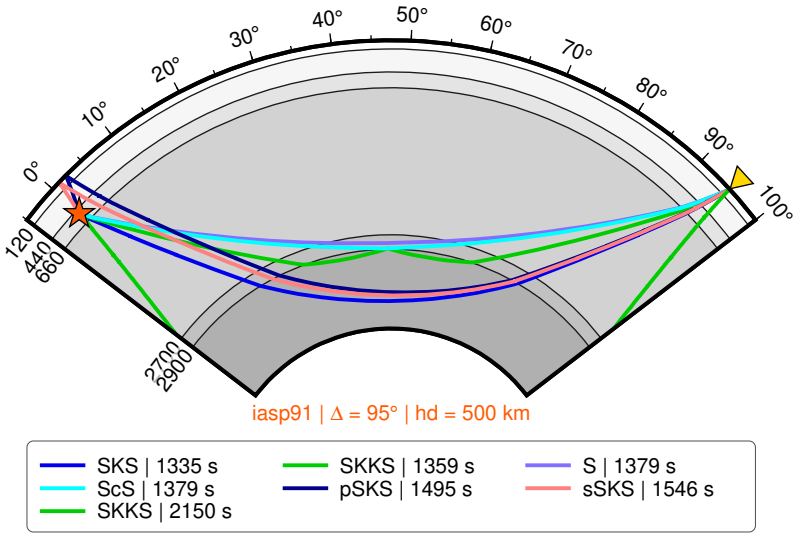

Figure 4.8: *Raypaths of various seismic phases for an epicentral distance of* 95°*. The red star represents the hypocentre at a depth of* 500 km *and the yellow triangle the recording station.*

On the other hand, different analysts also encounter several subjective factors when deciding whether a seismic phase contains a measurable SWS signal or not. Defining an objective classification table, which can be found in Table 4.6, gives criteria according to which the observations can be classified into different splitting observations and quality classes. The classification depends on the SNR, differences in the results of the two used methods and observable elliptical or linear particle motions. Nevertheless, there are still measurements very close to the limit of observations or at the boundary between different quality criteria or even different types of observations. These measurements are referred to as unclear near-null measurements according to Wüstefeld and Bokelmann (2007). Depending on the analyst, these measurements might be classified in different quality classes or even different types of observations. Additionally, subjective human factors play a non-negligible role in SWSMs and the classification of type and quality. Decision-making might depend on the time of the day, day of the week, the amount of previously observed SWS signals and the analyst's mood. For instance, after measuring several good quality SWS signals, the chances of discarding a poor quality but measurable SWS signal are higher than the chances of discarding the same signal after having studied several phases without showing SWS.

4.3.3 Consequences for the following work

By studying the same dataset for the KEF station in the HE network in Finland by three different analysts, we assess the reliability and reproducibility of SWSMs. Comparison of the results from different analysts highlights the subjective factors involved in classifying a measurement as split or null and determining its quality. As discussed in Section 4.3.2, different factors influence the classification of measurements as good, fair or poor quality and can even impact the observational type. For the following work of this thesis, these factors are taken into account to ensure robustness of the results.

One key learning of this work is, to only use clearly visible phases and onsets. Each measurement of SWS is of great importance for the following interpretation since only a limited amount of pairs can be found. A poorly measurable XKS phase is not only time-consuming in analysing, but an incorrectly associated phase or a measurement indicating a wrong observational type has a strong influence in the resulting interpretation of the

underground model. Especially, when not only the observational type but also the splitting parameters will be interpreted, high quality data is necessary. Otherwise the sources of uncertainty are larger than the measurable signal and variations between different analysts are larger than the actual differences of the measured values.

Chapter 5

Shear wave splitting measurements beneath Siberia

5.1 Spatial distribution of possible station-earthquake pairs

To get the most comprehensive picture possible of the HLFL and its potential anisotropic signature beneath Siberia, I study rays passing through the LMM in different propagation directions and at varying incidence angles. However, certain requirements with respect to epicentral distance, hypocentral depth and magnitude need to be fulfilled by the earthquakes and the earthquake-station configuration to be able to measure SWS of XKS phases.

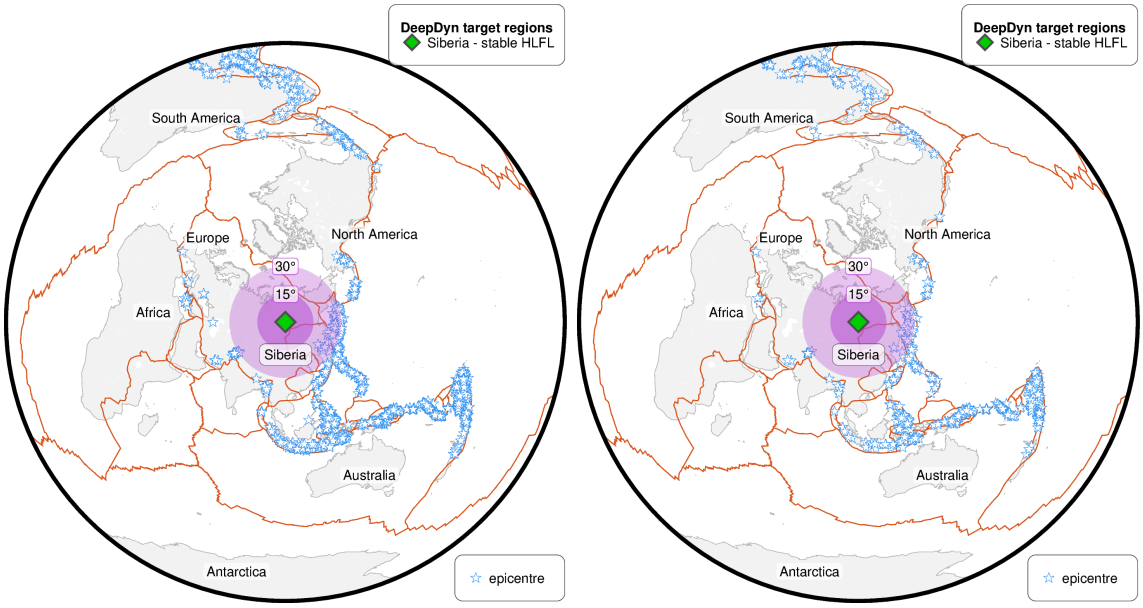

Figure 5.1: *Number and distribution of EQs with a hypocentral depth of at least* 50 km *and a moment magnitude of* $M_W \geq 5.5$ *(left) and* $M_W \geq 6$ *(right) between* 2010/01/01 *and* 2024/01/01. *Due to the significant decrease in events a limit of* $M_W > 5.5$ *is chosen. Earthquake data is taken from the USGS-earthquake catalogue (U.S. Geological Survey, 2025).*

5.1.1 Suitable earthquakes

Reliable measurements of SWS require a selection of earthquakes that fulfil certain aspects regarding their hypocentral depths and magnitude. From the studies at the KEF station, discussed in Section 4.3.2, a high moment magnitude is preferable, as the record sections show a better SNR. In Fig. 5.1, the comparison between the number and distribution of earthquakes with a hypocentral depth $z \geq 50\,\text{km}$ and magnitudes $M_W \geq 5.5$ (left) and $M_W \geq 6$ (right) is presented. Increasing the limit for the moment magnitude from $M_W \geq 5.5$ to $M_W \geq 6.0$ strongly reduces the number of available earthquakes in the interval between 2010/01/01 until 2024/01/01 from 1514 to 527 events and limits their spatial distribution. At the same time, the long rupture duration of very strong earthquakes might result in an undesired signal of the SKS phase to be hidden in the long coda of the S phase.

Similarly, constraints on the hypocentral depth can be discussed. An increase in the limit of the hypocentral depth from 20 km to 50 km for earthquakes with moment magnitudes of $M_W \geq 5.5$ reduces the number of events from 3204 to 1514 (cf. Fig. 5.2). However, studies at the KEF station (see Section 4.3.2) have shown striking improvements in SNR for earthquakes with greater hypocentral depth.

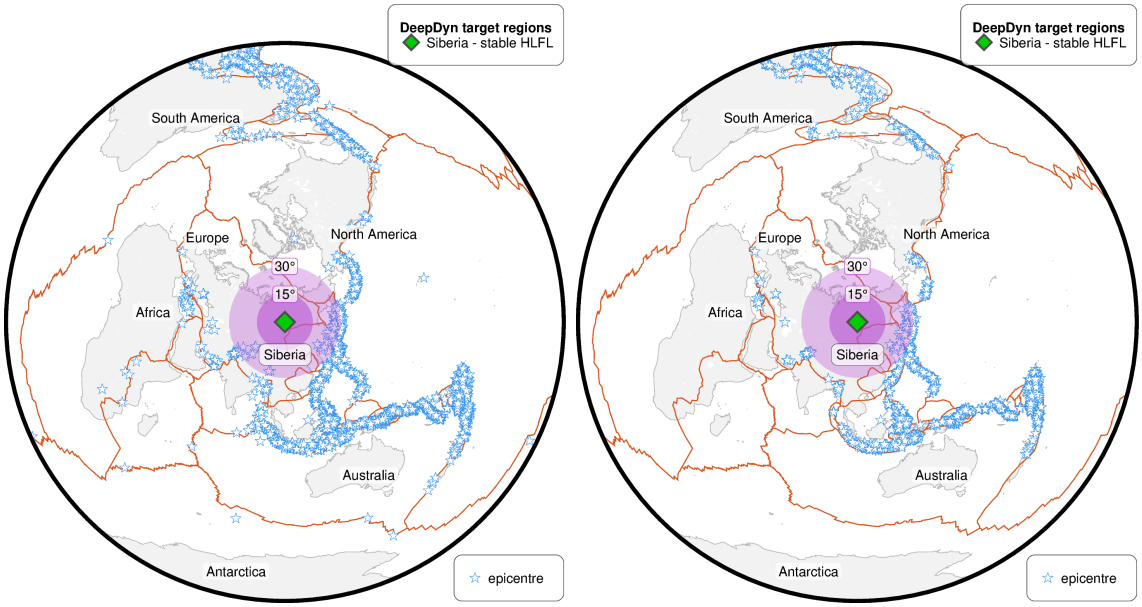

Figure 5.2: *Number and distribution of EQs with moment magnitude of a* $M_W \geq 5.5$ *and a hypocentral depth of at least* 20 km *(left) and* 50 km *(right) between* 2010/01/01 *and* 2024/01/01. *A significant decrease in the number of events can be observed. Earthquake data is taken from the USGS-earthquake catalogue (U.S. Geological Survey, 2025).*

Therefore, in the following, earthquakes with a depth greater than 50 km and a magnitude above 5.5 are selected.

Table 5.1: *Parameters of EQs for SWSMs beneath Siberia.*

epicentral distance/ °	$89 <$ distance < 141
magnitude M_W	> 5.5
depth/ km	> 50

5.1.2 Selection of recording stations

To find potential stations that are located in the desired epicentral distance to suitable earthquakes, both temporary stations of seismic arrays and permanent stations are taken into account and piercing points are calculated for all earthquakes that meet the criteria listed in Table 5.1. The raypaths through the Earth for all events after 1995/01/01 are calculated by using the *tauP* package of *obspy* (Crotwell et al., 1999). The distance between the coordinates of the piercing point through the CMB of the upcoming raypath and the centre of the HLFL beneath Siberia is determined. If this distance is less than 15° the earthquake is classified as a suitable earthquake-station pair. The spatial distribution of the analysed stations can be seen in Fig. 5.3. Of these seismic stations, those with a significant number of suitable earthquakes are classified as potential stations with usable recordings. The detailed station parameters of all analysed stations, together with the number of suitable earthquake recordings per station, can be found in Table A.1 in the appendix.

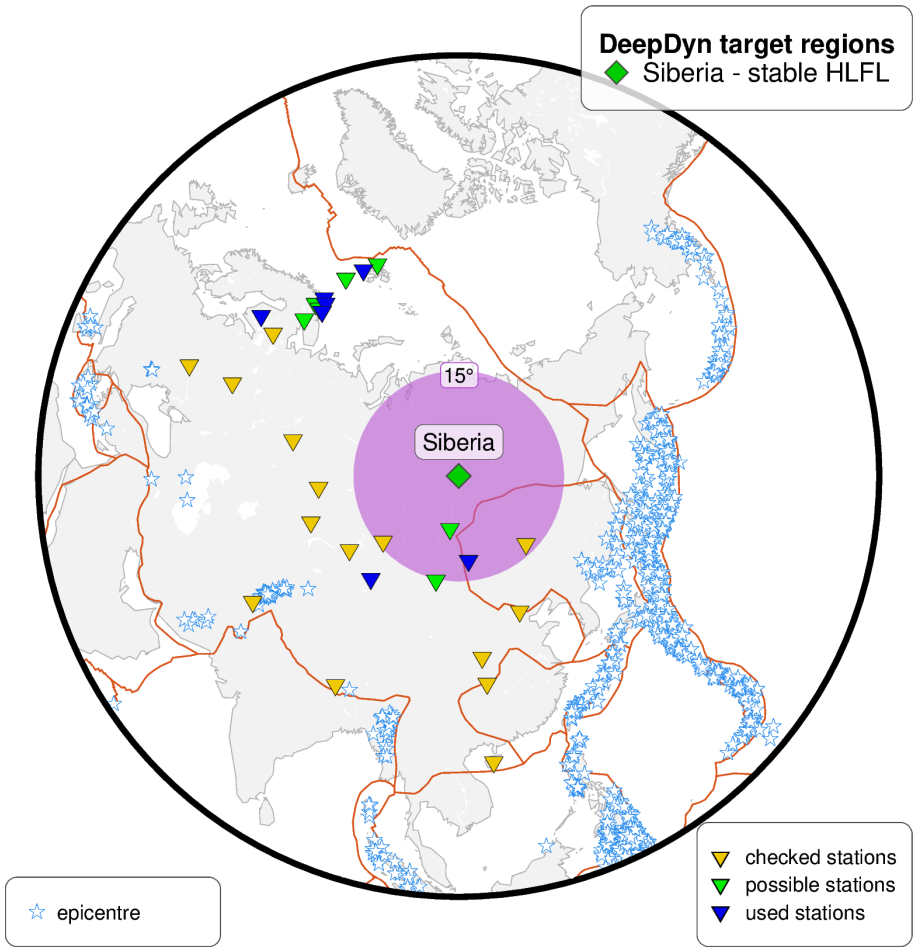

Figure 5.3: *Map of the possible stations (green triangles) out of all analysed stations to study the HLFL beneath Siberia. The green diamond marks the centre of the target region and the light purple area the region of* 15° *around it. The epicentres of suitable earthquakes, taken from U.S. Geological Survey (2025), are plotted in blue stars.*

Seismic stations located in Russia and run by Russian institutions are not included in the analysis, despite their large number of suitable events, since due to the war in Ukraine, no seismic data can be requested for those stations.

Table 5.2: *Parameters of the recording stations to study the HLFL beneath Siberia.*

station code	network code	longitude /° N	latitude /° E	operation time	sensor type
HSPB	PL	15.5332	77.0019	2007/09/22 -	STS-2
ULN	IU	107.0532	47.8651	1994/10/31-	STS-1
WMQ	IC	87.7049	43.8138	1995/09/23 -	STS-1
SA01	1G	25.82	71.11	2013/09/26 - 2016/05/11	STS-2
SA02	1G	28.24	71.06	2013/09/25 - 2016/05/10	STS-2
SA05	1G	31.01	70.28	2013/09/24 - 2015/05/19	STS-2

To select the seismic stations for SWSMs during this thesis, a geometry with varying spatial distributions of raypaths and different propagation directions and angles is preferred, as anisotropy describes the directional dependence of a property. Therefore, stations in the north of Europe as well as in Central Asia are selected. In general, permanent stations are preferred because of their longer time spans of seismic data compared to temporary deployments of stations (Creasy et al., 2021). Together with the availability of the recordings, the total number of suitable earthquakes and the quality of the earthquakes (especially the magnitude and depth), the three permanent stations HSPB (network: PL), ULN (network: IU) and WMQ (network: IC) are selected. Additionally, I choose three stations of the ScanArray: SA01, SA02, SA05 (network: 1G) to test the reliability of the SWS method. Due to the geographical proximity of the ScanArray stations similar results are expected. The six selected stations and their parameters are shown in Table 5.2. The parameters of the 3C seismograms and the number of downloaded event recordings can be found in Table 5.3.

Table 5.3: *Parameters of the 3C seismograms at the recording stations to study the HLFL beneath Siberia.*

station code	data-centre	channel-code	sampling rate/ Hz	time span of EQ	total no. of EQ
HSPB	GFZ	HH?	100	2010/02/15 - 2023/11/22	211
ULN	IRISDMC	BH?	20	1995/02/08 - 2023/10/07	167
WMQ	IRISDMC	BH?	20	1995/10/21 - 2023/12/07	111
SA01	GFZ	HH?	100	2013/11/03 - 2016/04/26	34
SA02	GFZ	HH?	100	2013/11/03 - 2016/04/26	40
SA05	GFZ	HH?	100	2013/11/03 - 2015/05/05	20

The spatial configuration between the stations and events, together with the piercing points through the LMM at the recorder site for both SKS and SKKS phases, can be seen in Fig. 5.4. As expected, the piercing points for the SKS phases plot closer to the recording stations than the SKKS phases. Depending on the coordinates of the recording stations, two main source regions can be identified for the chosen earthquakes. For recording stations in Northern Europe (Figs. 5.4a and 5.4d to 5.4f), earthquakes in Southeast Asia up to Tonga are used. This results in raypaths passing through the target region from southeast to northwest. For most of the selected events, the piercing points for the SKKS phases are closer to the centre of the HLFL beneath Siberia.

For the recording stations ULN, Mongolia, and WMQ, China, (Fig. 5.4b and Fig. 5.4c) a different spatial orientation can be seen for the raypaths. The selected earthquakes for these stations have epicentres in Central and South America, leading to raypaths of the analysed phases orientated from north to south through the target region. For the ULN station configuration, most piercing points are nicely centred around the HLFL, while the piercing points for the WMQ station are slightly towards west.

Hence, combining the six selected stations gives us the possibility to study the HLFL beneath Siberia from different directions and different angles, since SKS, PKS and SKKS phases penetrate the D″ layer at different angles.

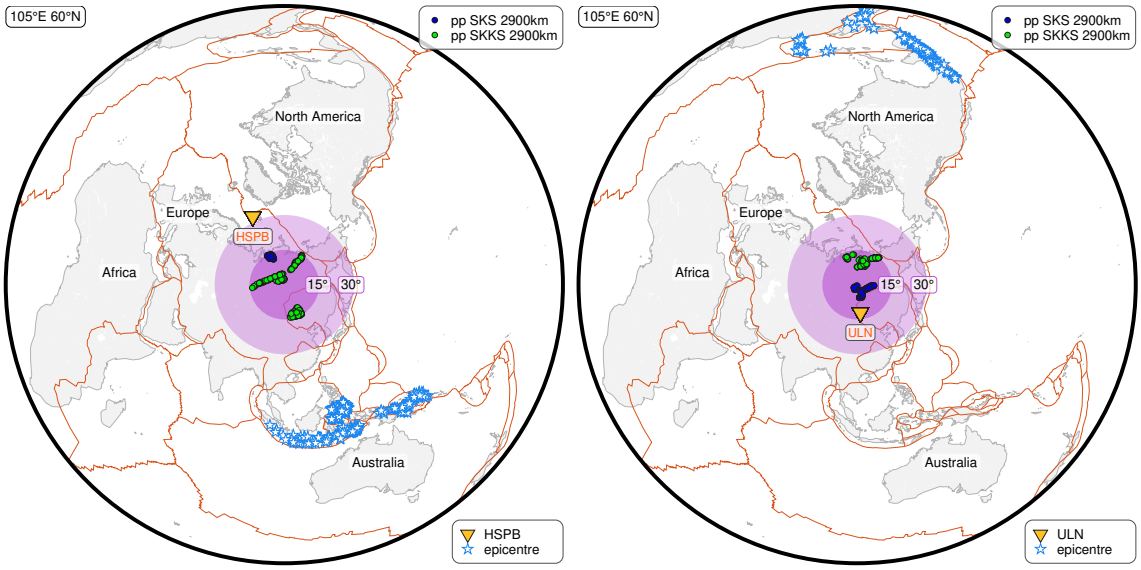

(a) HSPB

(b) ULN

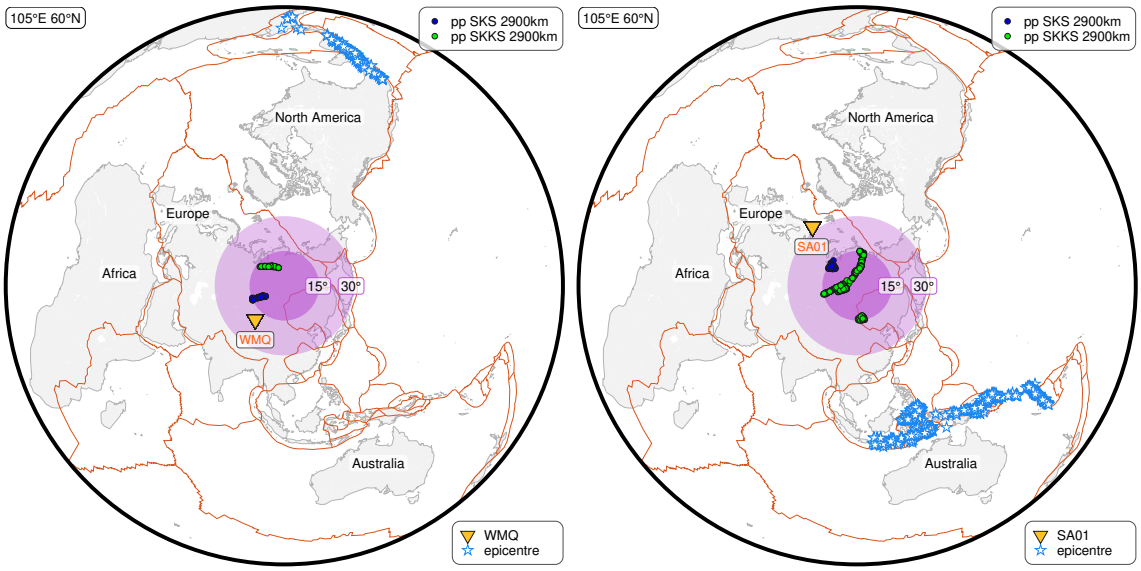

(c) WMQ

(d) SA01

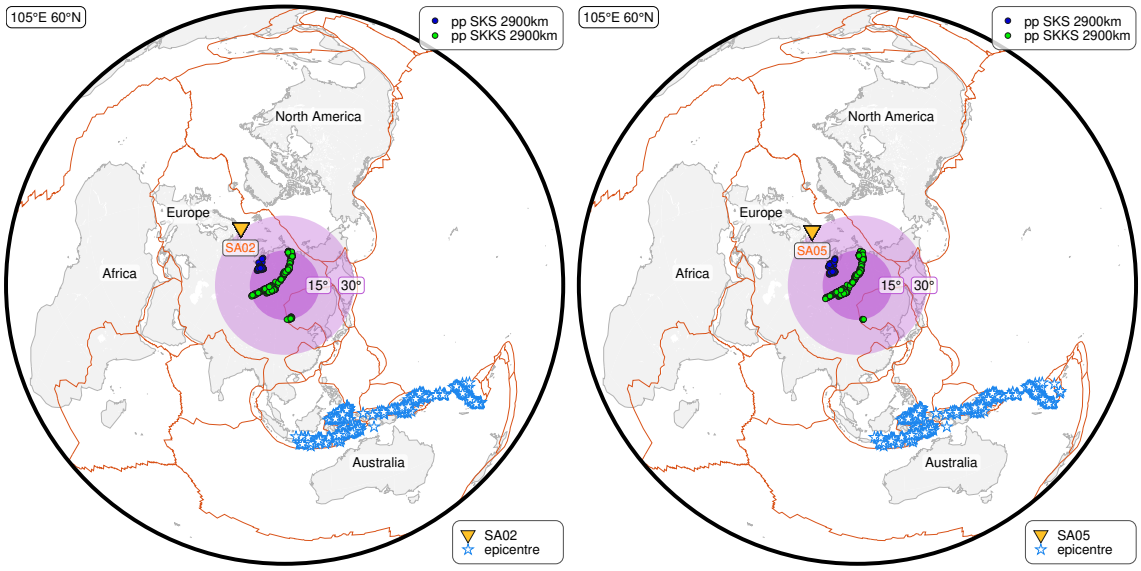

(e) SA02 *(f) SA05*

Figure 5.4: *Spatial configuration of possible EQs for the selected recording stations. Possible earthquakes refer to earthquakes that have recorder-side piercing points (pps) within the coloured* 15° *radius of the centre of the HLFL beneath Siberia. The information about the earthquakes is taken from the USGS earthquake catalogue (U.S. Geological Survey, 2025) and the raypaths are calculated using the tauP package (Crotwell et al., 1999).*

5.2 Adjusted methods for measuring shear wave splitting

The SWSMs are performed in *MATLAB* by using the *SplitLab* program (Wüstefeld et al., 2008) as discussed in Section 3.2 and 3.3. For each station the possible earthquakes that fullfil the criteria defined in Table 5.1 are selected. The seismic traces are requested via the *obspy.client* function (Beyreuther et al., 2010) in *Python*. Then, a new project file is created for each station as described in Section 3.2.1. The only modifications are the constrains on the suitable earthquakes which are mentioned in Table 5.1. The general process of the analysis of the data, orientated on the theoretical arrival time of the phase and the selection of filter parameters, is performed in the same way as for the KEF station (cf. Section 4.1). Unlike the SWSMs at the KEF station, all earthquakes here are analysed to measure either a SWS for the SKS or the PKS phase. Only if a successful measurement can be performed for at least one of the two phases, the SKKS phases are analysed, since we are only interested in phase pairs. The classification criteria (cf. Table 4.6), as defined by Fröhlich (2020), are continued to be used with the difference that every signal that cannot clearly be classified as null or split is discarded to improve the reliability of the method and exclude possible near-null measurements (Wüstefeld and Bokelmann, 2007).

For the WMQ station, a potential misorientation is identified by a similar behaviour of the signal on the R- and T-components as well as a 90° offset between the SC and RC method in the particle motion of the *diagnostic* plot (Fig. A.4 and Fig. A.5). This occurred for earthquakes after 2013/06/16, affecting 33 out of the 111 requested earthquakes. No information regarding a misorientation of the seismometer is mentioned in the metadata of the station, but the dates go along with a change of the recording seismometers at the station[1] (National Science Foundation's Seismological Facility for the Advancement of Geoscience, 2018).

[1]The metadata is taken from http://ds.iris.edu/mda/IC/WMQ/. Last seen: 2015/03/10.

Chapter 6

Results and discussion

In this chapter, the results obtained for the SWSMs at the different stations are presented and discussed for each station individually. Subsequently, the results from all stations are discussed and compared to an underlying model of the Earth's magnetic field and a seismic tomography of the variations in shear wave velocity in 2900 km depth (Section 6.2). The results are also compared to previously performed studies of SWS in the area (Section 6.3). The second part of the discussion (Section 6.4) focuses on the evaluation of the SWS method, assessing the total number of measured *X*KS phase pairs and the reproducibility of SWSMs by different analysts and at proximal stations.

6.1 Results at individual stations

Measurements of SWS are performed for the six stations as outlined in Section 5.1.2. The resulting individual single splitting measurements, sorted by phases and observational types, can be found in the appendix (Table A.2 - Table A.7). The corresponding stereoplots are displayed in Fig. A.6. Since the aim of this thesis is to better understand the anisotropy in the LMM, the focus of this section lies on the earthquakes for which at least two of the *X*KS phases haven been measured. Striking differences occurred in the total number of pairs found at each station and the observational types. These differences are discussed in detail in the following sections.

6.1.1 HSPB station

For the HSPB station, SWSMs are successfully performed with 49 SKS phases and zero PKS phases out of the 216 events (Table A.2). Studying the arriving SKKS phases a total of 10 phase pairs are measured. These split up equally into discrepant pairs (5) and same pairs (5) (Table 6.1). For the same pairs, both null-null and split-split observations are measurable.

The stereoplots with the obtained splitting parameters for the pairs for which at least one of the two SWSMs is of good or fair quality (Table 4.6) can be seen in Fig. 6.1. The events group into two groups with slightly different BAZs. For events with smaller BAZs (plotting further north) most cases exhibit splits. Especially, the SKKS phases at greater incidence angles demonstrate consistent splitting observations with comparable delay times and a similar orientation of the fast axis. For the SKS phases, both nulls and splits are observed, with the fast axis remaining consistent across different split measurements. The events with larger BAZs display only nulls for SKS, and both nulls and splits with very short delay times for SKKS.

Table 6.1: *Number of pairs for which at least two of the analysed XKS phases were observed for an earthquake at the station HSPB. The second and third column present pairs for which both seismic phases show similar splitting observations, while for pairs in the fourth column, both phases show different splitting observations.*

total no. of pairs	no. of same pairs (nulls)	no. of same pairs (splits)	no. of discrepant pairs
10	2	3	5

The small backazimuthal range for which measurements are obtained is a consequence of the boundary conditions regarding the distance of the recorder side piercing point in the LMM from the centre of the HLFL (Fig. 5.4a). The epicentres of the earthquakes for which we can measure pairs of SWS are displayed in Fig. 6.2. A comparison of this figure with the plot of all possible earthquakes for the HSPB station in Fig. 5.4a reveals that pairs of *X*KS phases can be observed from both the eastern and the western end of the possible events. This is beneficial, since the resulting piercing points in the LMM, thus, spread out further, as it can be seen in Fig. 6.3. The figure displays a map of the piercing points of the measured pairs in 2900 km depth. The recording station HSPB is marked with a yellow triangle and the centre of the HLFL with a green diamond. The grey striped area marks the region of reduced shear wave velocity at the Perm anomaly according to Wolf et al. (2023). Phases that belong to the same event are connected with a black line. The colours of the piercing points, calculated with the *tauP* package (Crotwell et al., 1999) in *Python*, correspond to the different seismic phases and splitting observations. The coloured dots (blue and green) refer to a discrepant pair. The different BAZs can be clearly distinguished by an accumulation of piercing points further south and north. The general behaviour of the pairs appears to agree. Though, it is striking that for the discrepant pairs, the SKS phases do not show splitting while the SKKS phases, which are closer to the centre of the HLFL, find splitting.

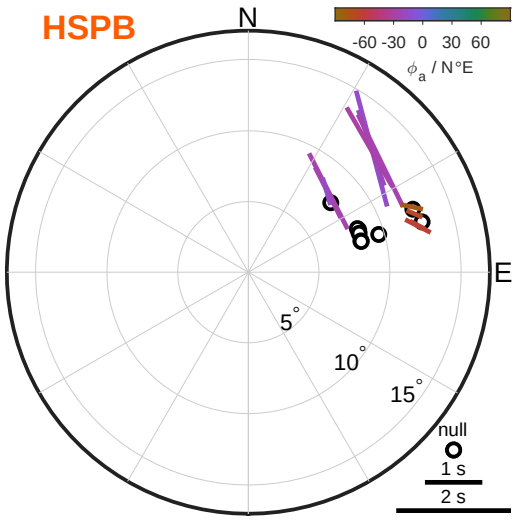

Figure 6.1: *Stereoplot of pairs of XKS measurements for the station HSPB with at least one of the measurements being of good or fair quality. The positions of the markers indicate the BAZ and the degrees from the centre point show the incident angle. The form of the marker depends on the observational type. For further explanation of the projection see Fig. 4.1.*

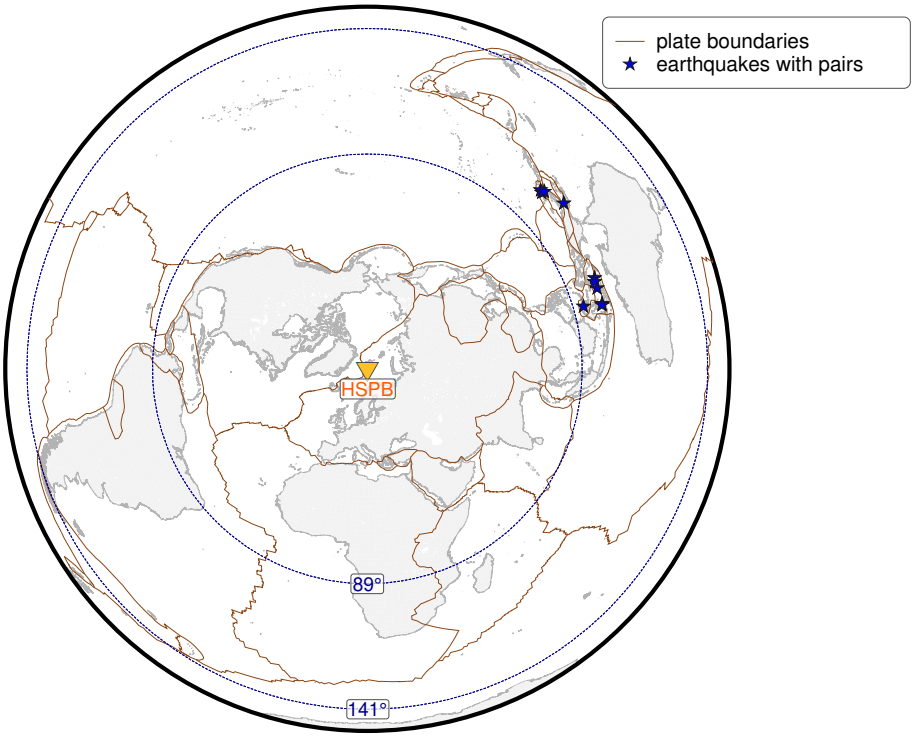

Figure 6.2: *Map of the epicentres of the earthquakes for which at least two XKS phases were measured. The yellow triangle shows the recording station HSPB. The blue circles represent epicentral distances of* 89° *and* 141°.

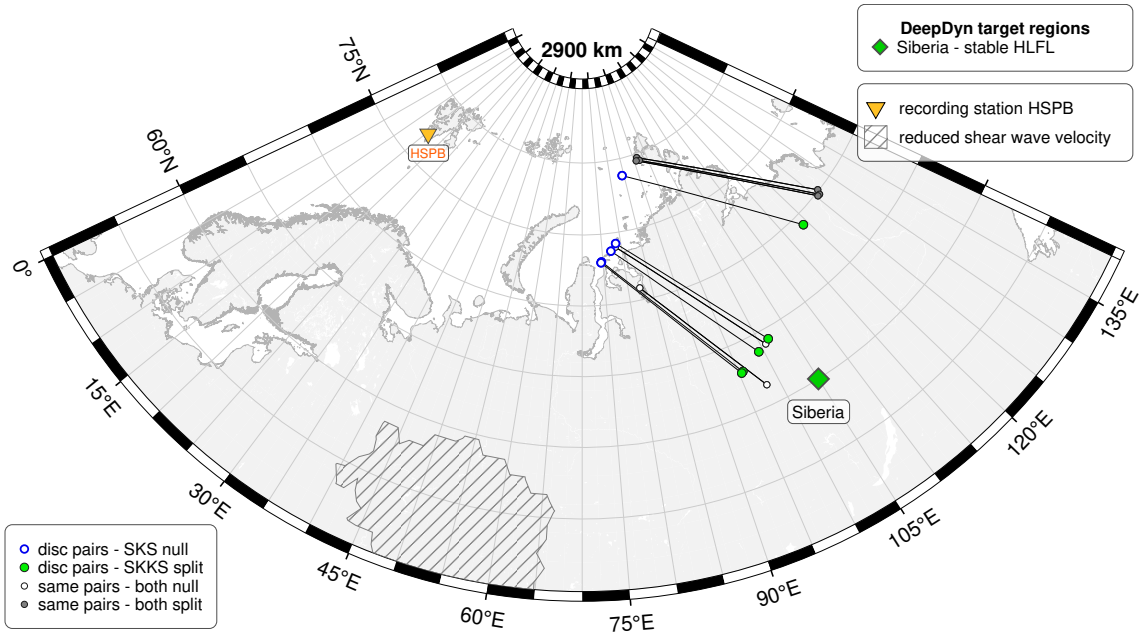

Figure 6.3: *Piercing points at the receiver side of the raypath at* 2900 km *depth for the HSPB station. The yellow triangle marks the recording station HSPB and the green diamond the DeepDyn target region beneath Siberia. The data of the region with reduced shear wave velocity is taken from Wolf et al. (2023). The colour of the piercing point indicates the wave type and the type of splitting observation.*

6.1.2 ULN station

Measurements at the ULN station in Mongolia result in a total of seven pairs out of the 168 events that are analysed. However, only two of these pairs are discrepant and can thereby be attributed to an influence from the LMM (cf. Table 6.2). Nevertheless, from the pairs with the same type of splitting observation with similar BAZs and thus close spatial proximity, insights can be gained regarding the reliability of the method. This will be further discussed in Section 6.4.3. For the ULN station a very narrow range of BAZs around 20° is observed, where both nulls and splits are seen for both phases (Fig. 6.4). The nulls concentrate slightly further north than the splits. Regarding the orientation of the fast polarisation axis and the delay time, variations between the events are larger than for the HSPB station (Fig. 6.1). Examinating the epicentres of the events for which SWSMs have been performed successfully (Fig. 6.5), we can see that earthquakes with larger epicentral distances ($\Delta = [130, 141]°$) are not appearing in the map. Despite the advantage of these larger epicentral distances in terms of PKS occurrence, difficulties arise in measuring the SKS phase. As it can be seen in Fig. 4.7c starting at epicentral distances of around 125°, SKIKS and SKS phases arrive simultaneously, potentially leading to phase interferences and incorrect picking of phases or onsets. At epicentral distances exceeding 135°, an additional difficulty occurs due to the coincident arrival time of pSKS and SKKS phases.

Table 6.2: *Number of pairs for which at least two of the analysed XKS phases were observed for an earthquake at the station ULN. The second and third column present pairs for which both seismic phases show similar splitting observations, while for pairs in the fourth column, both phases show different splitting observations.*

total no. of pairs	no. of same pairs (nulls)	no. of same pairs (splits)	no. of discrepant pairs
7	1	4	2

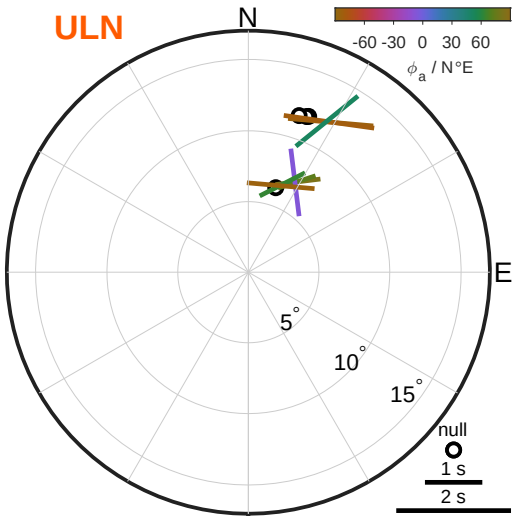

Figure 6.4: *Stereoplot of pairs of XKS measurements for the station ULN with at least one of the measurements being of good or fair quality. The positions of the markers indicate the BAZ and the degrees from the centre point show the incident angle. The form of the marker depends on the observational type. For further explanation of the projection see Fig. 4.1.*

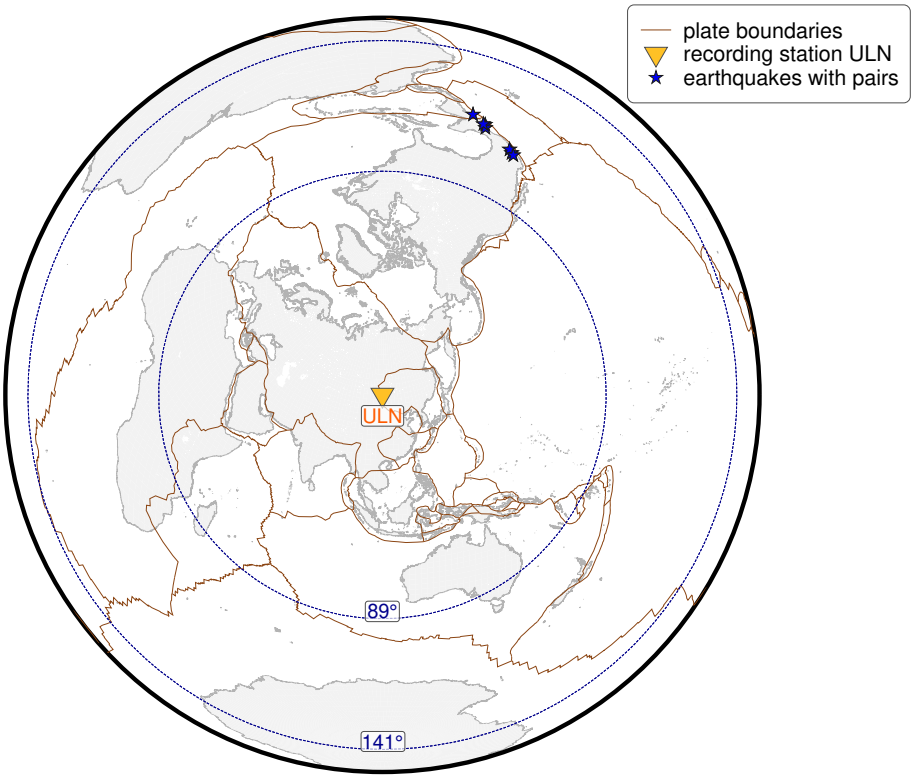

Figure 6.5: *Map of the epicentres of the earthquakes for which at least two XKS phases were measured. The yellow triangle shows the recording station ULN. The blue circles represent epicentral distances of* 89° *and* 141°*.*

For the earthquakes for which SWSMs are successful, the piercing points are displayed in Fig. 6.6. The piercing points of these events all plot to the east of the centre of the HLFL. In this configuration of earthquakes and recording station, the SKS phases plot closer to the centre than the SKKS phases. The observations of the SWSMs towards the easternmost piercing points show consistent split measurements for both phases. The discrepant pairs are also consistent, yet an additional split measurement is obtained within the null measurements in the SKKS phases. However, since this split observation corresponds to a same pair, the splitting process might originate from the upper mantle or crust.

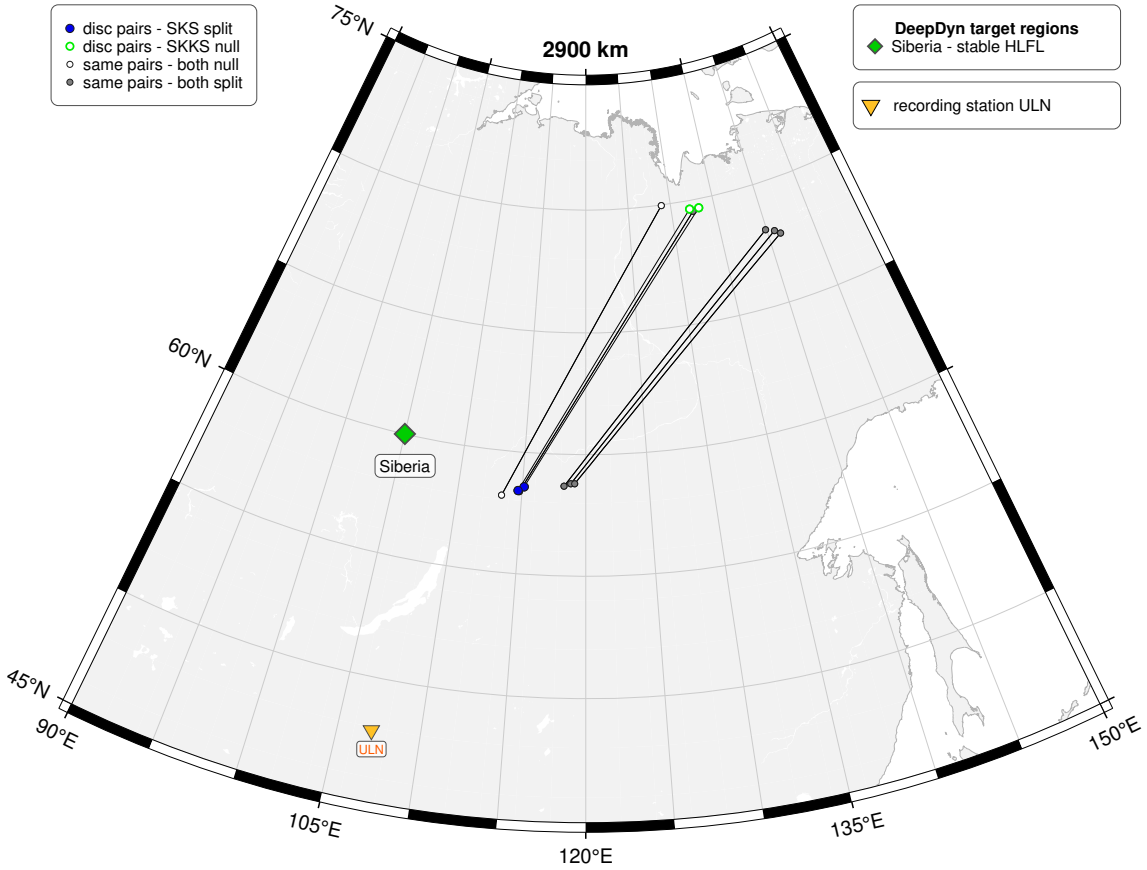

Figure 6.6: *Piercing points at the receiver side of the raypath at* 2900 km *depth for the station ULN. The yellow triangle marks the recording station ULN and the green diamond the DeepDyn target region beneath Siberia. The colour of the piercing point indicates the wave type and the type of splitting observation.*

6.1.3 WMQ station

At the WMQ station only three pairs are measured. All three pairs show splits for both phases (cf. Table 6.3). The values for the splitting parameters are in good agreement for the SKS phases (Fig. 6.7). However, one of the three SKKS measurements has a different orientation of the fast polarisation axis, but with a similar delay time as the others.

Table 6.3: *Number of pairs for which at least two of the analysed XKS phases were observed for an earthquake at the station WMQ. The second and third column present pairs for which both seismic phases show similar splitting observations, while for pairs in the fourth column, both phases show different splitting observations.*

total no. of pairs	no. of same pairs (nulls)	no. of same pairs (splits)	no. of discrepant pairs
3	0	3	0

From all the potential earthquakes shown in Fig. 5.4c only events with epicentres in Central America (cf. Fig. 6.8) can be used, since for larger epicentral distances phase interferences occur. A plot of the piercing points of the three pairs is presented in Fig. 6.9. The three events have almost identical piercing points, in particular the SKS phases. Looking at the spatial orientation of the raypaths through the target region it would have been

interesting to get information about the anisotropy in the LMM west of the HLFL with raypath passing through the region from a north-south direction. However, the consistent split measurements for both phases, with comparable values for the splitting parameters, preclude further implications on the anisotropy in the LMM.

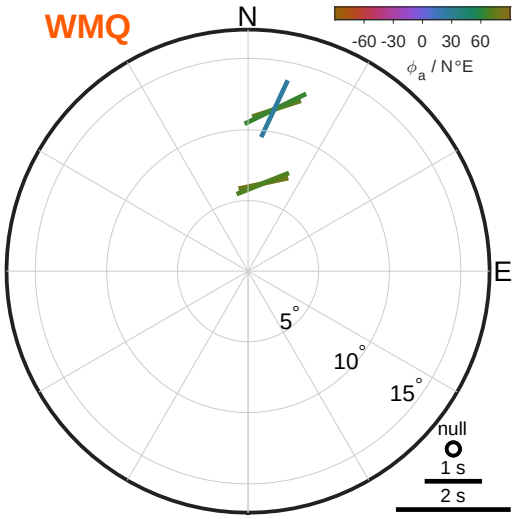

Figure 6.7: *Stereoplot of pairs of XKS measurements for the station WMQ with at least one of the measurements being of good or fair quality. The positions of the markers indicate the BAZ and the degrees from the centre point show the incident angle. The form of the marker depends on the observational type. For further explanation of the projection see Fig. 4.1.*

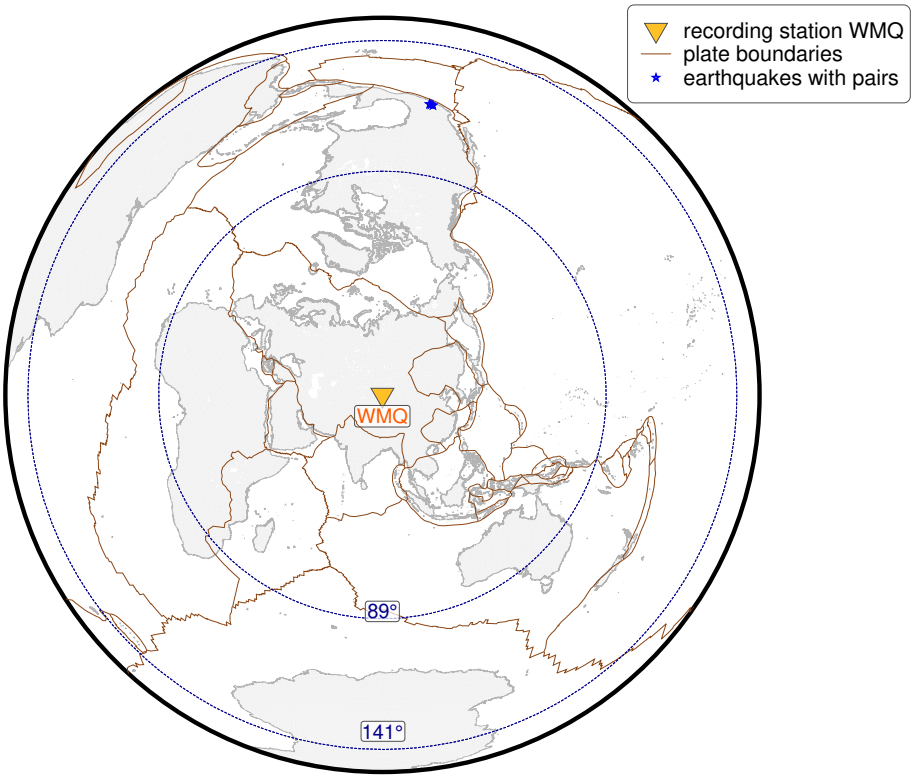

Figure 6.8: *Map of the epicentres of the earthquakes for which at least two XKS phases were measured. The yellow triangle shows the recording station WMQ. The blue circles represent epicentral distances of* 89° *and* 141°*.*

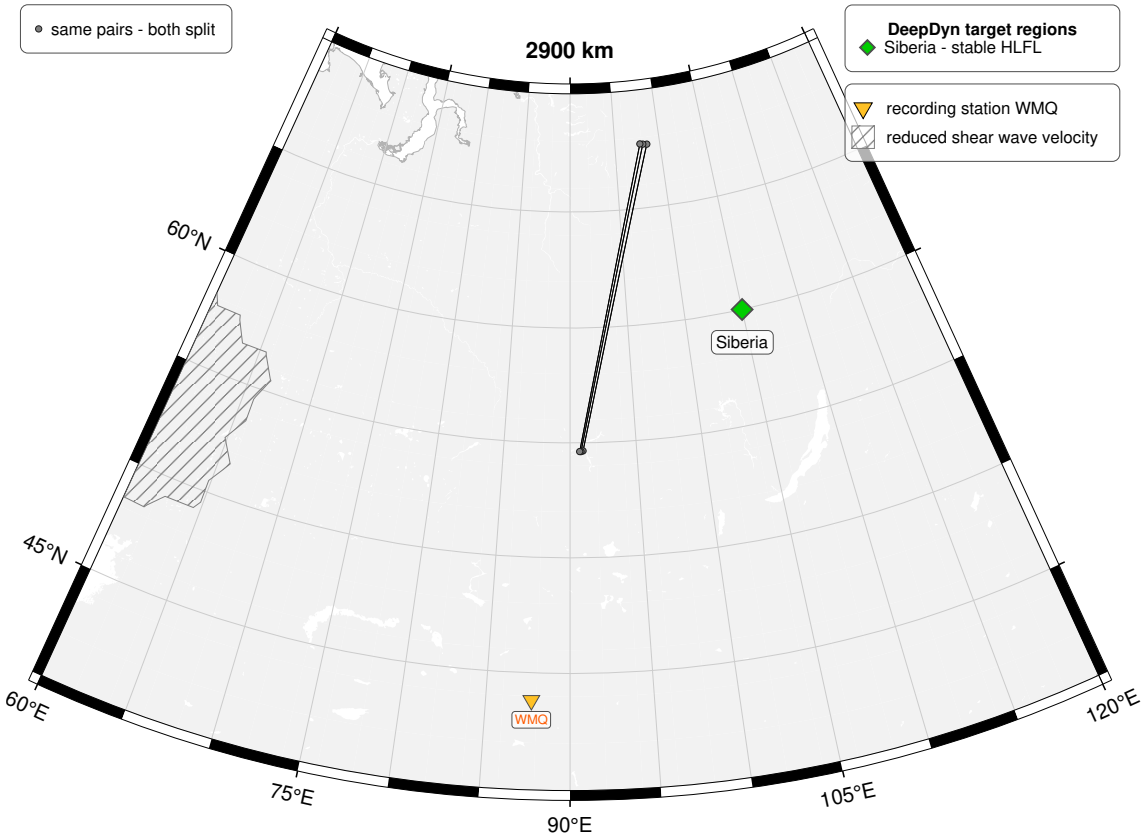

Figure 6.9: *Piercing points at the receiver side of the raypath at* 2900 km *depth for the station WMQ. The yellow triangle marks the recording station WMQ and the green diamond the DeepDyn target region beneath Siberia. The data of the region with reduced shear wave velocity is taken from Wolf et al. (2023). The colour of the piercing point indicates the wave type and the type of splitting observation.*

6.1.4 ScanArray stations

The primary objective of studying SWSMs at the three ScanArray stations (Thybo et al., 2021) SA01, SA02 and SA05 is to ascertain the reproducibility of measurements at stations that are geographically proximate. To this end, measurements have been conducted on these three temporal stations in the north of Norway. Only for two of the three stations SWS has been observed. For each of the stations SA01 and SA02, two discrepant pairs are observed (Table 6.4).

Table 6.4: *Number of pairs for which at least two of the analysed XKS phases were observed for an earthquake at the ScanArray stations SA01, SA02, SA05. The second and third column present pairs for which both seismic phases show similar splitting observations, while for pairs in the fourth column, both phases show different splitting observations.*

station	total no. of pairs	no. of same pairs (nulls)	no. of same pairs (splits)	no. of discrepant pairs
SA01	2	0	0	2
SA02	2	0	0	2
SA05	0	0	0	0

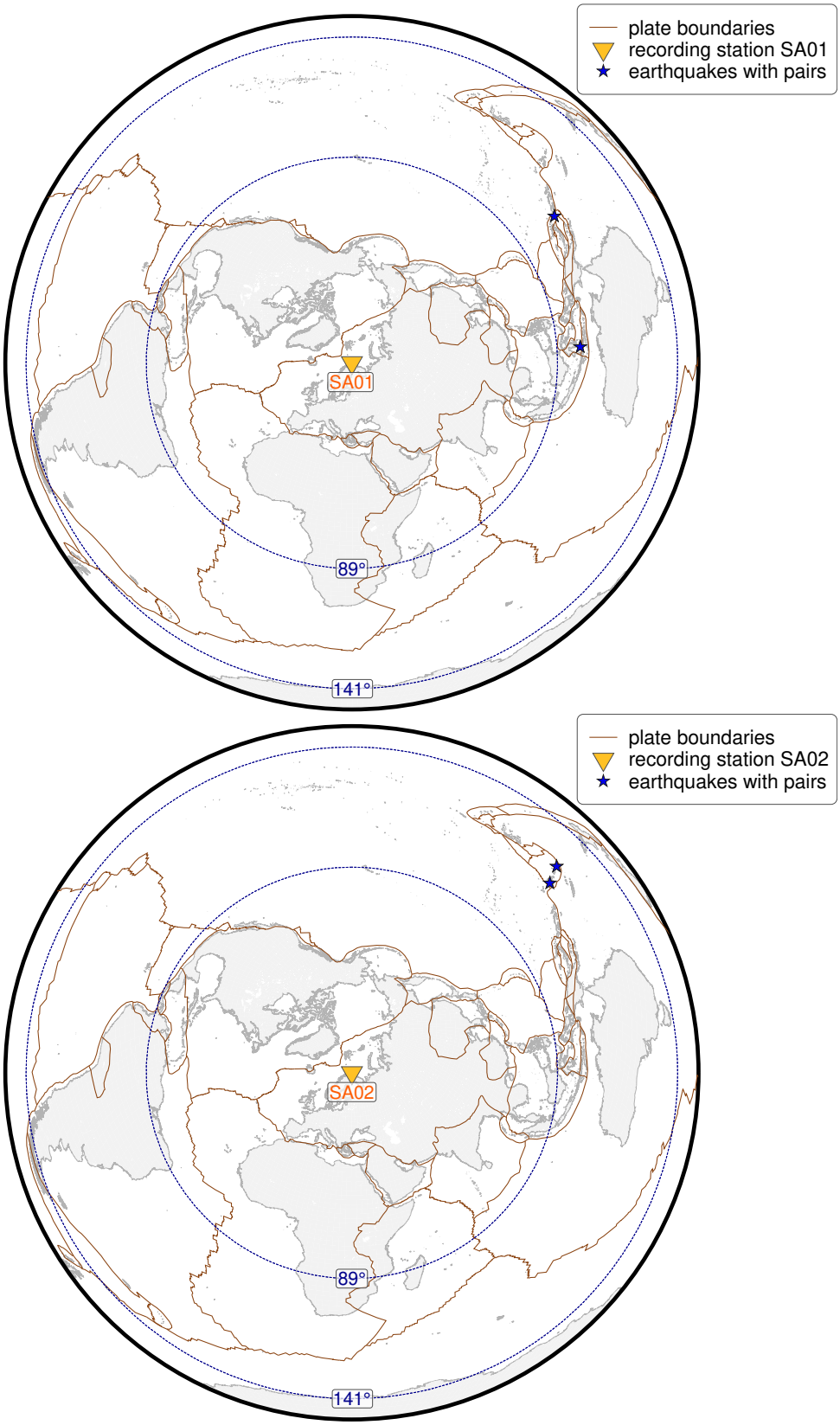

Figure 6.10: *Map of the epicentres of the earthquakes for which at least two XKS phases were measured for the station SA01 (top) and the station SA02 (bottom). The yellow triangles show the recording stations. The blue circles represent epicentral distances of* 89° *and* 141°.

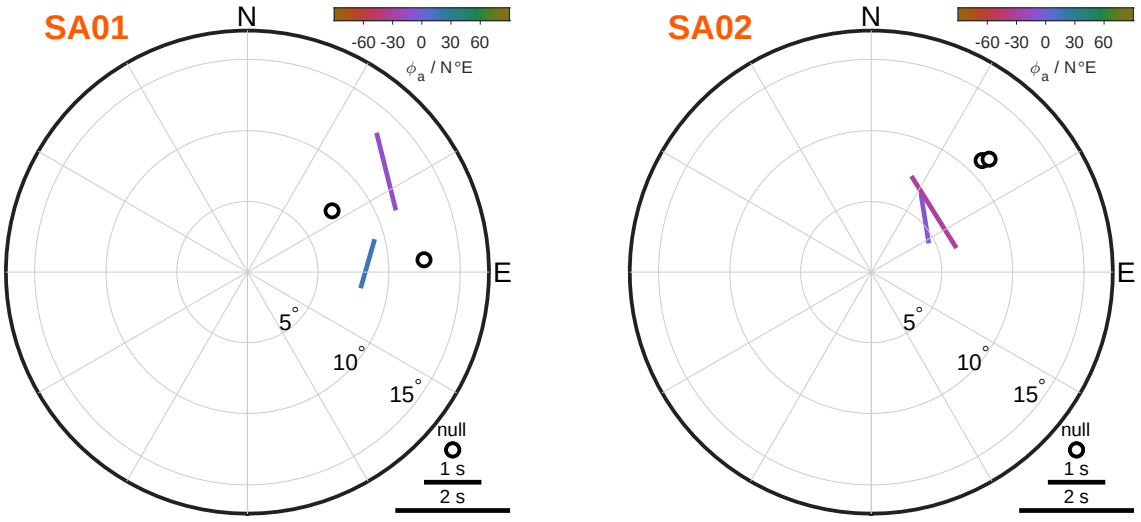

(a) SA01 *(b) SA02*

Figure 6.11: *Stereoplots of pairs of XKS measurements for the station SA01 (left) and the station SA02 (right) with at least one of the measurements being of good or fair quality. The positions of the markers indicate the BAZ and the degrees from the centre point show the incident angle. The form of the marker depends on the observational type. For further explanation of the projection see Fig. 4.1.*

The epicentres for those pairs are located in Southeast Asia towards Tonga (Fig. 6.10). Consequently, the rays pass through the anisotropic region in southeast to northwest direction up to east to west direction. The stereoplot of the two discrepant pairs for the SA01 station in Fig. 6.11 (left) shows slightly different BAZs between northeast and east, with the northernmost one showing a split measurement for SKKS and the easternmost showing a null measurement. The two pairs from the station SA02 have a BAZ of around 45° with the SKKS phases showing nulls while the SKS phases are split (Fig. 6.11 (right)). The piercing points in 2900 km depth of the four pairs are shown in Fig. 6.12. The two pairs with split SKS phases from the SA02 station are found to be in close spatial proximity, which strengthens the reliable performance of the method. The two pairs from the SA01 station are further south with different observational types for each phase. A noteable observation is that for three out of the four pairs the phase closer to the centre of the HLFL does not show splitting, while the one further away does. This is in contrast to the results we obtained from the measurements at the previously measured stations. Possible reasons for this, as well as a comparison regarding the SNRs and the individual pairs that are measured at these three stations, will be explained in the following sections.

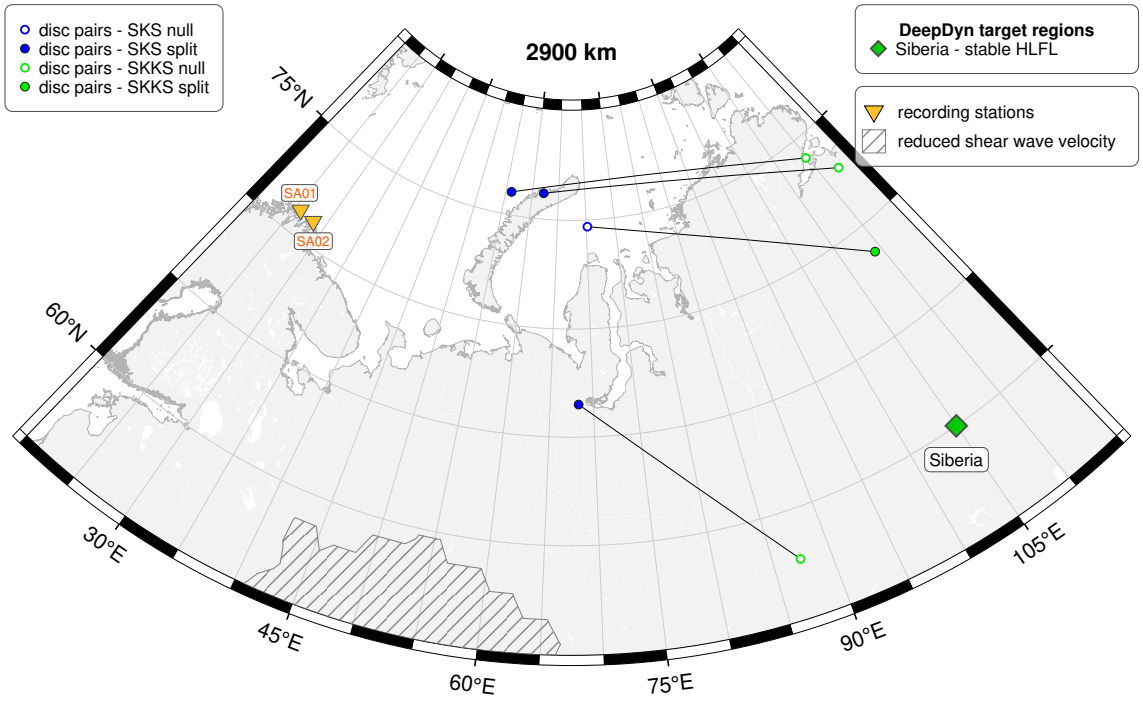

Figure 6.12: *Piercing points at the receiver side of the raypath at* 2900 km *depth for the stations SA01 and SA02. The yellow triangles mark the recording stations SA01 and SA02 and the green diamond the DeepDyn target region beneath Siberia. The data of the region with reduced shear wave velocity is taken from Wolf et al. (2023). The colour of the piercing point indicates the wave type and the type of splitting observation.*

6.2 Summarised results at studied stations

Performing SWSMs at six different stations resulted in the observation of pairs of *X*KS phases at five of these stations. In the following analysis, the SWSMs with BAZs from northeast to east of the KEF station are additionally included. The number of pairs in total, classified by the observational type, can be seen in Table 6.5. The first line contains the SWSMs performed at the KEF station for raypaths with BAZs from northeast and east. These are a total of 25 pairs, with eight discrepant pairs.

Table 6.5: *Number of pairs for which at least two of the analysed XKS phases were observed for an earthquake at the studied stations. The second and third column present pairs for which both seismic phases show similar splitting observations, while for pairs in the fourth column both phases show different splitting observations.*

station	total no. of pairs	no. of same pairs (nulls)	no. of same pairs (splits)	no. of discrepant pairs
KEF	25	7	10	8
HSPB	10	2	3	5
ULN	7	1	4	2
WMQ	3	0	3	0
SA01	2	0	0	2
SA02	2	0	0	2
SA05	0	0	0	0

Figure 6.13 displays the piercing points for pairs from all seven stations. The centre of the HLFL beneath Siberia is again marked with a green diamond. The colours of the dots represent the type of splitting observation and the phase, as well as whether the pair is a discrepant pair or a same pair. The combination of results demonstrates a varying orientation of pairs of XKS phases for which SWSMs are successfully performed. For the stations in Northern Scandinavia the SKKS phases plot closer to the HLFL than the SKS and PKS phases. In most cases, the SKKS phases show splitting while the SKS phases provide mostly nulls. For the stations in Central Asia, the ULN station exhibits a closer proximity of the SKS phase to the HLFL, with splitting observations for the discrepant pairs, while I have nulls for the SKKS phases of the discrepant pairs. For the WMQ station, both phases consistently show splitting with a comparable distance to the HLFL. A closer examination of the discrepant pairs, close to the HLFL, reveals a region, delineated by the yellow ellipse, in which the observations of the phases of discrepant pairs are consistently split (Fig. 6.13). In contrast, for discrepant pairs located farther from the HLFL, we observe mostly nulls, with certain regions of accumulations of nulls obtained from measurements at different stations (cf. brown ellipses in Fig. 6.13).

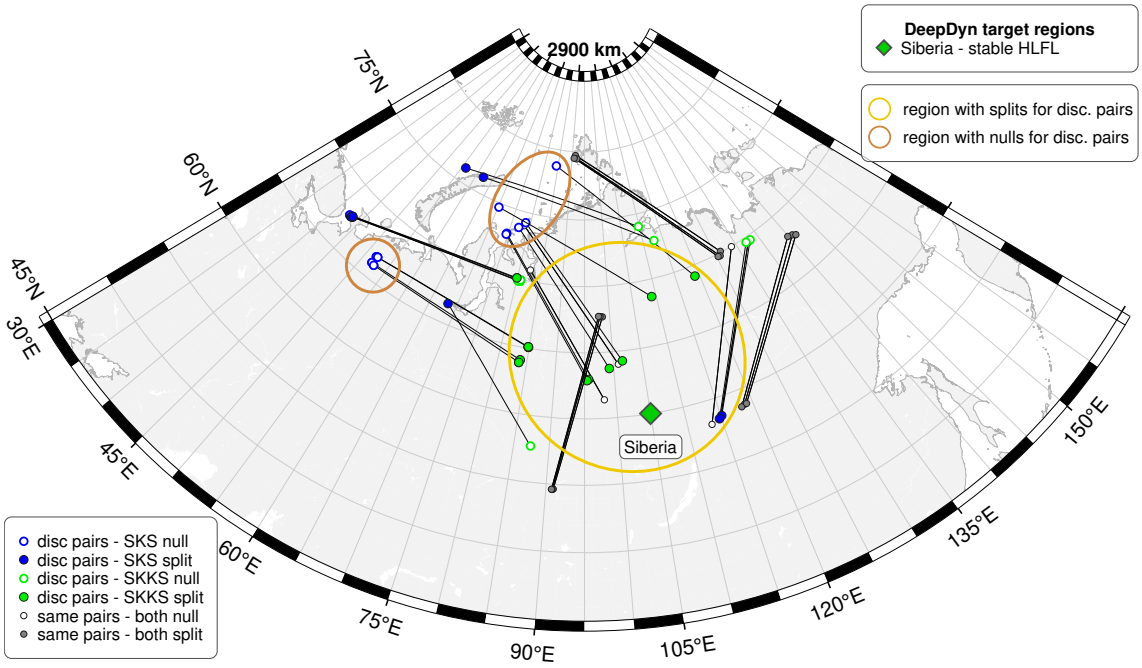

Figure 6.13: *Piercing points at the receiver side of the raypath at* 2900 km *depth for all stations. The green diamond marks the DeepDyn target region beneath Siberia. The colour of the piercing point indicates the wave type and the type of splitting observation. The yellow ellipse marks the region where phases of discrepant pairs show splitting, the brown ellipses regions where nulls are observed.*

Outside the marked regions, we also measured different observational types in close vicinity for both discrepant and same pairs. If a discrepant and same pair show different observational types, the anisotropy might originate from distinct sources, in the LMM or in the upper mantle or crust. Since SWS is a linear but not commutative property, the resulting observation at the surface is a combination of the anisotropies present at different locations along the raypath. Depending on the splitting parameters earlier along the raypath, splitting might occur or not occur later in the raypath depending on the geometrical orientation and the type of anisotropy being present in the crust (Long and Silver, 2009; Silver and Long, 2011).

Additionally, the propagation direction through the anisotropic medium plays a significant role in whether splitting is observed or not. In Section 2.2.3, the case of a simple anisotropy consisting of one layer of homogenous anisotropy is discussed. If the anisotropy is more complex, the type of splitting observation depends on the propagation direction through the medium, the initial polarisation of the incoming wave and the incidence angle (Wookey and Kendall, 2008; Nowacki et al., 2011).

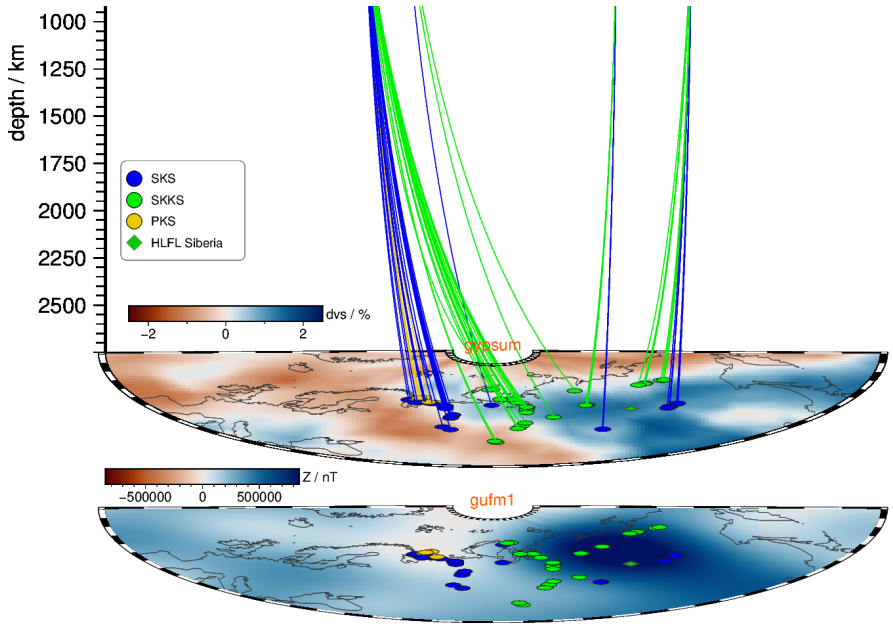

Figure 6.14: *3D representation of the raypaths of the events with pairs at all recording stations between* 2750 *km and* 1000 km *depth. The tomography according to the GyPSuM model (Simmons et al., 2010) is plotted in a depth of* 2750 km *depth with the corresponding piercing points of the rays plotted in the corresponding colours of each phase. The model gufm1 of the Earth's magnetic field (Jackson et al., 2000) at the CMB is plotted beneath with the piercing points for the rays in* 2900 km *depth.*

The combination of the measurements from all stations results in a complex pattern of connected piercing points, which offers the advantage of facilitating the study of the HLFL beneath Siberia along raypaths with different orientations and angles. This is further confirmed by looking at a 3D representation of the raypaths with piercing points in the LMM. Figure 6.14 displays the calculated raypaths with respect to their depth, according to the *tauP* package (Crotwell et al., 1999), for the three different seismic phases: SKS (blue), SKKS (green) and PKS (gold). The horizontal plane in 2900 km depth represents the *gufm1* model of the Earth's magnetic field (Jackson et al., 2000) and the horizontal plane at 2750 km depth shows the variations of shear wave velocity according to the *GyPSuM* model (Simmons et al., 2010). The dots give the piercing points of the different phases in the corresponding colours. The layer of the *GyPSuM* model is plotted in a depth of 2750 km, as the tomography model by Simmons et al. (2010) is obtained for depths between 2650 km to 2900 km depth. The various recording stations, together with earthquakes with epicentres in both South and Central America as well as Southeast Asia, provide us with varying locations of piercing points related to the HLFL and directions in which the waves propagate through the LMM. It is visible that both SKS and PKS phases penetrate through the LMM at steeper angles than the SKKS phases. Having both SKS and SKKS phases piercing through the D″ layer at proximal distances of the HLFL can give us additional information about the type of anisotropy by studying it at different angles.

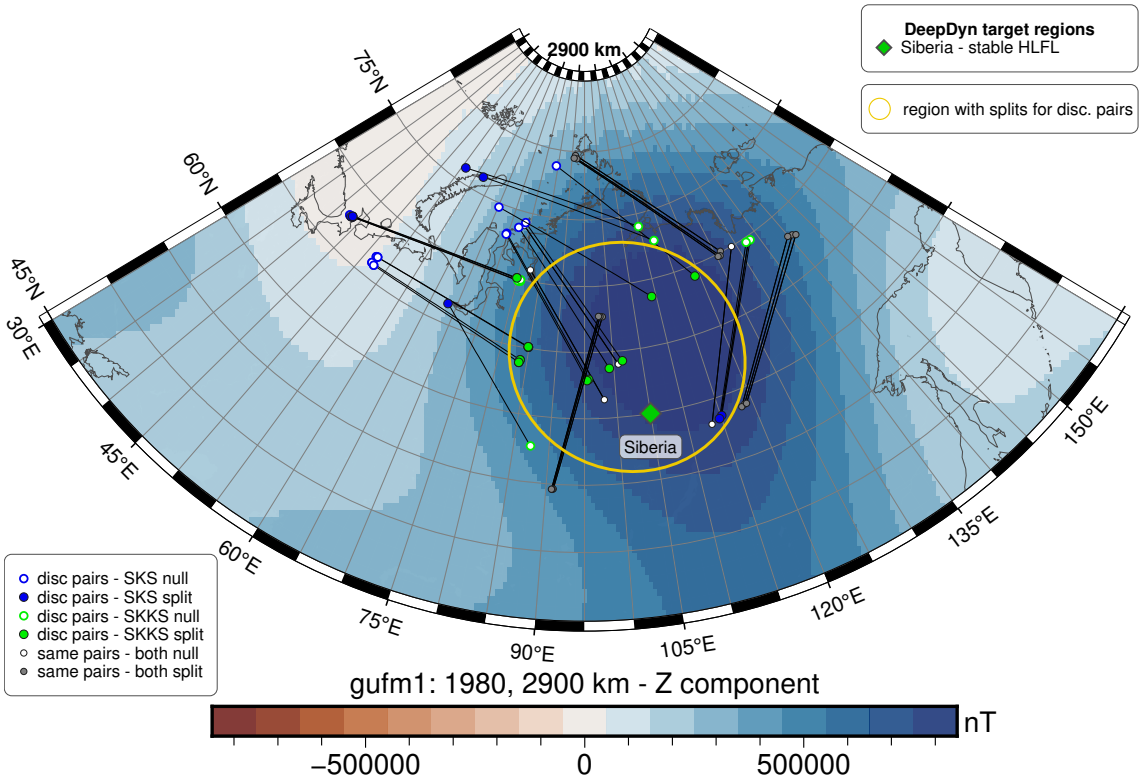

Figure 6.15: *Piercing points at the receiver side of the raypath at* 2900 km *depth for all stations. The green diamond marks the DeepDyn target region beneath Siberia. The colour of the piercing point indicates the wave type and the type of splitting observation. Plotted in the background is the gufm1 model of the radial component of the Earth's magnetic field at the CMB according to Jackson et al. (2000). The yellow ellipse marks the region where phases of discrepant pairs show splitting.*

A comparison of the measured splitting observations and the model of the Earth's magnetic field at the CMB can be seen in Fig. 6.15. The employed model is the *gufm1* model of Jackson et al. (2000). An increase in magnetic flux around and north of the marked position of the HLFL beneath Siberia is clearly visible. Therefore, the selected earthquake-station pairs define a reasonable selection with piercing points in the LMM in the region of interest. Marking again the yellow ellipse, that has already been shown in Fig. 6.13, in this figure and comparing the splitting observations with the intensity of the magnetic flux aligns nicely. The splitting observations of the discrepant pairs within the ellipse also lies within the region of the highest magnetic flux. In regions where observations are predominantly nulls, the magnetic flux is also lower, particularly towards the northwest and the west of the centre of the HLFL. Discrepant pairs from the KEF stations, located further from the centre of the HLFL towards the northwest, show a different pattern. For these measurements, both nulls and splits are observed for both phases. In some cases, the different results are obtained because pairs show the same splitting observation for both phases, thus implicating the presence of anisotropy in the upper mantle and crust. However, there are also discrepant pairs showing different observational types. These pairs have been measured at the KEF station before using the adjusted methods to analyse SWS, including the stricter constraints regarding both the selection of suitable earthquakes and the handling of near-null measurements (Wüstefeld and Bokelmann, 2007).

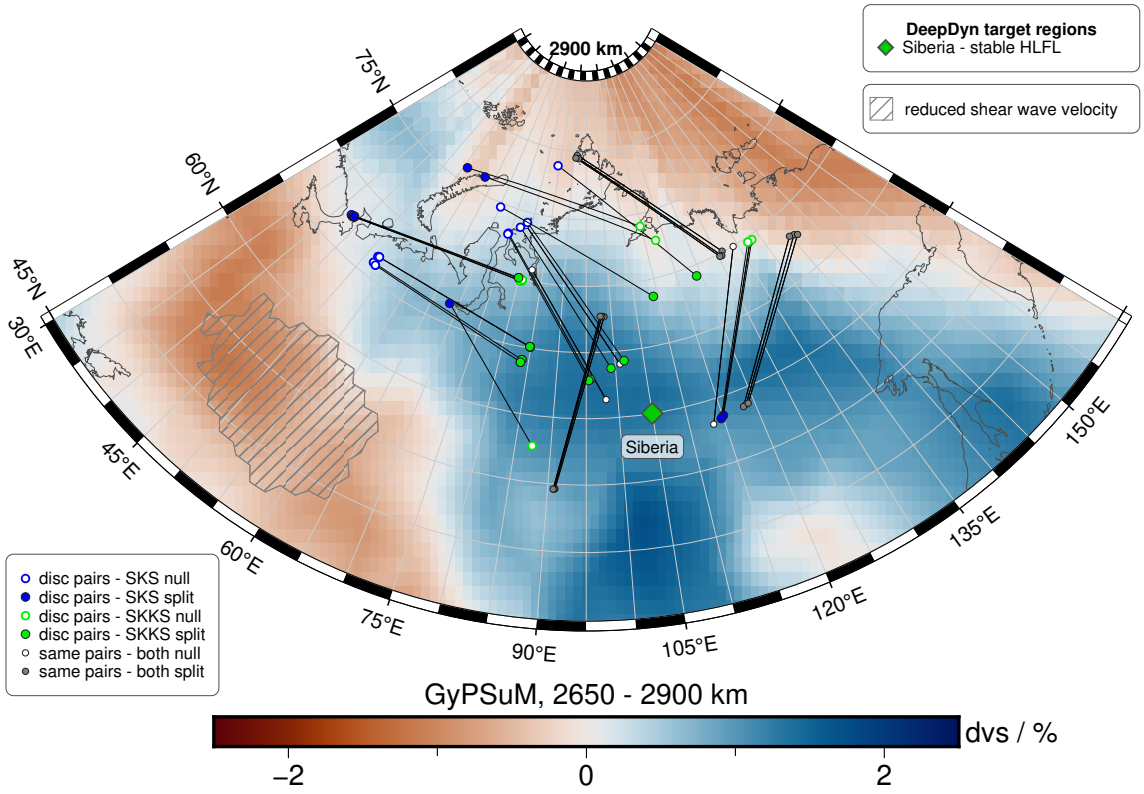

Figure 6.16: *Piercing points at the receiver side of the raypath at* 2900 km *depth for all stations. The green diamond marks the DeepDyn target region beneath Siberia. The colour of the piercing point indicates the wave type and the type of splitting observation. The data of the region with reduced shear wave velocity is taken from Wolf et al. (2023). The tomography GyPSuM model of the lateral variations of the shear wave velocity in* 2650 km *to* 2900 km *depth according to Simmons et al. (2010) is plotted in the background.*

In addition to the magnetic flux, variations of the shear wave velocity in the D″ layer need to be taken into consideration as a potential reason of the observed anisotropy. The *GyPSuM* model of Simmons et al. (2010) in the LMM, obtained from tomography, is plotted in the map of the piercing points at 2900 km depth in Fig. 6.16. The shear wave velocity in the region of the HLFL is increased, potentially associated with the remnant subduction slab as discussed in Section 2.1. Further away from the centre of the HLFL towards the north and southwest, a reduction of shear wave velocity is presented in the model. This goes along with the striped region representing the Perm anomaly (Wolf et al., 2023). In the majority of discrepant pairs, one of the piercing points is located within the region with increased shear wave velocity and for these phases splitting seems to occur. However, no clear trend is visible for the piercing points of discrepant pairs, that are located at the boundary of regions with increased or reduced shear wave velocity. This observation persists for piercing points that are in regions with decreased shear wave velocity. Towards the north, the majority of these phases of the discrepant pairs seem to produce null observations but there are also some exceptions towards the northwest. Those exceptions are primarily attributable to the measurements conducted at the KEF station, striking the importance of strict criteria in the classification and measurement of SWS. Additionally, uncertainties have not been incorporated into the figures for both the model of the Earth's magnetic field as well as the tomography. However, given the depth of the CMB, it is reasonable to conclude that these uncertainties are not negligible. Furthermore, the calculation of the exact piercing points and the raypath relies on the one-dimensional *iasp91* model (Kennett and Engdahl, 1991). Consequently, the interpretation of piercing

points in close proximity to the boundary of both the region of intense magnetic flux (Fig. 6.15) as well as the boundary between regions of increased and reduced shear wave velocity (Fig. 6.16) needs to be done with caution.

Comparing the map in Fig. 6.15 with other models of the Earth's magnetic field at the CMB or Fig. 6.16 with other models of the shear wave velocity in the same depth, e.g., the *REVEAL* model, obtained with full waveform inversion (Thrastarson et al., 2024), might provide insights to the uncertainties of the models, for both the magnetic field and the shear wave velocity, present at the position of the piercing points.

6.3 Comparison with other studies

The majority of the piercing points obtained in this thesis lie in a region where the *GyPSuM* model (Simmons et al., 2010) has an increased shear wave velocity (cf. Fig. 6.16). Anisotropy has been previously studied in the region of this increased shear wave velocity in the LMM in other studies. In this section, four of these studies are discussed in more detail (cf. Fig. 6.17). These are marked in yellow around the region where the raypaths of the studied events propagate through the LMM and labelled according to the authors and year of publication.

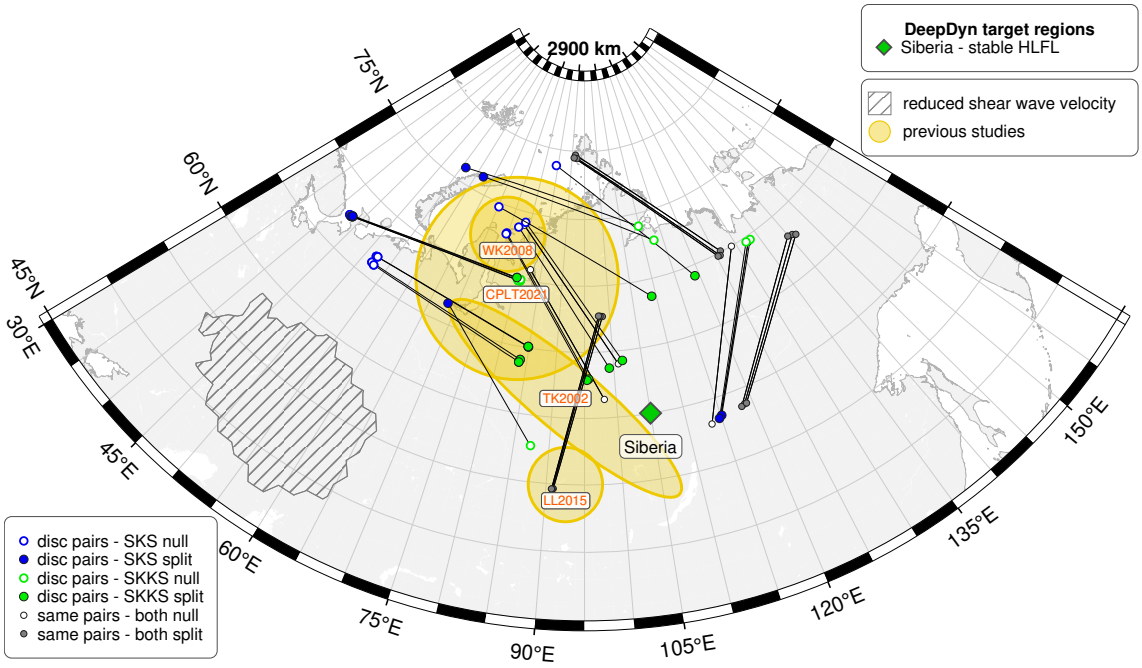

Figure 6.17: *Piercing points at the receiver side of the raypath at* 2900 km *depth for all stations. The green diamond marks the DeepDyn target region beneath Siberia. The colour of the piercing point indicates the wave type and the type of splitting observation. The data of the region with reduced shear wave velocity is taken from Wolf et al. (2023). The yellow coloured areas present regions where previous SWS studies have been performed: WK2008: Wookey and Kendall (2008), TK2002: Thomas and Kendall (2002), LL2015: Long and Lynner (2015), CPLT2001: Creasy et al. (2021).*

Thomas and Kendall (2002) measured eight earthquakes with epicentres in the northwest Pacific rim and hypocentral depths greater than 450 km at recording stations in Europe. SKS phases are used to correct for the influence of upper mantle anisotropy on the S and ScS phases. The splitting parameters are described by the time difference between the

signal of the S and ScS phases on the transverse and radial component of the seismograms. In 95 % of the split measurements, the transverse component of the wave is ahead of the radial component, while the shape of the signal corresponds to that of an isotropic model with a discontinuity of the D″ layer. Therefore, Thomas and Kendall (2002) proposed a transversely isotropic anisotropy. They associate the anisotropy with a subduction of the Izanagi plate, since a collision of the slab and the CMB proceeds in a significant shear deformation. This process has the potential to induce dislocation glide in crystal assemblages in the LMM or preferred orientations in inclusions (Thomas and Kendall, 2002).

Wookey and Kendall (2008) studied differential pairs of S and ScS phases at epicentral distances ranging from 60° to 85° along two perpendicular raypaths (east-west and south-north). They analysed one event from both directions at various recording stations. From these measurements, they obtained different delay times and values for the fast polarisation axis, from which they interfered an incomparability of a simple anisotropy. Their measurements agree with the north-south trend of geodynamics as determined by tomography. These measurements might go along with a LPO of perovskite or post-perovskite, or an alignment of melt inclusions. The observed anisotropy may therefore be a consequence of the remnant slab material from past subduction in the North Pacific (Wookey and Kendall, 2008).

A direct comparison between the results of this study and those of Thomas and Kendall (2002) and Wookey and Kendall (2008) is not straightforward. Both used discrepant pairs of S and ScS phases to study the anisotropy in the LMM. As the ScS phase gets reflected at the CMB, this phase propagates almost horizontally through the D″ layer. In contrast, *X*KS phases, which have been utilised throughout this thesis, and particularly SKS phases, have a steeper angle with which they penetrate through the D″ layer (Fig. 4.8). Wookey and Kendall (2008) obtained splits for discrepant pairs of S and ScS phases in the yellow circular region labelled with WK2008 in Fig. 6.17, where I obtained predominantly nulls. This difference can be explained by the different raypaths that *X*KS and ScS phases have in the LMM. The strength of the anisotropy and the path length within this anisotropy always show a trade-off regarding the values of the splitting parameters and eventually even the type of splitting observation (Nowacki et al., 2011; Creasy et al., 2021). Additionally, the splitting parameters by Wookey and Kendall (2008) are obtained along raypaths in south-north and east-west direction. In this thesis, the raypaths with piercing points in vicinity of the region studied by Wookey and Kendall (2007) are raypaths from southeast to northwest. In the presence of a complex anisotropy (more complex than a single, laterally homogeneous, horizontal anisotropic layer), different results can follow from different measurement methods, including the propagation direction, propagation angle or wave type (Long and Silver, 2009).

Creasy et al. (2021) studied a similar region as Wookey and Kendall (2008), but to a larger extend. Their SWSMs included in addition to SKS, SKKS and PKS phases also SKiKS phases. The SKS phases (corrected for upper mantle anisotropy) with piercing points in the centre of the region labelled with CPLT2021 in Fig. 6.17, predominantly do not show splitting. Towards the north of the study region of Creasy et al. (2021), consistent split PKS phases are measured. These findings are consistent with both the null observations in SKS phases in the centre of the region found in this work as well as the splits in SKS phases obtained north of the CPLT2021 region. Additionally, Creasy et al. (2021) performed forward modelling, combining their SWSMs with PdP and SdS reflection polarities. They associated the anisotropy with a CPO of post-perovskite or bridgmanite. Since the shear direction that they obtained is orientated south-southwest or north-northeast, they suggest a flow in the LMM towards the Perm anomaly (Creasy et al., 2021).

Long and Lynner (2015) conducted a study on anisotropy in the region labelled by LL2015 in Fig. 6.17. They observed a LMM anisotropy in proximity to the Perm anomaly. 30 discrepant pairs were measured at 18 stations within Europe. Of these, ten discrepant pairs sample the boundary of the Perm anomaly, while a smaller group sample the region east of the Perm anomaly around (60° N, 80° E). These discrepant pairs are associated with the pronounced lateral gradient in shear wave velocity in the region and the presence of mantle flow. The presence of anisotropy near the boundary of the Perm anomaly indicates that deformation is concentrated at the boundary, potentially linked to mantle flow directed towards the Perm anomaly (Long and Lynner, 2015).

Since anisotropy of the LMM has been previously observed in the target region of this thesis, and the SWS observational types in this thesis agree particularly well with the observations types of the same phases in the region of CPLT2021, we interpret the measurements performed in this thesis as indeed showing lateral variations in seismic anisotropy in the D″ layer. The anisotropy in the LMM beneath Siberia has been associated with a deformation of slab material, which may result in a potential alignment of material (Thomas and Kendall, 2002; Wookey and Kendall, 2008). The material exhibiting anisotropy could also influence the magnetic flux due to alignment, potential changes in temperature or chemical composition.

However, a number of assumptions needs to be made in order to get from measurements of anisotropy to mantle flow and, consequently, deformation. These assumptions include constraints regarding the type of anisotropy, rheology, the response of the material to shear and the strain history. Many of these influencing factors are still unknown, including, e.g., lateral variations in viscosity and temperature, as well as the effect of composition and temperature on the density of mantle phases (Nowacki et al., 2011; Creasy et al., 2021). Nevertheless, previous studies have shown that the LMM influences the magnetic field through the control of the geodynamo. Especially, the presence of static features as the HLFLs result from the coupling of flow in the core to the mantle (Bloxham and Gubbins, 1987). The morphology of the geomagnetic field is, thus, strongly influenced by the structure in the D″ layer in regions of fast shear wave velocity anomalies (Gubbins et al., 2007). The flow in the highly electrically conductive core, generating a major part of the Earth's magnetic field, is electromagnetically coupled to the lower mantle, which is significantly less conductive. An electromotive force in the LMM is induced, due to the advection of fluid motions in the core, resulting in movements of the magnetic field lines. This effect may vary laterally due to the temperature-dependent conductivity of the mantle (Bloxham and Gubbins, 1987). Gubbins et al. (2007) suggest that the influence due to thermal variations might have stronger effects on the magnetic field than compositional variations, with the thermal conductivities of the minerals at the CMB forming an important boundary condition for core dynamics. The large lateral temperature variations above the CMB act back on the core and force weak convection in the core. This might force an alignment of convection cells in the core with thermal anomalies in the LMM (Bloxham and Gubbins, 1987). Li (2020) suggests the formation of hot thermal ridges due to small-scale convection near the CMB which is driven by subducting slabs - driving flow towards a hot anomaly (as the Perm anomaly). These thermal ridges may cause or enhance seismic anisotropy in the region (Li, 2020).

6.4 Evaluation of the used method

In the following, the obtained results are discussed regarding the SWS method. Section 6.4.1 addresses the discrepancy between the small percentage of measured SWS pairs compared to the number of the requested events for the different stations. In addition, the dependence

of the observation of SWS with varying BAZs is discussed. Section 6.4.2 presents the criteria to minimise the dependence of the results on the analyst. In the last section (6.4.3), the reproducibility of the results at proximate stations is discussed.

6.4.1 Number of observed splitting pairs

Looking at Table 6.1 to Table 6.4 for all analysed stations, a great discrepancy can be seen between the number of requested events and the number of events for which a successful SWSM of a pair of *X*KS phases has been performed. Only in around 2.7 % to 4.7 % of the earthquakes, a pair of core refracted waves with SWS has been observed at one of the studied permanent stations. Various factors that can lead to this discrepancy are mentioned in Table 6.6 for the permanent stations HSPB, ULN and WMQ and in Table 6.7 for the temporary stations SA01, SA02 and SA05. The first criterion refers to the correct set-up of the seismic station or a possible misorientation of the seismic station, which goes along with an incorrect orientation of the three components, ZNE, of the seismometer. This specific problem occurred again at the WMQ station, affecting 33 out of the 111 earthquakes (cf. Fig. A.4 and Fig. A.5). Since no information regarding the exact misorientation of the seismometer is mentioned in the metadata of the station, a correction for this misorientation could not be done for the WMQ station. Consequently, these events are not used, in contrast to the data from the KEF station which have been corrected prior to the analysis.

Table 6.6: *Analysis of requested EQs regarding their eligibility for SWSMs of XKS phases for the permanent stations HSPB, ULN and WMQ.*

criteria	**HSPB** no. EQ=211	**ULN** no. EQ=167	**WMQ** no. EQ=111
misorientation	-	-	33
phase interferences			
$\leq 90°$: ScS, S & SKS	-	-	-
$[104, 109]°$: SKKS & SKIKS	50	6	-
$> 129°$: SKS & SKIKS	-	41	4
$> 135°$: SKS & SKIKS and pSKS & SKKS	-	26	-
magnitudes			
$M_W < 6.0$	100	94	71
$M_W \geq 7.5$	4	4	1
remaining EQ	**82**	**44**	**22**

Additionally, phase interferences, a major factor influencing SWSMs, have been previously discussed in Section 4.3.2. To exclude interferences with S and ScS phases for both SKS and SKKS phases, only events with epicentral distances greater than 89° are analysed. But, a closer look at Fig. 4.7c reveals that SKKS and SKIKS phases arrive in close temporal proximity in an epicentral range of $[104, 109]°$. This significantly influences the number of usable events for the HSPB station with 50 out of 211 events being in this epicentral distance.

For the ULN station, the large epicentral distances to the selected earthquakes enable the measurement of SWS for PKS phases. However, the interference of SKIKS and pSKS phases for both SKS and SKKS phases limits the SWSMs in 41 of 167 earthquakes. Another main influence on measuring SWS is the magnitude of the analysed earthquakes. For earthquakes with moment magnitudes smaller than 6, the low SNR hinders the measurement of SWS since the relevant phases cannot be clearly identified or might be hidden in noise. More than 60 % of the earthquakes at the WMQ station and still 47 % of the events at the HSPB station have moment magnitudes between $[5.6, 5.9]$. Increasing the moment magnitude limit will increase the SNR, but it will also strongly reduce the number of potential earthquakes. A limit for very large moment magnitudes ($M_W \geq 7.5$) is pointed out due to the long rupture duration, and therefore the signal of the SKS and SKKS phases may be hidden in the S wave coda. This affects only few events due to the rare occurrence of strong earthquakes. The influence of a limit on the hypocentral depth is not further discussed here, since a boundary of 50 km already results in SWSMs with high SNR and strongly constrains the number of events.

Table 6.7: *Analysis of requested EQs regarding their eligibility for SWSMs of XKS phases for the temporary stations SA01, SA02 and SA05.*

criteria	**SA01** no. EQ=34	**SA02** no. EQ=40	**SA05** no. EQ=20
misorientation	-	-	-
phase interferences			
$\leq 90°$: ScS, S & SKS	-	-	-
$[104, 109]°$: SKKS & SKIKS	8	10	6
$> 129°$: SKS & SKIKS	-	-	-
$> 135°$: SKS & SKIKS and pSKS & SKKS	-	-	-
magnitudes			
$M_W < 6.0$	20	22	10
$M_W \geq 7.5$	1	1	1
remaining EQ	**10**	**14**	**7**

However, even for the remaining earthquakes (Table 6.6 and Table 6.7), not for every event SWSMs of pairs of *X*KS phases are measured. Another influencing factor on whether SWS can be measured at the station for an earthquake includes the radiation pattern. Therefore, an additional analysis is performed to study the directional dependency of the pairs, for which SWSMs are (not) performed successfully. The total ranges of BAZs for all downloaded earthquakes of the permanent stations are analysed and listed in Table A.8. The range given for the ULN station extends over north from 347.4° to 360° and then continues from 0.0° to 28.8°. The BAZ range for the WMQ station is similarly orientated. The total range of BAZs for the HSPB station is the widest with almost 53°. Within this range, two sectors can be identified where successful measuring of SWS can be performed. For the ULN station three ranges are defined. The limits of these ranges cannot be defined so clearly; especially between the range in the northern and north-eastnorthern range. However, the occurrence of PKS phases only in the BAZ range in the north is striking for defining a second sector where pairs can be measured. Despite the BAZ range of the WMQ station exceeding 31°, the three only pairs have been observed in a range between 9.2° to 10.0°.

Given the inhomogeneous distribution of suitable earthquakes for SWSMs of *X*KS phases on the Earth, and the constraints introduced due to the desired location of the piercing points in the LMM, making assumptions about directional dependency of the epicentres that are suitable for measuring SWS is not possible without including events from a larger backazimuthal range. The second cluster of pairs at the ULN station between $[357, 6]^\circ$, as an example, is the only cluster showing a significant number of measurable PKS phases. This is due to the fact that only in this BAZs there are sufficient strong and deep enough earthquakes in a matching epicentral distance. With the limited number of earthquakes and small ranges of BAZs a clear indication of the directional dependency of earthquakes with good measurable SWS is challenging, since this effect cannot be studied without the influence of other constraints on the events, such as the hypocentral depth or the magnitude. The listed values in Table A.8 for the hypocentral depth (z) and the moment magnitude (M_W) mark the smallest value for both, when a SWSM has still been performed. These values do not necessarily follow from the same earthquakes. From the measurements it is striking that, to be able to measure SWS, either a great hypocentral depth or a strong magnitude is needed. The presence of one of these criteria might compensate a lower value in the other, thereby still allowing for the occurrence of measurable SWS. This can be illustrated by an earthquake with a moment magnitude of $M_W = 6.0$ and a hypocentral depth of only 50 km, which can still result in a measurable SWS, and vice versa. Therefore, to minimise the discrepancy between the number of requested events and the measurable SWS, it is necessary to introduce a combined limit for the hypocentral depth and the moment magnitude of potential earthquakes. This could increase the percentage of SWSMs within the requested events, while at the same time not unnecessarily minimising the overall number of events, and thus discarding potential good earthquakes.

6.4.2 Reproducibility of the method depending on analyst

The influence of different analysts on the obtained SWSMs has been discussed in detail in Section 4.3. The definition of strict criteria for the classification of the observational type and the quality (Table 4.6) ensures an as objective classification as possible. Further restrictions on the potential earthquakes, with respect to hypocentral depth, moment magnitude and epicentral distances, serve to minimise the variations that occurred in the analyses of the events at the KEF station by different analysts. The implementation of these strict criteria might lead to discarding of some of the potential usable earthquakes and, consequently, measurable phases. Nevertheless, together with the use of two methods in *SplitLab* (Wüstefeld et al., 2008) to obtain the splitting parameters, this ensures that questionable results, for which different analysts might have different results, will not be included in the analysis. Since the overall number of discrepant pairs (19 out of 1486 analysed events) in the vicinity of the HLFL beneath Siberia is small, it is critical to ensure the quality and reproducibility of each measurement, independent of the analyst.

6.4.3 Reproducibility of the method at stations

The criteria defined in Table 4.6 and discussed in Section 4.3.2 and Section 6.4.2 are chosen to ensure that the results derived from SWSMs do not depend on the analysts. The same would be expected for measuring at different seismic stations in close spatial vicinity. For those stations, the radiation pattern of the earthquakes and the epicentral distance to the event should be the similar. If the stations are located in sufficient proximity to each other, the anisotropy in the upper mantle or crust just beneath the station should be similar. To quantitatively study this effect, SWSMs are performed at three stations of the ScanArray (SA01, SA02 and SA05) (Thybo et al., 2021). Since these stations have only been deployed temporarily, SWSMs can only be performed for a limited number of

earthquakes. The Julian dates for the earthquakes, for which at least one *X*KS phase is measured, are listed in Table 6.8. The different observations for the phases at the three stations are listed in three columns. If a SWSM can be performed for an given earthquake, the measured phase is listed, e.g., for the earthquake at the 2014.001 SWSMs at the SA01 station can be performed for the SKS phase, but not for the SKKS phase. The signal for the SKKS phase is not visible, likely due to noise or the absence of a visible signal within a reasonable time span around the theoretical arrival time of the phase. This is particularly the case for SKKS phases, for both the SA01 and the SA02 station. As previously observed and discussed, successful measurement of SWS of the SKKS phases is more challenging and cannot be accomplished as often as for the SKS phases (cf. Section 4.2). This can be attributed to the smaller amplitude of the SKKS phase, which is more susceptible to be hidden in the noise. The three stations in general show a comparable high noise level compared to the previously studied permanent station. A look at the locations of the three stations reveals their proximity to the shoreline in Northern Norway, which induces a higher noise level due to swell and tidal movements.

Table 6.8: *Comparison of SWSMs at different stations of the ScanArray.*

event date	**SA01**	**SA02**	**SA05**
2014.001	SKS; SKKS no signal	SKS no signal; SKKS & pSKS interfere	SKS not measurable
2014.049	no data	SKS; SKKS & SKIKS interfere	SKS not measurable
2014.101	SKS; SKKS	SKS no signal; SKKS & SKIKS interfere	no data
2014.121	no data	SKS; SKKS	signal btw. SKS & SKIKS
2015.058	SKS; SKKS	SKS; SKKS no signal	splitting methods disagree
2015.087	SKS; SKKS no signal	SKS; SKKS no signal	splitting methods disagree
2015.293	SKS; SKKS no signal	SKS; SKKS	no data

Only for two events (2014.101 and 2015.058) a pair of SWS is measured at the SA01 station. For both earthquakes, issues were encountered at the SA02 station regarding the absence of a visible signal for one of the phases or the interference of phases. The SA05 station exhibits an overall higher noise level than SA01 and SA02. Therefore, even if a signal is visible for one of the phases, SWS cannot be measured because both splitting methods (RC and SC) do not agree, or the particle motion is neither elliptical nor linear before and after correction.

The number of earthquakes, that can be studied at these stations, is further limited since not all three stations have been operating throughout the entire time span. If one of the stations is not operating for an earthquake this is indicated with "no data" in Table 6.8. This is, for instance, the case for the SA01 station for the earthquake at the 2014.121, for which a discrepant pair is measured at the SA02 station. A comprehensive comparison of the results at the ScanArray stations, concerning the reproducibility at the different stations, has therefore not been feasible due to a limited number of suitable earthquakes within the operational period of all three stations and a high noise level. To study this effect in more detail, these measurements should be repeated at two permanent stations

with a larger number of potential earthquakes and a lower noise level.

Indeed, the consistency of splitting observations for different earthquakes with spatially close epicentres and piercing points in the LMM for both SKS and SKKS phases has been studied in this thesis. For example, this can be seen in Fig. 6.9. The three earthquakes, for which splitting is observed for two core refracted phases, have epicentres in close vicinity, resulting in recorder-side piercing points that are spatially very close for both SKS and SKKS phases. The observational type is the same for all three events, thereby demonstrating consistency and therefore also reliability of the results. Similar observations can be obtained for the three easternmost pairs measured at the ULN station (Fig. 6.6). Both the SKS and SKKS phases show consistent results for the observational type, with especially the piercing points of the SKS phases in the LMM being in close vicinity.

Chapter 7

Conclusion and outlook

In this thesis, SWSMs have been conducted to study seismic anisotropy in the LMM beneath Siberia, using XKS phases. Earthquakes with moment magnitudes greater or equal to 5.5 and a hypocentral depth of at least 20 km with epicentral distances ranging from 80° to 141° degrees have been measured at seven seismic stations. The recording stations are broadband stations in Northern Europe and Central Asia. The splitting parameters, the orientation of the fast polarisation direction ϕ and the delay time δt, are determined in *MATLAB* using the *SplitLab* software (Wüstefeld et al., 2008). The SWS for the single event analysis is performed using the RC method (Bowman and Ando, 1987) and the SC method (Silver and Chan, 1991). A particular focus is placed on the analysis of phase pair SWS discrepancies, i.e., between SKS and SKKS phases, as they serve as a clear indication for a LMM contribution to the splitting signal.

Measurements of SWS at the KEF station in Finland resulted in a total of 36 pairs with 17 discrepant pairs with piercing points in the LMM beneath the North Atlantic as well as southeast to northeast of the recording station. The piercing points of the SKKS phases west of the KEF station align with the boundary of the LLSVP beneath the North Atlantic. These SKKS phases close to the boundary of the LLSVP consistently show splitting while the SKS phases further away from the region of reduced shear wave velocity show nulls. The splitting observations of the SKKS phases suggest a strong anisotropy along the boundary of the LLSVP. This is assumed to be induced by a complex mantle flow towards the region of reduced shear wave velocity and this potentially feeds into an upwelling of hot mantle material (Grund and Ritter, 2018; Long and Lynner, 2015). The SWSMs with piercing points east of the KEF station result in a complex pattern with varying nulls and splits for all three phases. This complexity can be attributed to the combination of an increased shear wave velocity in proximity to the subducted slabs beneath Siberia and a reduced shear wave velocity within the vicinity of the Perm anomaly.

The analysis of SWS at the KEF station provided the additional advantage to be able to compare the results obtained by different analysts. Muhammad Dillah and I studied the same dataset which had previously been analysed by Grund and Ritter (2018). Variations between the analysts can be attributed to an error in the temporal alignment of the components of the seismograms in *SplitLab* (Fröhlich et al., 2023), still contained in the measurements of Grund and Ritter (2018), resulting in the creation of artificial splitting observations or distortion of some measured splitting observations. Other factors influencing the quality of measurements and the splitting observational type include both subjective as well as objective factors. As objective factors, the time window in which splitting measurements are performed and the filter parameters are criteria that are selected individually by the analyst. Additionally, simultaneously arriving seismic phases might

influence the SWSMs due to phase interferences. Aside from that, subjective factors such as possible near-null measurements (Wüstefeld and Bokelmann, 2007) as well as the human factor have a non-negligible influence on the SWSMs.

The information obtained from the measurements at the station KEF has then been incorporated into the measurements of anisotropy at the HLFL beneath Siberia. The selection of six different seismic stations and the corresponding earthquakes has been made in such way, that the piercing points through the LMM are within a 15° radius around the centre of the HLFL beneath Siberia. Thereby, enabling a comprehensive image of the anisotropy in the LMM in this region along various propagation directions. The study of pairs of core refracted phases gives the advantage to be able to attribute the anisotropy to the LMM while also examining the anisotropy in the regions at different angles, since SKS phases are penetrating through the LMM at steeper angles as SKKS phases. A total of 49 pairs are measured with 19 discrepant pairs, indicating that the observed anisotropy can be attributed to the LMM. The observed pattern in the discrepant pairs predominantly finds split phases within the region where the model of the Earth's magnetic field at the CMB (Jackson et al., 2000) indicates the highest magnetic flux. Therefore, the SWSMs might be associated with an increased magnetic flux manifesting as potential changes of mineral composition or temperature variations, and thus a deformation process that leads to an alignment of material, which results in the macroscopic observation of anisotropy in the region (Gubbins et al., 2007; Nowacki et al., 2011).

A comparison with previous studies shows a robust evidence for seismic anisotropy in the LMM in the target region (Thomas and Kendall, 2002; Wookey and Kendall, 2008; Creasy et al., 2021; Long and Lynner, 2015; Grund and Ritter, 2018). A high level of agreement is obtained between the results in this thesis and by Creasy et al. (2021) using core refracted phases. However, discrepancies emerge when comparing the results with the SWSMs by Thomas and Kendall (2002) and Wookey and Kendall (2008), who used pairs of S and ScS phases. In the presence of a complex anisotropy, the measured splitting type depends on the propagation direction as well as the angle with which the wave propagates through the LMM. Since ScS phases are reflected at the CMB, they penetrate through the D″ layer at much smaller angles than *X*KS phases. So far, the present anisotropy has mostly been associated with a change in shear wave velocity due to the remnant subducted slab and thus deformation processes that go along with this downwelling material (Thomas and Kendall, 2002; Wookey and Kendall, 2008; Creasy et al., 2021). A comparison of the splitting pattern with the model of the Earth's magnetic field (Jackson et al., 2000) offers an alternative possibility. The flow processes at boundaries with increased and decreased shear wave velocity may be associated with temperature and density variations, which could impact mineral and phase composition in these regions (Li, 2020). Consequently, these deformation processes could also influence the intensity of the magnetic flux in the region.

In order to understand how variations of shear wave velocity or changes in the intensity of the magnetic flux influence the presence of anisotropy or whether a combination of both might contribute to the measured splitting observation further SWSMs are required. By studying additional stations, that show a significant number of suitable, deep and strong enough earthquakes (cf. Table A.1), a more complete image of the pattern of anisotropy might be obtained. The incorporation of discrepant pairs of S and ScS phases might reduce and explain the occurring discrepancies between the observations of SWS in this thesis and the studies by Thomas and Kendall (2002) and Wookey and Kendall (2008). As a way to obtain a more complete image of the anisotropy in the regions with intense magnetic flux, it is highly relevant to also compare the results obtained in the region of Siberia with those of the SWSMs at the HLFLs beneath Canada and the North Atlantic.

The DeepDyn Project "Understanding the influence of seismic deep mantle structure at the core-mantle boundary on intense magnetic flux regions" studies in addition to anisotropy also reflections of the D″ layer. This is carried out at the University of Münster. Their results should be compared to our measurements of SWS to obtain a more complete image on the seismic structures in regions of increased magnetic flux at the CMB.

In subsequent works, the link between the measuring of SWS and the underlying mantle flow geometries should be studied in more detail. This might provide information about a potential correlation of anisotropy and an increased magnetic flux. As many assumptions have to be made to infer the underlying deformation processes from the observation of SWSMs and potentially obtain a connection to the increased magnetic flux, forward modelling, e.g. using *AxiSEM3D*, should be utilised to obtain information regarding constraints on the mineral composition and temperature or pressure conditions in the vicinity of the HLFL beneath Siberia. The combination of the D″ reflections with a study of seismic anisotropy in the DeepDyn project has the potential to yield additional information that can constrain the geometry of possible models. This could overcome the general non-uniqueness problem of datasets and the imprecision of the responsible mechanism for the anisotropy in the LMM (Creasy et al., 2021). The SWSMs from this thesis can then be incorporated into the modelling as limiting conditions to test how well certain mineral compositions or temperature and pressure conditions fit with the obtained splitting observations.

Appendix A

A.1 SWSMs at KEF station

A.1.1 Misorientation of the KEF station

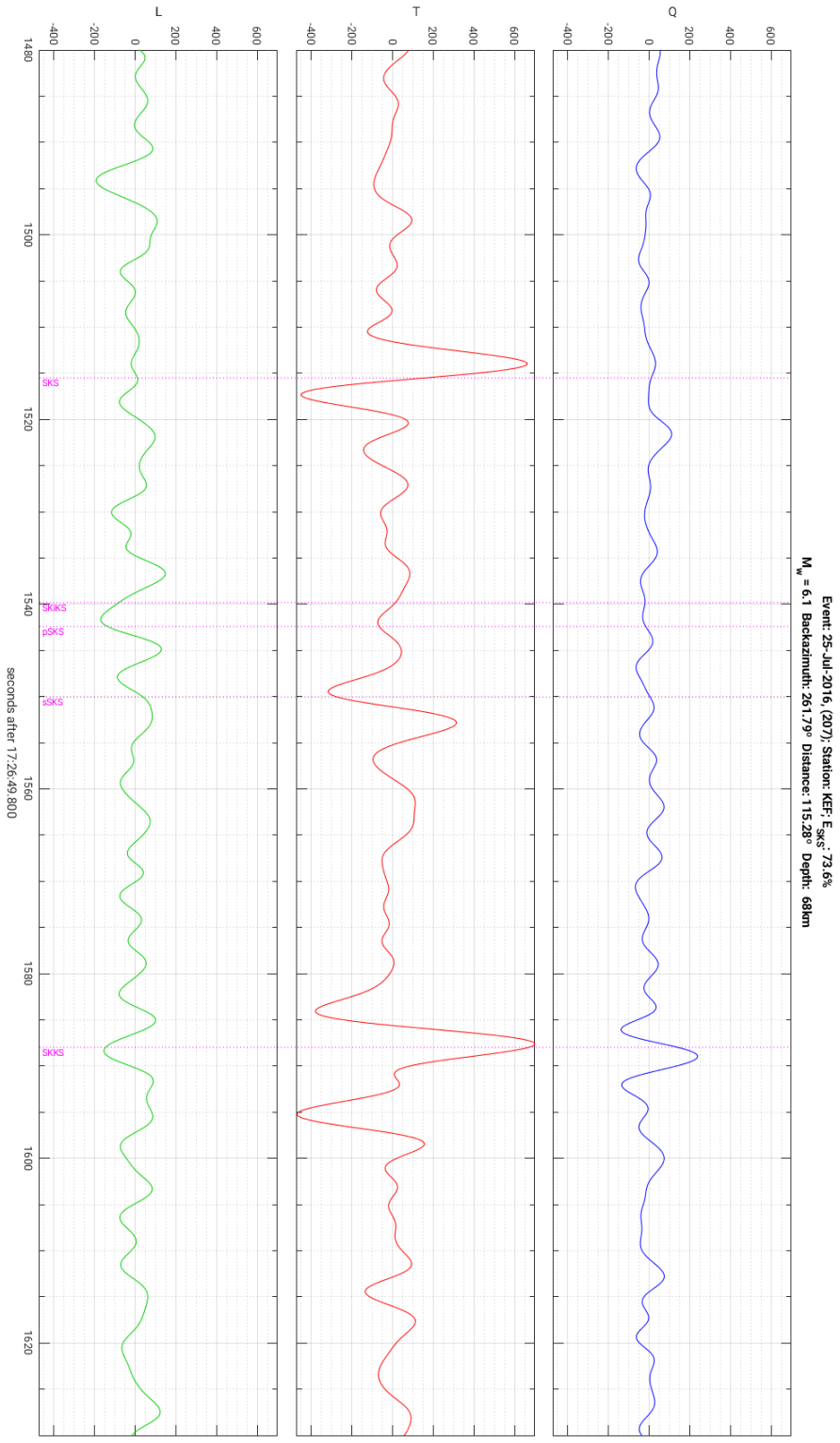

Figure A.1: *View seismogram panel for an earthquake on 2016/07/25, hypocentral depth* $= 68\,km$*,* $M_W = 6.1$*, epicentral distance* $= 115.28°$*, with misorientation of the KEF seismometer. A strong signal is visible on the T-component.*

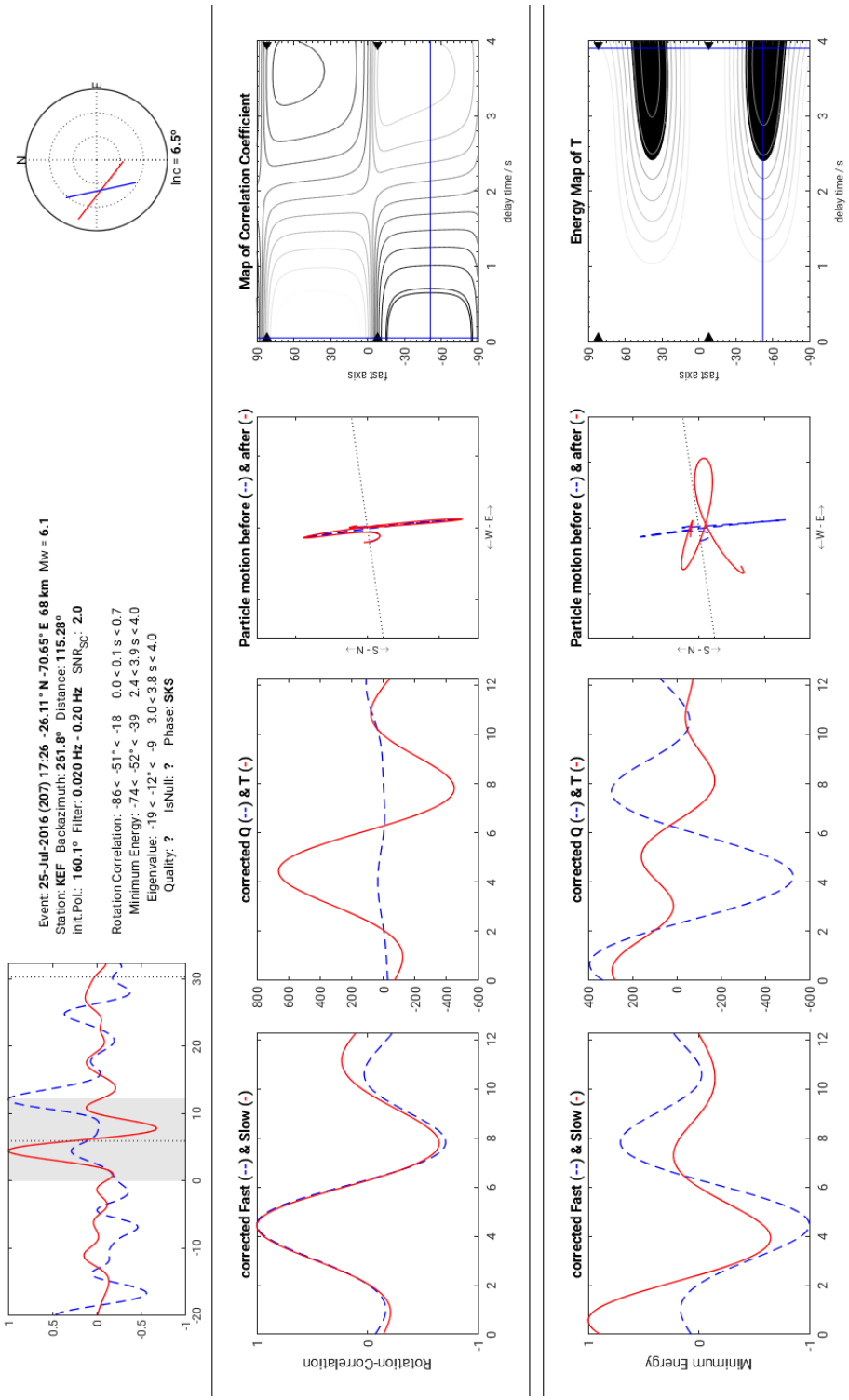

(a) *Diagnostic plot with misorientation*

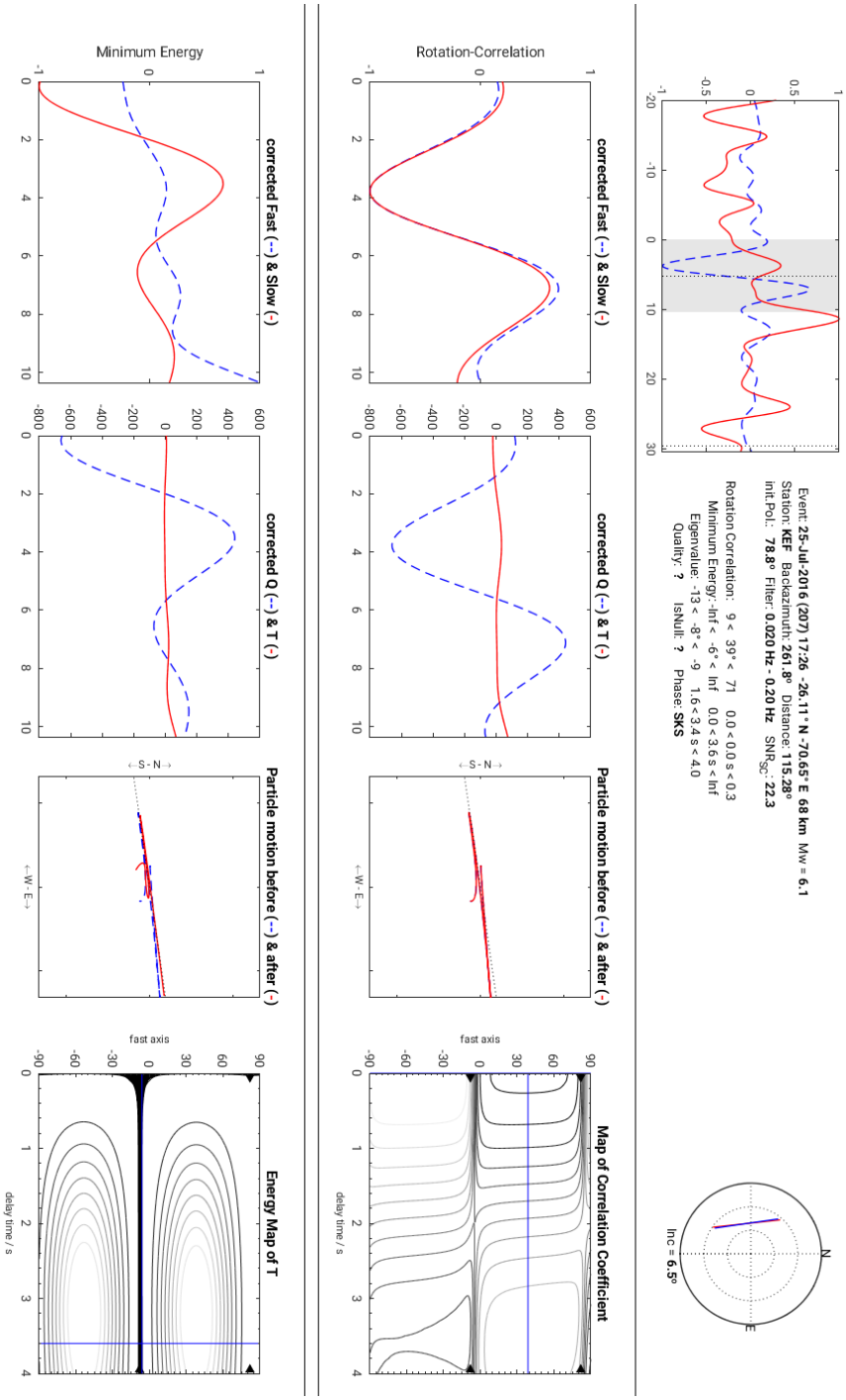

(b) Diagnostic plot with correction for misorientation

Figure A.2: *Diagnostic plot for an earthquake on 2016/07/25, hypocentral depth = 68 km, $M_W = 6.1$, epicentral distance = 115.28°, with misorientation of the seismometer (top) and after the correction for a misorientation of the KEF seismometer (bottom). Strong deviations of the particle motion from the theoretical BAZ occur before correction. The determination of splitting parameters does not agree within both methods and is not working satisfying since we still see a signal on the T-component also after determination of the splitting parameters. After the correction for the misorientation of the station, the particle motion is aligned with the theoretical BAZ and only noise remains on the corrected T-component. Both methods (SC and RC) agree for the corrected traces.*

A.1.2 Comparison of SWSMs by different analysts

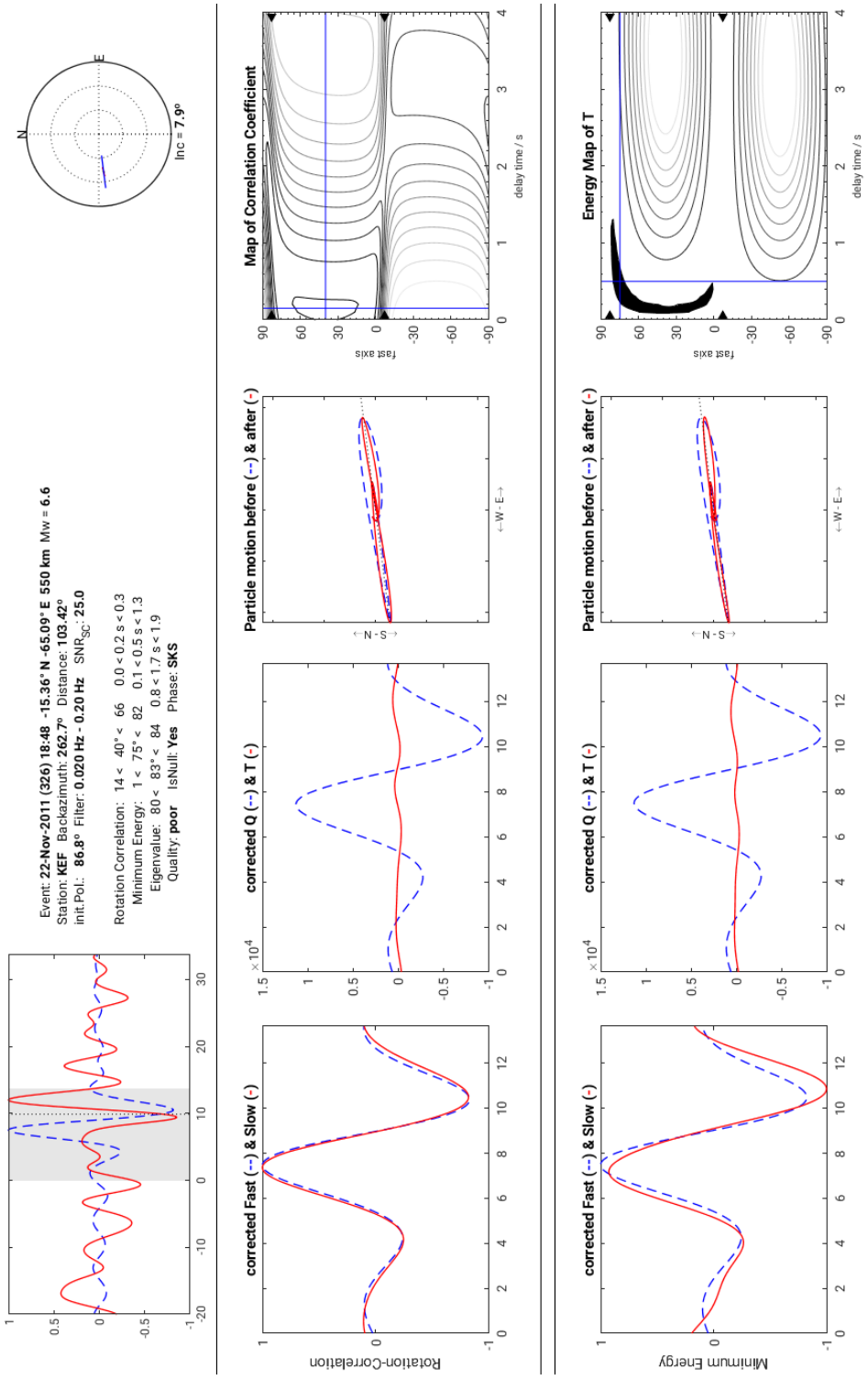

(a) SKS FD

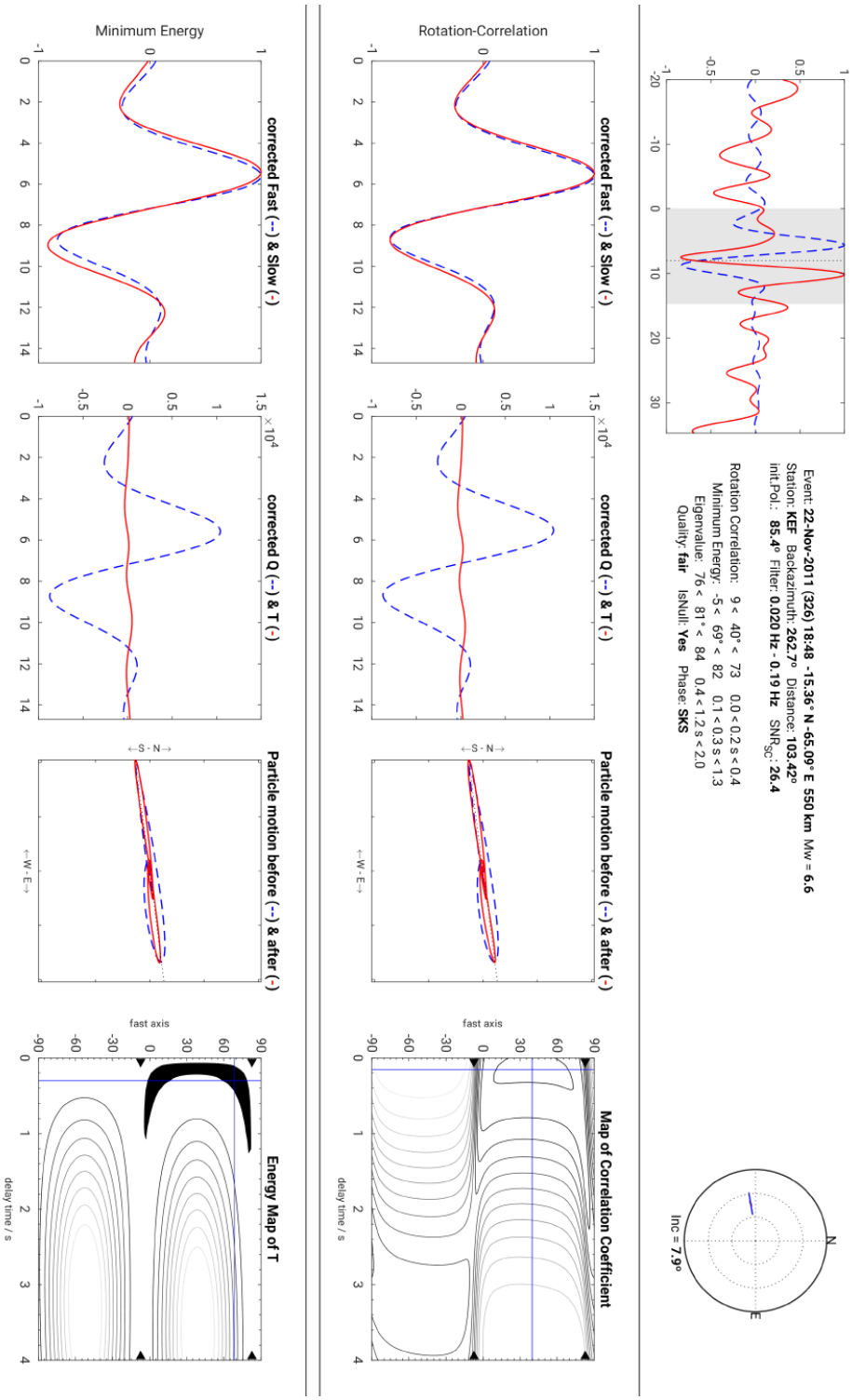
Event: 22-Nov-2011 (326) 18:48 -15.36° N -65.09° E 550 km Mw = 6.6
Station: KEF Backazimuth: 262.7° Distance: 103.42°
int.Pol.: 85.4° Filter: 0.020 Hz - 0.19 Hz SNR$_{SC}$: 26.4
Rotation Correlation: 9 < 40° < 73 0.0 < 0.2 s < 0.4
Minimum Energy: -5 < 69° < 82 0.1 < 0.3 s < 1.3
Eigenvalue: 76 < 81° < 84 0.4 < 1.2 s < 2.0
Quality: fair IsNull: Yes Phase: SKS
Inc = 7.9°
N
E
Rotation-Correlation
corrected Fast (--) & Slow (-)
corrected Q (--) & T (-)
Particle motion before (--) & after (-)
Map of Correlation Coefficient
fast axis
delay time / s
Minimum Energy
corrected Fast (--) & Slow (-)
corrected Q (--) & T (-)
Particle motion before (--) & after (-)
Energy Map of T
fast axis
delay time / s

(b) *SKS MD*

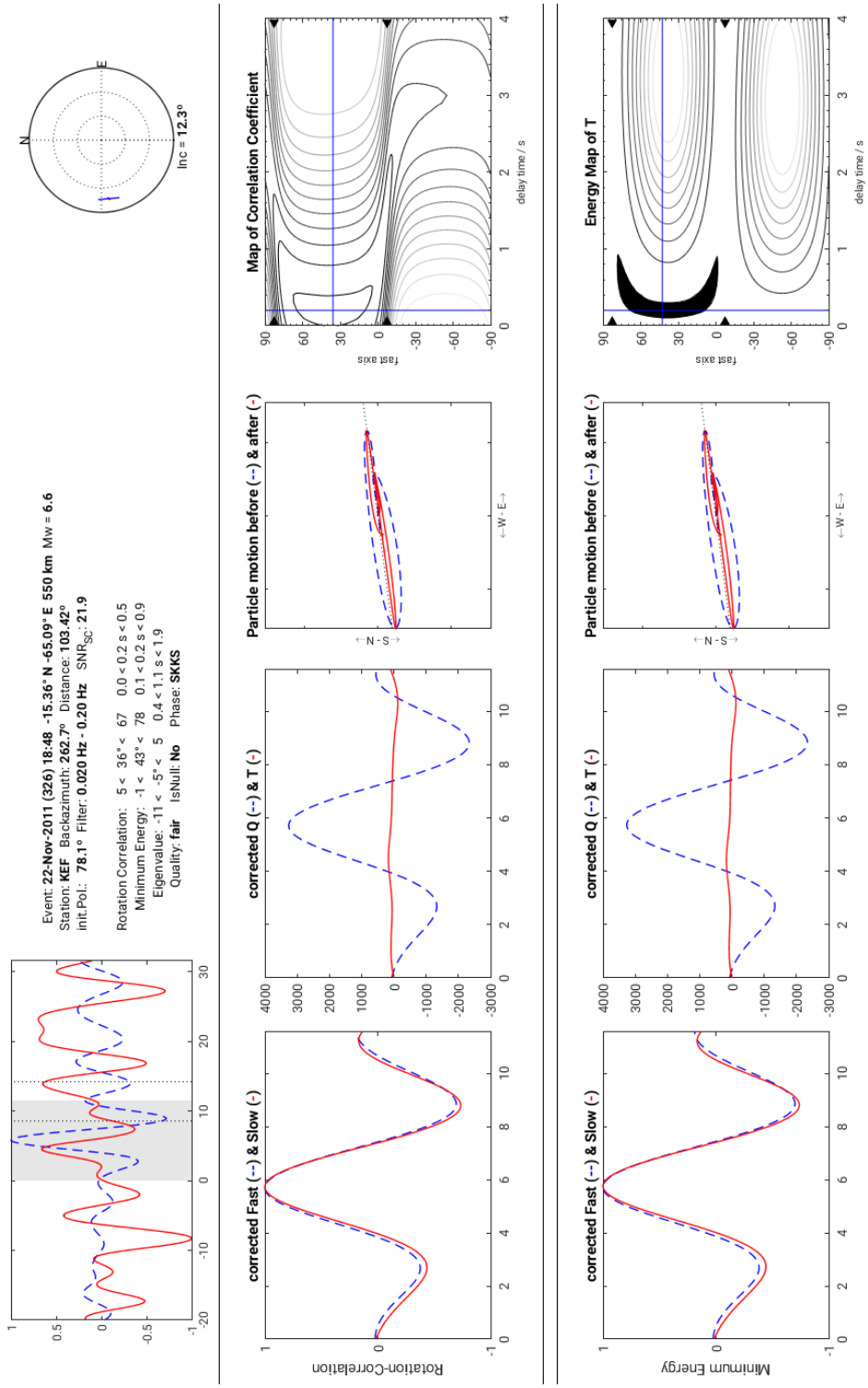
Event: 22-Nov-2011 (326) 18:48 -15.36° N -65.09° E 550 km Mw = 6.6
Station: KEF Backazimuth: 262.7° Distance: 103.42°
init.Pol.: 78.1° Filter: 0.020 Hz - 0.20 Hz SNR$_{SC}$: 21.9
Rotation Correlation: 5 < 36° < 67 0.0 < 0.2 s < 0.5
Minimum Energy: -1 < 43° < 78 0.1 < 0.2 s < 0.9
Eigenvalue: -11 < -5° < 5 0.4 < 1.1 s < 1.9
Quality: fair IsNull: No Phase: SKKS
Inc = 12.3°
N
E
corrected Fast (--) & Slow (-)
corrected Q (--) & T (-)
Particle motion before (--) & after (-)
Map of Correlation Coefficient
Energy Map of T
Rotation-Correlation
Minimum Energy
fast axis
delay time / s
←N - S→
←W - E→

(c) SKKS FD

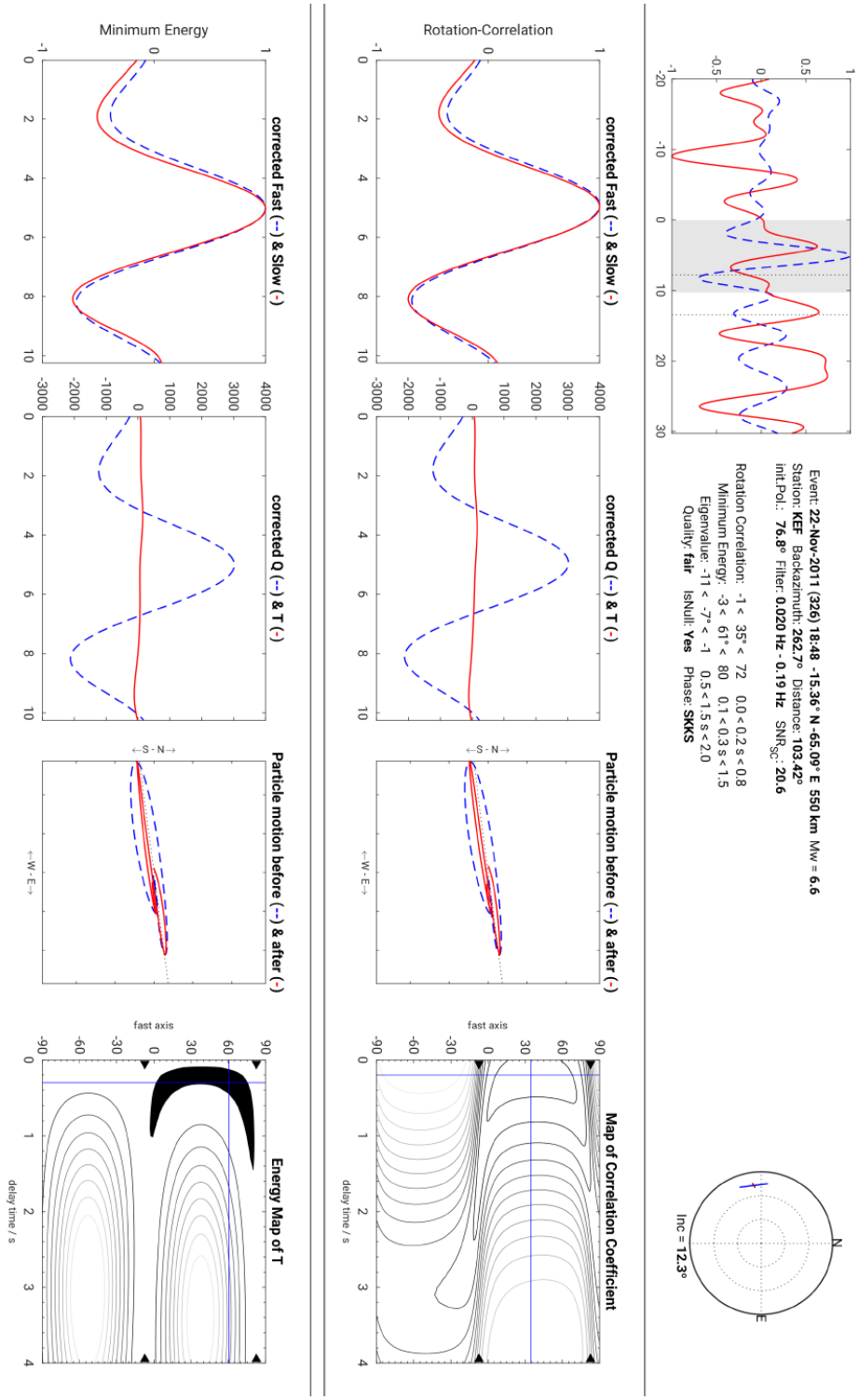

(d) SKKS MD

Figure A.3: *Diagnostic plot of SKS and SKKS phases for an earthquake on 2011/11/22 analysed by MD and myself. The observational type for the SKS phase agrees within both analysts. For the SKKS phase I classified the phase as split while MD classified it as null. There is no strong signal on the T-component and the particle motion is only slightly elliptical but the SC method is not striving towards large delay times.*

A.2 SWSMs beneath Siberia

A.2.1 Station-earthquake configuration

Table A.1: *Parameters of analysed seismic stations to potentially study the HLFL beneath Siberia. The last column represents the number of suitable earthquakes, that occurred after 1995/01/01 independent of the operation status of the recording station, with a piercing point in the LMM within* 15° *radius around the centre of the HLFL beneath Siberia. SWSMs are performed at the stations with bolded entries in the table.*

Station	Network	longitude	latitude	operation time	possible earthquakes
BJO1	NS	19.00383	74.50367	1992/10/24 -	769 (SKKS) & 132 (SKS)
BJT	IC	116.17161	40.01907	1994/05/25 -	44 (SKKS) & 18 (SKS)
DALA	YT	100.47	45.01	2003/04/30 - 2003/10/26	180 (SKKS) & 180 (SKS)
ENH	IC	109.49474	30.2762	1997/09/20 -	42 (SKKS) & 0 (SKS)
HIA	IC	119.74136	49.27012	1994/12/04 -	9 (SKKS) & 171 (SKS)
HSPB	**PL**	**15.5332**	**77.0019**	**2007/09/22 -**	**322 (SKKS) & 52 (SKS)**
JOF	HE	31.31	63.92	2006/01/01 -	722 (SKKS) & 1 (SKS)
KBS	IU	11.9385	78.9154	1994/11/05 -	608 (SKKS) & 122 (SKS)
KBU	GE	69.13	34.52	2005/11/24 -	1 (SKKS) & 0 (SKS)
KEV	IU	27.0035	69.7565	1993/06/07 -	744 (SKKS) & 105 (SKS)
KHOH	YT	88.3539	49.3144	2003/10/08 - 2003/10/10	19 (SKKS) & 566 (SKS)
KIEV	IU	29.2242	50.7012	1995/01/30 -	182 (SKKS) & 0 (SKS)
MAKZ	IU	81.977	46.808	1996/09/14 -	15 (SKKS) & 127 (SKS)
MHV	GE	37.77	54.96	1995/05/13 - 2007/12/31	909 (SKKS) & 0 (SKS)
OKTB	YT	102.98	52.41	2003/05/01 - 2003/10/10	66 (SKKS) & 217 (SKS)
OTUK	CK	72.34	48.24	2010/02/09 -	36 (SKKS) & 29 (SKS)
QIZ	IC	109.8445	19.0291	1996/09/19 -	0 (SKKS) & 0 (SKS)
SA01	**1G**	**25.82**	**71.11**	**2013/11/03 - 2016/04/26**	**762 (SKKS) & 110 (SKS)**
SA02	**1G**	**28.24**	**71.06**	**2013/11/03 - 2016/04/26**	**746 (SKKS) & 102 (SKS)**
SA05	**1G**	**31.01**	**70.28**	**2013/11/03 - 2015/05/05**	**715 (SKKS) & 115 (SKS)**
ULN	**IU**	**107.0532**	**47.8651**	**1994/10/31 -**	**154 (SKKS) & 200 (SKS)**
VADS	NS	29.365	70.12016	2016/09/07 -	726 (SKKS) & 100 (SKS)
WMQ	**IC**	**87.7049**	**43.8138**	**1995/09/23 -**	**124 (SKKS) & 133 (SKS)**
XAN	IC	108.92321	34.03107	1992/11/29 -	133 (SKKS) & 0 (SKS)

A.2.2 Misorientation of the WMQ station

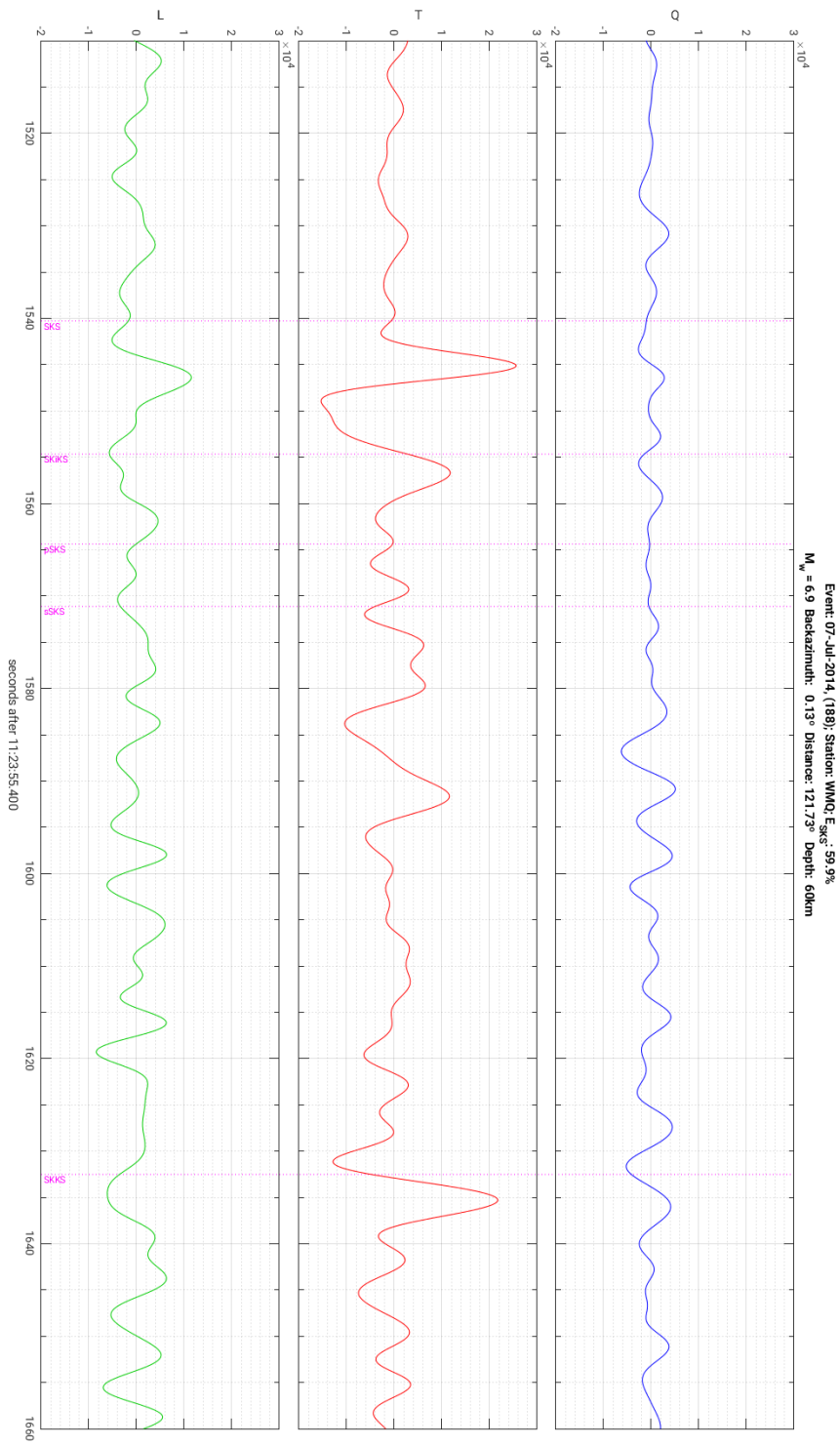

Figure A.4: *View seismogram panel for an earthquake on 2014/07/07, hypocentral depth* $= 60\,\mathrm{km}$*,* $M_W = 6.9$*, epicentral distance* $= 121.73°$*, with misorientation of the WMQ seismometer. A strong signal is visible on the* T*-component for both the SKS as well as the SKKS phase.*

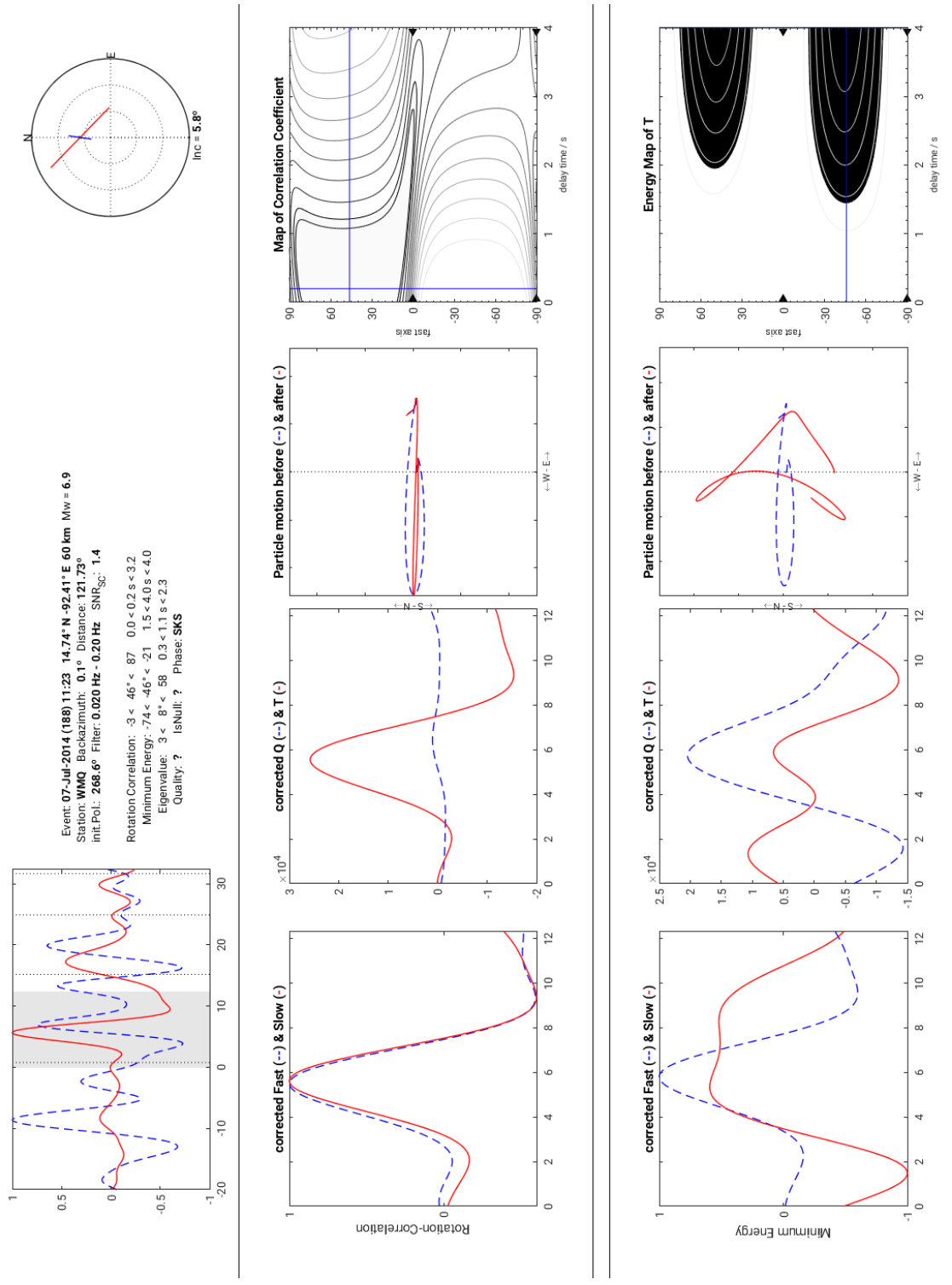

Figure A.5: *Diagnostic plot for an earthquake on 2014/07/07, hypocentral depth* = 60 km, $M_W = 6.9$, *epicentral distance* = 121.73°, *with misorientation of the WMQ seismometer. Strong deviations of the particle motion from the theoretical BAZ occur. The determination of splitting parameters does not agree within both methods and is not working satisfying since we still see a signal on the T-component also after determination of the splitting parameters. Since the exact misorientation of the seismometer is not known, no SWSMs are conducted.*

A.3 Results and discussion

A.3.1 Single measurements of shear wave splitting

Table A.2: *Number of SWSMs for the station HSPB. The first column represents the total amount of phases for which I was able to measure SWS, independent of the splitting observation and the phase. The individual results for the different phases are listed in the other columns. It needs to be taken into account, that all seismic traces are studies for SWS of SKS and PKS phases, measurements of SKKS splitting is only performed if SWS is measured for any of the two.*

total no. of SWSMs	**SKS**		**SKKS**		**PKS**	
	split	null	split	null	split	null
59	19	30	8	2	0	0

Table A.3: *Number of SWSMs for the station ULN. The first column represents the total amount of phases for which I was able to measure SWS, independent of the splitting observation and the phase. The individual results for the different phases are listed in the other columns. It needs to be taken into account, that all seismic traces are studies for SWS of SKS and PKS phases, measurements of SKKS splitting is only performed if SWS is measured for any of the two.*

total no. of SWSMs	**SKS**		**SKKS**		**PKS**	
	split	null	split	null	split	null
41	20	5	4	3	0	9

Table A.4: *Number of SWSMs for the station WMQ. The first column represents the total amount of phases for which I was able to measure SWS, independent of the splitting observation and the phase. The individual results for the different phases are listed in the other columns. It needs to be taken into account, that all seismic traces are studies for SWS of SKS and PKS phases, measurements of SKKS splitting is only performed if SWS is measured for any of the two.*

total no. of SWSMs	**SKS**		**SKKS**		**PKS**	
	split	null	split	null	split	null
8	5	0	3	0	0	0

Table A.5: *Number of SWSMs for the station SA01. The first column represents the total amount of phases for which I was able to measure SWS, independent of the splitting observation and the phase. The individual results for the different phases are listed in the other columns. It needs to be taken into account, that all seismic traces are studies for SWS of SKS and PKS phases, measurements of SKKS splitting is only performed if SWS is measured for any of the two.*

total no. of SWSMs	**SKS**		**SKKS**		**PKS**	
	split	null	split	null	split	null
7	4	1	1	1	0	0

Table A.6: *Number of SWSMs for the station SA02. The first column represents the total amount of phases for which I was able to measure SWS, independent of the splitting observation and the phase. The individual results for the different phases are listed in the other columns. It needs to be taken into account, that all seismic traces are studies for SWS of SKS and PKS phases, measurements of SKKS splitting is only performed if SWS is measured for any of the two.*

total no. of SWSMs	**SKS**		**SKKS**		**PKS**	
	split	null	split	null	split	null
7	3	2	0	2	0	0

Table A.7: *Number of SWSMs for the station SA05. The first column represents the total amount of phases for which I was able to measure SWS, independent of the splitting observation and the phase. The individual results for the different phases are listed in the other columns. It needs to be taken into account, that all seismic traces are studies for SWS of SKS and PKS phases, measurements of SKKS splitting is only performed if SWS is measured for any of the two.*

total no. of SWSMs	**SKS**		**SKKS**		**PKS**	
	split	null	split	null	split	null
0	0	0	0	0	0	0

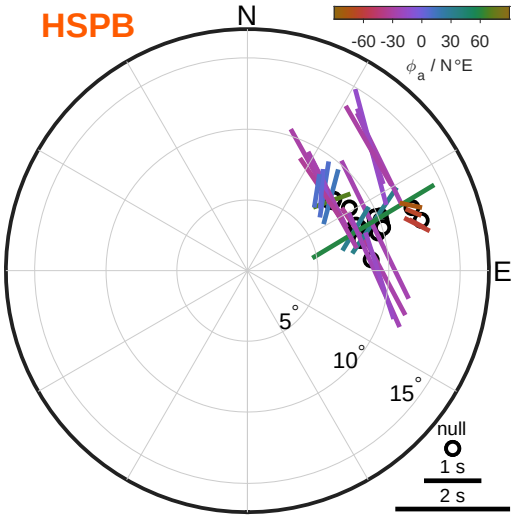

(a) HSPB

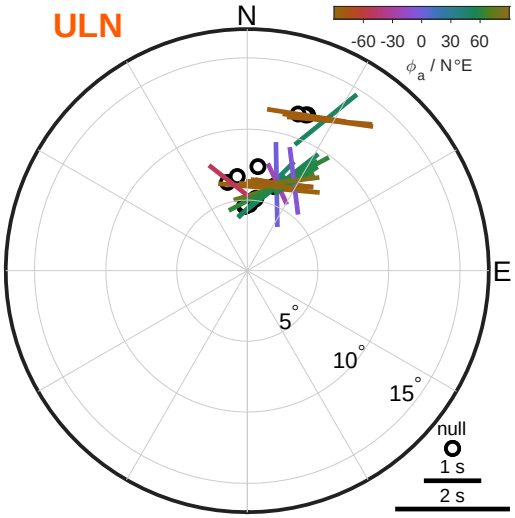

(b) ULN

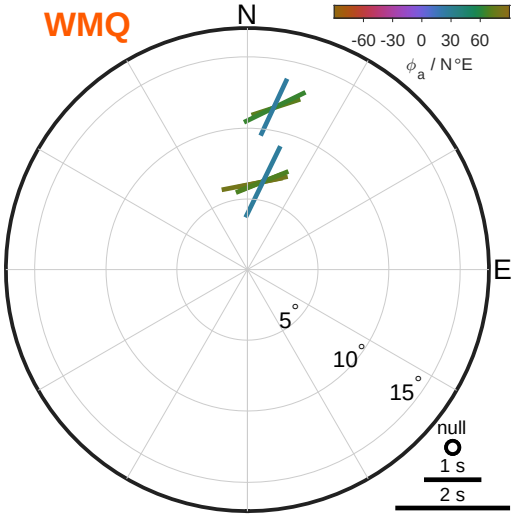

(c) WMQ

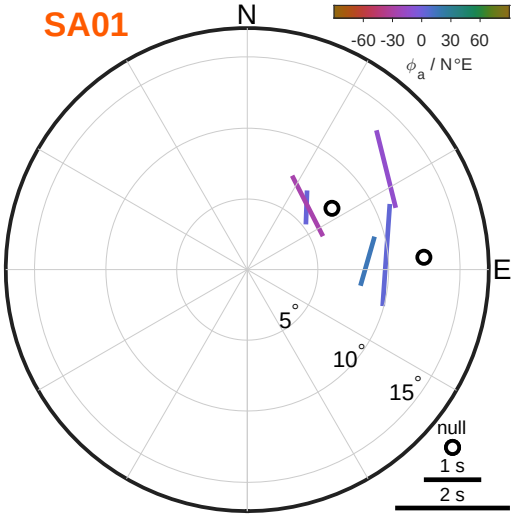

(d) SA01

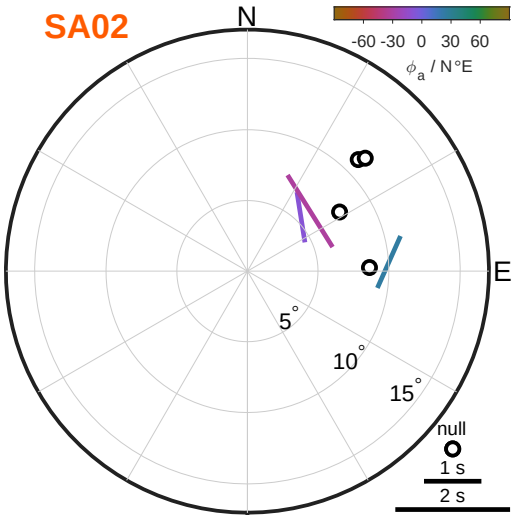

(e) SA02

Figure A.6: *Stereoplots for single SWSMs at the different recording stations to study the HLFL beneath Siberia. The mapped SWS observations include measurements of all quality criteria.*

A.3.2 Directional dependency

Table A.8: *Analysis of the BAZs of EQs where successful SWSMs are performed for at least two XKS phases at the permanent stations HSPB, ULN and WMQ. The indicated hypocentral depth z beneath the range of BAZs for pairs indicates the shallowest depth of an EQ in this BAZ range where a SWSM has still been possible. M_W indicates the smallest moment magnitude for which a SWSM has been possible. This EQ is not necessarily the same event as the event mentioned in the hypocentral depth.*

criteria	**HSPB**	**ULN**	**WMQ**
total range of BAZs	$[41.0, 93.8]^\circ$	$[347.4, 28.8]^\circ$	$[338.2, 10.0]^\circ$
range of BAZs for pairs	$[44, 50]^\circ$ $z \geq 70\,\text{km}$, $M_W \geq 6.1$	$[347, 354]^\circ$ $z \geq 113\,\text{km}$, $M_W \geq 5.8$	$[9.2, 10.0]^\circ$ $z \geq 60\,\text{km}$, $M_W \geq 5.9$
	$[68, 75]^\circ$ $z \geq 100\,\text{km}$, $M_W \geq 5.8$	$[357, 6]^\circ$ $z \geq 120\,\text{km}$, $M_W \geq 5.9$	
		$[18, 29]^\circ$ $z \geq 54\,\text{km}$, $M_W \geq 6.0$	

Bibliography

Amit, H., Aubert, J., and Hulot, G. (2010). "Stationary, oscillating or drifting mantle-driven geomagnetic flux patches?" *Journal of Geophysical Research: Solid Earth* 115.B7. ISSN: 0148-0227. DOI: 10.1029/2009jb006542.

Amit, H., Korte, M., Aubert, J., Constable, C., and Hulot, G. (2011). "The time-dependence of intense archeomagnetic flux patches". *Journal of Geophysical Research* 116.B12. ISSN: 0148-0227. DOI: 10.1029/2011jb008538.

Aubert, J. (2005). "Steady zonal flows in spherical shell dynamos". *Journal of Fluid Mechanics* 542.1, pp. 53–67. ISSN: 1469-7645. DOI: 10.1017/S0022112005006129.

Beyreuther, M., Barsch, R., Krischer, L., Megies, T., Behr, Y., and Wassermann, J. (2010). "ObsPy: A Python Toolbox for Seismology". *Seismological Research Letters* 81.3, pp. 530–533. DOI: 10.1785/gssrl.81.3.530.

Bloxham, J. and Gubbins, D. (1987). "Thermal core– mantle interactions". *Nature* 325.6104, pp. 511–513. ISSN: 1476-4687. DOI: 10.1038/325511a0.

Bowman, J. R. and Ando, M. (1987). "Shear-wave splitting in the upper-mantle wedge above the Tonga subduction zone". *Geophysical Journal International* 88.1, pp. 25–41. ISSN: 1365-246X. DOI: 10.1111/j.1365-246x.1987.tb01367.x.

Busse, F. H. (2000). "Homogeneous Dynamos in Planetary Cores and in the Laboratory". *Annual Review of Fluid Mechanics* 32.1, pp. 383–408. ISSN: 1545-4479. DOI: 10.1146/annurev.fluid.32.1.383.

Clauser, C. (2014). *Einführung in die Geophysik: Globale physikalische Felder und Prozesse in der Erde*. Springer Berlin Heidelberg. ISBN: 9783642044960. DOI: 10.1007/978-3-642-04496-0.

Creasy, N., Pisconti, A., Long, M. D., and Thomas, C. (2021). "Modeling of Seismic Anisotropy Observations Reveals Plausible Lowermost Mantle Flow Directions Beneath Siberia". *Geochemistry, Geophysics, Geosystems* 22.10. DOI: https://doi.org/10.1029/2021GC009924.

Crotwell, H. P., Owens, T. J., and Ritsema, J. (1999). "The TauP Toolkit: Flexible Seismic Travel-time and Ray-path Utilities". *Seismological Research Letters* 70.2, pp. 154–160. ISSN: 0895-0695. DOI: 10.1785/gssrl.70.2.154.

Deng, J., Long, M. D., Creasy, N., Wagner, L., Beck, S., Zandt, G., Tavera, H., and Minaya, E. (2017). "Lowermost mantle anisotropy near the eastern edge of the Pacific LLSVP: constraints from SKS–SKKS splitting intensity measurements". *Geophysical Journal International* 210.2, pp. 774–786. ISSN: 1365-246X. DOI: 10.1093/gji/ggx190.

Dziewonski, A. M., Chou, T.-A., and Woodhouse, J. H. (1981). "Determination of earthquake source parameters from waveform data for studies of global and regional seis-

micity". *Journal of Geophysical Research: Solid Earth* 86.B4, pp. 2825–2852. ISSN: 0148-0227. DOI: 10.1029/jb086ib04p02825.

Ekström, G., Nettles, M., and Dziewoński, A. (2012). "The global CMT project 2004–2010: Centroid-moment tensors for 13,017 earthquakes". *Physics of the Earth and Planetary Interiors* 200–201, pp. 1–9. ISSN: 0031-9201. DOI: 10.1016/j.pepi.2012.04.002.

Finlay, C. C. and Jackson, A. (2003). "Equatorially Dominated Magnetic Field Change at the Surface of Earth's Core". *Science* 300.5628, pp. 2084–2086. ISSN: 1095-9203. DOI: 10.1126/science.1083324.

Fröhlich, Y. (2020). "Scherwellen-Doppelbrechung von SK(K)S-Phasen und lateral variierende Anisotropie im Gebiet des Oberrheingrabens". Masterarbeit, Geophysikalisches Institut (GPI), Karlsruher Institut für Technologie (KIT). DOI: 10.5445/IR/1000165525.

Fröhlich, Y., Grund, M., and Ritter, J. (2021). "Laterally and Vertically Varying Seismic Anisotropy in the Upper Mantle below Central Europe". In: *AGU Fall Meeting Abstracts*. Vol. 2021. URL: https://ui.adsabs.harvard.edu/abs/2021AGUFMDI45C0032F.

Fröhlich, Y., Grund, M., and Ritter, J. R. R. (2023). "On the effects of wrongly aligned seismogram components for shear wave splitting analysis". *Annals of Geophysics* 66.2, SE207. ISSN: 1593-5213. DOI: 10.4401/ag-8781.

Garnero, E. J., Kennett, B., and Loper, D. E. (2005). "Studies of the Earth's Deep Interior—Eighth Symposium". *Physics of the Earth and Planetary Interiors* 153.1–3. Studies of the Earth's Deep Interior, pp. 1–2. ISSN: 0031-9201. DOI: 10.1016/j.pepi.2005.08.003.

Greulich, W., Barnert, S., Dr. Delbrück, M., Dr. Eis, R., Natalie, F., Heinisch, C., Nagel, S., Dr. Radons, G., Schilling-Benz, L., and Dr. Schüller, J. (1998). *Spektrum.de, Lexikon der Physik, Anisotropie*. URL: https://www.spektrum.de/lexikon/physik/anisotropie/541 (visited on 01/11/2025).

Grund, M. and Ritter, J. R. (2018). "Widespread seismic anisotropy in Earth's lowermost mantle beneath the Atlantic and Siberia". *Geology* 47.2, pp. 123–126. ISSN: 0091-7613. DOI: 10.1130/g45514.1.

Gubbins, D., Willis, A. P., and Sreenivasan, B. (2007). "Correlation of Earth's magnetic field with lower mantle thermal and seismic structure". *Physics of the Earth and Planetary Interiors* 162.3–4, pp. 256–260. ISSN: 0031-9201. DOI: 10.1016/j.pepi.2007.04.014.

Heron, P. J. (2019). "Mantle plumes and mantle dynamics in the Wilson cycle". *Geological Society, London, Special Publications* 470.1, pp. 87–103. ISSN: 2041-4927. DOI: 10.1144/sp470-2018-97.

Hunter, J. D. (2007). "Matplotlib: A 2D graphics environment". *Computing in Science & Engineering* 9.3, pp. 90–95. DOI: 10.1109/MCSE.2007.55.

Jackson, A., Jonkers, A. R. T., and Walker, M. R. (2000). "Four centuries of geomagnetic secular variation from historical records". *Philosophical Transactions of the Royal Society of London. Series A: Mathematical, Physical and Engineering Sciences* 358.1768, pp. 957–990. ISSN: 1471-2962. DOI: 10.1098/rsta.2000.0569.

Kaviris, G., Fountoulakis, I., Spingos, I., Millas, C., Papadimitriou, P., and Drakatos, G. (2018). "Mantle dynamics beneath Greece from SKS and PKS seismic anisotropy study". *Acta Geophysica* 66.6, pp. 1341–1357. ISSN: 1895-7455. DOI: 10.1007/s11600-018-0225-z.

Kendall, J.-M. and Silver, P. G. (1998). "Investigating causes of D" anistropy". In: *The Core-Mantle Boundary Region*. Vol. 28. American Geophysical Union (AGU), pp. 97–118. URL: https://agupubs.onlinelibrary.wiley.com/doi/abs/10.1029/GD028p0097.

Kennett, B. (2005). *AK135tables*. URL: https://www.researchgate.net/publication/257584026_AK135tables.

Kennett, B. and Engdahl, E. (1991). "Traveltimes for global earthquake location and phase identification". *Geophysical Journal International* 105.2, pp. 429–465. ISSN: 0956-540X. DOI: 10.1111/j.1365-246x.1991.tb06724.x.

Lay, T., Williams, Q., Garnero, E. J., Kellogg, L., and Wysession, M. E. (1998). "Seismic Wave Anisotropy in the D" Region and Its Implications". In: *The Core-Mantle Boundary Region*. Vol. 28. American Geophysical Union, pp. 299–318. URL: https://agupubs.onlinelibrary.wiley.com/doi/10.1029/GD028p0299.

Li, M. (2020). "The Formation of Hot Thermal Anomalies in Cold Subduction-Influenced Regions of Earth's Lowermost Mantle". *Journal of Geophysical Research: Solid Earth* 125.6. DOI: https://doi.org/10.1029/2019JB019312.

Long, M. D. and Becker, T. W. (2010). "Mantle dynamics and seismic anisotropy". *Earth and Planetary Science Letters* 297.3–4, pp. 341–354. ISSN: 0012-821X. DOI: 10.1016/j.epsl.2010.06.036.

Long, M. D. and Lynner, C. (2015). "Seismic anisotropy in the lowermost mantle near the Perm Anomaly". *Geophysical Research Letters* 42.17, pp. 7073–7080. DOI: https://doi.org/10.1002/2015GL065506.

Long, M. D. and Silver, P. G. (2009). "Shear Wave Splitting and Mantle Anisotropy: Measurements, Interpretations, and New Directions". *Surveys in Geophysics* 30.4–5, pp. 407–461. ISSN: 1573-0956. DOI: 10.1007/s10712-009-9075-1.

Long, M. D. and van der Hilst, R. D. (2005). "Estimating Shear-Wave Splitting Parameters from Broadband Recordings in Japan: A Comparison of Three Methods". *Bulletin of the Seismological Society of America* 95.4, pp. 1346–1358. ISSN: 0037-1106. DOI: 10.1785/0120040107.

Maupin, V. and Park, J. (2007). "Theory and Observations – Wave Propagation in Anisotropic Media". *Seismology and the Structure of the Earth. Treatise on Geophysics* 1, pp. 289–321. DOI: 10.1016/b978-044452748-6.00007-9.

McNamara, A. K. (2019). "A review of large low shear velocity provinces and ultra low velocity zones". *Tectonophysics* 760, pp. 199–220. ISSN: 0040-1951. DOI: 10.1016/j.tecto.2018.04.015.

Meade, C., Silver, P. G., and Kaneshima, S. (1995). "Laboratory and seismological observations of lower mantle isotropy". *Geophysical Research Letters* 22.10, pp. 1293–1296. ISSN: 1944-8007. DOI: 10.1029/95gl01091.

Moores, E. M. and Twiss, R. J. (2014). *Tectonics*. United States of America: Waveland Press, Inc.

Murakami, M., Hirose, K., Kawamura, K., Sata, N., and Ohishi, Y. (2004). "Post-perovskite phase transition in $MgSiO_3$". *Science* 304.5672, pp. 855–858. ISSN: 1095-9203. DOI: 10.1126/science.1095932.

National Science Foundation's Seismological Facility for the Advancement of Geoscience (2018). *MetaData Aggregator*. URL: http://ds.iris.edu/mda/IC/WMQ/ (visited on 03/10/2025).

Nowacki, A., Wookey, J., and Kendall, J.-M. (2011). "New advances in using seismic anisotropy, mineral physics and geodynamics to understand deformation in the lowermost mantle". *Journal of Geodynamics* 52.3–4, pp. 205–228. ISSN: 0264-3707. DOI: 10.1016/j.jog.2011.04.003.

Olson, P. and Amit, H. (2006). "Changes in earth's dipole". *Naturwissenschaften* 93.11, pp. 519–542. ISSN: 1432-1904. DOI: 10.1007/s00114-006-0138-6.

Peltier, W. R. (2007). "Mantle Dynamics and the D" layer: Impacts of the Post Perovskite Phase". In: *Post-Perovskite: The Last Mantle Phase Transition*. Vol. 174. American Geophysical Union, pp. 217–227. DOI: 10.1029/174gm15.

Plomerová, J., Šílenỳ, J., and Babuška, V. (1996). "Joint interpretation of upper-mantle anisotropy based on teleseismic P-travel time delays and inversion of shear-wave splitting parameters". *Physics of the Earth and Planetary Interiors* 95.3–4, pp. 293–309. ISSN: 0031-9201. DOI: 10.1016/0031-9201(95)03122-7.

Restivo, A. and Helffrich, G. (1999). "Teleseismic shear wave splitting measurements in noisy environments". *Geophysical Journal International* 137.3, pp. 821–830. ISSN: 0956-540X. DOI: 10.1046/j.1365-246x.1999.00845.x.

Sanz Alonso, Y. (2017). "Bestimmung von SKS-Splitting-Parametern und Anisotropiemodellen im Bereich des Oberrheingrabens". Masterarbeit, Geophysikalisches Institut (GPI), Karlsruher Institut für Technologie (KIT).

Savage, M. K. (1999). "Seismic anisotropy and mantle deformation: What have we learned from shear wave splitting?" *Reviews of Geophysics* 37.1, pp. 65–106. ISSN: 1944-9208. DOI: 10.1029/98rg02075.

Silver, P. G. and Chan, W. W. (1991). "Shear wave splitting and subcontinental mantle deformation". *Journal of Geophysical Research: Solid Earth* 96.B10, pp. 16429–16454. ISSN: 0148-0227. DOI: 10.1029/91jb00899.

Silver, P. G. and Long, M. D. (2011). "The non-commutivity of shear wave splitting operators at low frequencies and implications for anisotropy tomography". *Geophysical Journal International* 184.3, pp. 1415–1427. DOI: 10.1111/j.1365-246X.2010.04927.x.

Silver, P. G. and Savage, M. K. (1994). "The Interpretation of Shear-Wave Splitting Parameters In the Presence of Two Anisotropic Layers". *Geophysical Journal International* 119.3, pp. 949–963. DOI: 10.1111/j.1365-246X.1994.tb04027.x.

Simmons, N. A., Forte, A. M., Boschi, L., and Grand, S. P. (2010). "GyPSuM: A joint tomographic model of mantle density and seismic wave speeds". *Journal of Geophysical Research: Solid Earth* 115.B12. ISSN: 0148-0227. DOI: 10.1029/2010jb007631.

Thomas, C. and Kendall, J.-M. (2002). "The lowermost mantle beneath northern Asia — II. Evidence for lower-mantle anisotropy". *Geophysical Journal International* 151.1, pp. 296–308. ISSN: 0956-540X. DOI: 10.1046/j.1365-246X.2002.01760.x.

Thrastarson, S., van Herwaarden, D.-P., Noe, S., Josef Schiller, C., and Fichtner, A. (2024). "REVEAL: A Global Full-Waveform Inversion Model". *Bulletin of the Seismological Society of America* 114.3, pp. 1392–1406. ISSN: 0037-1106. DOI: 10.1785/0120230273.

Thybo, H., Bulut, N., Grund, M., et al. (2021). "ScanArray — A Broadband Seismological Experiment in the Baltic Shield". *Seismological Research Letters* 92.5, pp. 2811–2823. ISSN: 0895-0695. DOI: 10.1785/0220210015.

Tian, D., Uieda, L., Leong, W. J., et al. (2025). *PyGMT: A Python interface for the Generic Mapping Tools*. Version 0.14.2. DOI: 10.5281/zenodo.14868324.

U.S. Geological Survey (2025). *USGS, USGS Earthquake Hazards Program, Search Earthquake Catalog*. URL: https://earthquake.usgs.gov/earthquakes/search/ (visited on 02/14/2025).

van der Meer, D. G., van Hinsbergen, D. J., and Spakman, W. (2018). "Atlas of the underworld: Slab remnants in the mantle, their sinking history, and a new outlook on lower mantle viscosity". *Tectonophysics* 723, pp. 309–448. ISSN: 0040-1951. DOI: https://doi.org/10.1016/j.tecto.2017.10.004.

Vecsey, L., Plomerová, J., and Babuška, V. (2008). "Shear-wave splitting measurements — Problems and solutions". *Tectonophysics* 462.1. Seismic Anisotropy and Geodynamics of the Lithosphere-Asthenosphere System, pp. 178–196. ISSN: 0040-1951. DOI: https://doi.org/10.1016/j.tecto.2008.01.021.

Wang, Y. and Wen, L. (2007). "Complex seismic anisotropy at the border of a very low velocity province at the base of the Earth's mantle". *Journal of Geophysical Research: Solid Earth* 112.B9. DOI: https://doi.org/10.1029/2006JB004719.

Waskom, M. L. (2021). "seaborn: statistical data visualization". *Journal of Open Source Software* 6.60, p. 3021. DOI: 10.21105/joss.03021.

Wolf, J., Long, M. D., Li, M., and Garnero, E. (2023). "Global Compilation of Deep Mantle Anisotropy Observations and Possible Correlation With Low Velocity Provinces". *Geochemistry, Geophysics, Geosystems* 24.10. DOI: https://doi.org/10.1029/2023GC011070.

Wookey, J. and Kendall, J.-M. (2008). "Constraints on lowermost mantle mineralogy and fabric beneath Siberia from seismic anisotropy". *Earth and Planetary Science Letters* 275.1, pp. 32–42. ISSN: 0012-821X. DOI: https://doi.org/10.1016/j.epsl.2008.07.049.

Wookey, J. and Kendall, J.-M. (2007). "Seismic Anisotropy of Post-Perovskite and the Lowermost Mantle". In: *Post-Perovskite: The Last Mantle Phase Transition*. Vol. 174. American Geophysical Union, pp. 171–189. DOI: 10.1029/174gm13.

Wüstefeld, A. and Bokelmann, G. (2007). "Null Detection in Shear-Wave Splitting Measurements". *Bulletin of the Seismological Society of America* 97.4, pp. 1204–1211. ISSN: 0037-1106. DOI: 10.1785/0120060190.

Wüstefeld, A., Bokelmann, G., Zaroli, C., and Barruol, G. (2008). "SplitLab: A shear-wave splitting environment in Matlab". *Computers & Geosciences* 34.5, pp. 515–528. ISSN: 0098-3004. DOI: 10.1016/j.cageo.2007.08.002.

Parts of this thesis have been checked with artificial intelligence systems to correct for spelling, grammar and stylistic aspects of the text.